Weinzirl, T, Jogee, S, Neistein, E, Khochfar, S, Kormendy, J, Marinova, I, Hoyos, C, Balcells, M, den Brok, M, Hammer, D, Peletier, RF, Kleijn, GV, Carter, D, Goudfrooij, P, Lucey, JR, Mobasher, B, Trentham, N, Erwin, P and Puzia, T

The HST/ACS Coma Cluster Survey - VII. Structure and assembly of massive galaxies in the centre of the Coma cluster

Monthly Notices
of the
ROYAL ASTRONOMICAL SOCIETY
MNRAS **441,** 3083–3121 (2014) doi:10.1093/mnras/stu731

The *HST*/ACS Coma Cluster Survey – VII. Structure and assembly of massive galaxies in the centre of the Coma cluster

Tim Weinzirl,[1]★ Shardha Jogee,[1] Eyal Neistein,[2] Sadegh Khochfar,[2,3] John Kormendy,[1] Irina Marinova,[4] Carlos Hoyos,[5] Marc Balcells,[6,7,8] Mark den Brok,[9] Derek Hammer,[10,11] Reynier F. Peletier,[12] Gijs Verdoes Kleijn,[12] David Carter,[13] Paul Goudfrooij,[14] John R. Lucey,[15] Bahram Mobasher,[16] Neil Trentham,[17] Peter Erwin[2,18] and Thomas Puzia[19]

[1]*Department of Astronomy, 2515 Speedway, Stop C1400, Austin, TX 78712-1205, USA*
[2]*Max Planck Institut für extraterrestrische Physik, PO Box 1312, D-85478 Garching, Germany*
[3]*Institute for Astronomy, University of Edinburgh, Royal Observatory, Edinburgh EH9 3HJ, UK*
[4]*Southwestern University, Department of Physics, 1001 E. University Avenue, Georgetown, TX 78626, USA*
[5]*Instituto de Astronomia, Geofísica e Ciências Atmosféricas, Rua do Matão 1226, Cidade Universitária São Paulo-SP, Brazil*
[6]*Isaac Newton Group of Telescopes, Apartado 321, E-38700 Santa Cruz de La Palma, Canary Islands, Spain*
[7]*Instituto de Astrofísica de Canarias, E-38200 La Laguna, Islas Canarias, Spain*
[8]*Departamento de Astrofísica, Universidad de La Laguna, E-38206 La Laguna, Islas Canarias, Spain*
[9]*Department of Physics and Astronomy, University of Utah, Salt Lake City, UT 84112, USA*
[10]*Department of Physics and Astronomy, Johns Hopkins, Baltimore, MD 21218, USA*
[11]*NASA Goddard Space Flight Center, Code 662, Greenbelt, MD 20771, USA*
[12]*Kapteyn Astronomical Institute, University of Groningen, PO Box 800, NL-9700 AV Groningen, the Netherlands*
[13]*Astrophysics Research Institute, Liverpool John Moores University, IC2 Liverpool Science Park, 146 Brownlow Hill, Liverpool L3 5RF, UK*
[14]*Space Telescope Science Institute, 3700 San Martin Drive, Baltimore, MD 21218, USA*
[15] *Department of Physics, Durham University, South Road, Durham DH1 3LE, UK*
[16]*Department of Physics and Astronomy, University of California, Riverside, CA 92521, USA*
[17]*Institute of Astronomy, Madingley Road, Cambridge CB3 0HA, UK*
[18]*Universitäts-Sternwarte München, Scheinerstrasse 1, D-81679 München, Germany*
[19]*Department of Astronomy and Astrophysics, Pontificia Universidad Católica de Chile, Avenida Vicuña Mackenna 4860, Macul, Santiago, Chile*

Accepted 2014 April 10. Received 2014 March 25; in original form 2013 September 30

ABSTRACT

We constrain the assembly history of galaxies in the projected central 0.5 Mpc of the Coma cluster by performing structural decomposition on 69 massive ($M_\star \geq 10^9$ $M_\odot$) galaxies using high-resolution *F*814*W* images from the *Hubble Space Telescope* (*HST*) Treasury Survey of Coma. Each galaxy is modelled with up to three Sérsic components having a free Sérsic index *n*. After excluding the two cDs in the projected central 0.5 Mpc of Coma, 57 per cent of the galactic stellar mass in the projected central 0.5 Mpc of Coma resides in classical bulges/ellipticals while 43 per cent resides in cold disc-dominated structures. Most of the stellar mass in Coma may have been assembled through major (and possibly minor) mergers. Hubble types are assigned based on the decompositions, and we find a strong morphology–density relation; the ratio of (E+S0):spirals is (91.0 per cent):9.0 per cent. In agreement with earlier work, the size of outer discs in Coma S0s/spirals is smaller compared with lower density environments captured with SDSS (Data Release 2). Among similar-mass clusters from a hierarchical semi-analytic model, no single cluster can simultaneously match all the global properties of the Coma cluster. The model strongly overpredicts the mass of cold gas and underpredicts the mean fraction of stellar mass locked in hot components over a wide range of galaxy masses. We suggest that these disagreements with the model result from missing cluster physics (e.g. ram-pressure stripping), and certain bulge assembly modes (e.g. mergers of clumps). Overall, our study of Coma underscores that galaxy evolution is not solely a function of stellar mass, but also of environment.

Key words: galaxies: bulges – galaxies: clusters: Coma – galaxies: elliptical and lenticular, cD – galaxies: evolution – galaxies: formation – galaxies: structure.

★ E-mail: timw@astro.as.utexas.edu

1 INTRODUCTION

How galaxies form and evolve is one of the primary outstanding problems in extragalactic astronomy. The initial conditions led to the collapse of dark matter haloes which clustered hierarchically into progressively larger structures. In the halo interiors, gas formed rotating discs which underwent star formation (SF) to produce stellar discs (Cole et al. 2000; Steinmetz & Navarro 2002). The subsequent growth of galaxies is thought to have proceeded through a combination of major mergers (e.g. Toomre 1977; Barnes 1988; Khochfar & Silk 2006, 2009), minor mergers (e.g. Oser et al. 2012; Hilz, Naab & Ostriker 2013), cold-mode gas accretion (Birnboim & Dekel 2003; Kereš et al. 2005, 2009; Dekel & Birnboim 2006; Brooks et al. 2009; Dekel, Sari & Ceverino 2009a; Dekel et al. 2009b; Ceverino, Dekel & Bournaud 2010), and secular processes (Kormendy & Kennicutt 2004).

In early simulations focusing on gas-poor mergers, the major merger of two spiral galaxies with mass ratio $M_1/M_2 \geq 1/4$ would inevitably destroy the pre-existing stellar discs by violent relaxation, producing a remnant bulge or elliptical having a puffed-up distribution of stars with a low ratio of ordered-to-random motion (V/σ) and a steep de Vaucouleurs $r^{1/4}$ surface brightness profile[1] (Toomre 1977). Improved simulations (Naab, Khochfar & Burkert 2006; Robertson et al. 2006; Governato et al. 2007; Hopkins et al. 2009a,b) significantly revised this picture. In unequal-mass major mergers, violent relaxation of stellar discs is not complete. Furthermore, for major mergers where the progenitors have moderate-to-high gas fractions, gas-dissipative processes build discs on small and large scales (Hernquist & Mihos 1995; Robertson et al. 2006; Hopkins et al. 2009a,b; Kormendy et al. 2009). The overall single Sérsic index n of such remnants are typically $2 \lesssim n \lesssim 4$ (Naab et al. 2006; Naab & Trujillo 2006; Hopkins et al. 2009a). The subsequent accretion of gas from the halo, cold streams, and minor mergers can further build large-scale stellar discs, whose size depends on the specific angular momentum of the accreted gas (Steinmetz & Navarro 2002; Birnboim & Dekel 2003; Kereš et al. 2005, 2009; Dekel & Birnboim 2006; Robertson et al. 2006; Dekel et al. 2009a,b; Brooks et al. 2009; Hopkins et al. 2009b; Ceverino et al. 2010). Additionally, Bournaud, Elmegreen & Elmegreen (2007a) and Elmegreen et al. (2009) discuss bulge formation via the merging of clumps forming within very gas rich, turbulent disc in high-redshift galaxies. These bulges can have a range of Sérsic indices, ranging from $n < 2$ to $n = 4$.

As far as the structure of galaxies is concerned, we are still actively studying and debating the epoch and formation pathway for the main stellar components of galaxies, namely flattened, dynamically cold, disc-dominated components (including outer discs, circumnuclear discs, and pseudo-bulges) versus puffy, dynamically hot spheroidal or triaxial bulges/ellipticals. Getting a census of dynamically hot bulges/ellipticals and dynamically cold, flattened disc-dominated components on large and small scales in galaxies provides a powerful way of evaluating the importance of violent bulge-building processes, such as violent relaxation, versus gas-dissipative disc-building processes.

We adopt throughout this paper the widely used definition of a bulge as the excess light above an outer disc in an S0 or spiral galaxy (e.g. Laurikainen et al. 2007, 2009, 2010; Fisher & Drory 2008; Gadotti 2009; Weinzirl et al. 2009). The central bulge falls in three main categories called classical bulges, discy pseudo-bulges (Kormendy 1993; Kormendy & Kennicutt 2004; Athanassoula 2005; Jogee, Scoville & Kenney 2005; Kormendy & Fisher 2005; Fisher & Drory 2008), and boxy pseudo-bulges (Combes & Sanders 1981; Combes et al. 1990; Pfenniger & Norman 1990; Athanassoula 2005; Bureau & Athanassoula 2005; Martinez-Valpuesta, Shlosman & Heller 2006). Some bulges are composite mixtures of the first two classes (Kormendy & Barentine 2010; Barentine & Kormendy 2012). For remainder of the paper we refer to classical bulges simply as 'bulges' when the context is unambiguous.

Numerous observational efforts have been undertaken to derive such a census among galaxies in the field environment. Photometric studies (e.g. Kormendy 1993; Graham 2001; Balcells et al. 2003; Balcells, Graham & Peletier 2007b; Laurikainen et al. 2007; Fisher & Drory 2008; Graham & Worley 2008; Gadotti 2009; Weinzirl et al. 2009; Kormendy et al. 2010) have dissected field galaxies into outer stellar discs and different types of central bulges (classical, discy/boxy pseudo-bulges) associated with different Sérsic index, and compiled the stellar bulge-to-total light or mass ratio (B/T) of spirals and S0s. It is found that low-B/T and bulgeless galaxies are common in the field at low redshifts, both among low-mass or late-type galaxies (Böker et al. 2002; Kautsch et al. 2006; Barazza, Jogee & Marinova 2007, 2008) and among high-mass spirals or early-type spirals (Kormendy 1993; Balcells et al. 2003, 2007b; Laurikainen et al. 2007; Graham & Worley 2008; Gadotti 2009; Weinzirl et al. 2009; Kormendy et al. 2010). Balcells et al. (2003) highlighted the paucity of $r^{1/4}$ profiles in the bulges of early-type disc galaxies. Working on a bigger sample, Weinzirl et al. (2009) report that the majority (66.4 ± 4.4 per cent) of massive ($M_\star \geq 10^{10}$ M$_\odot$) field spirals have low B/T ($\leq$0.2) and bulges with low Sérsic index ($n \leq 2$).

These empirical results can be used to test models of the assembly history of field galaxies. For instance, Weinzirl et al. (2009) find that the results reported above are consistent with hierarchical semi-analytic models of galaxy evolution from Khochfar & Silk (2006) and Hopkins et al. (2009a), which predict that most ($\sim$85 per cent) massive field spirals have had no major merger since $z = 2$. While this work reduces the tension between theory and observations for field galaxies, one should note that hydrodynamical models still face challenges in producing purely bulgeless massive galaxies in different environments.

It is important to extend such studies from the field environment to rich clusters. Hierarchical models predict differences in galaxy merger history as a function of galaxy mass, environment, and redshift (Cole et al. 2000; Khochfar & Burkert 2001). Furthermore, cluster-specific physical processes, such as ram-pressure stripping (Gunn & Gott 1972; Fujita & Nagashima 1999), galaxy harassment (Barnes & Hernquist 1991; Moore et al. 1996, 1999; Hashimoto et al. 1998; Moore, Lake & Katz 1998; Gnedin 2003), and strangulation (Larson, Tinsley & Caldwell 1980), can alter SF history and galaxy stellar components (discs, bulges, bars).

Efforts to establish accurate demographics of galaxy components in clusters are ongoing. In the nearby Virgo cluster, Kormendy et al. (2009) find that more than 2/3 of the stellar mass is in classical bulges/ellipticals, including the stellar mass contribution from M87.[2] Furthermore, there is clear evidence for ongoing

[1] A de Vaucouleurs $r^{1/4}$ profile corresponds to a Sérsic (1968) profile with index $n = 4$.

[2] M87 is considered as a giant elliptical by some authors and as a cD by others. The detection of intracluster light around M87 (Mihos et al. 2005, 2009) strongly supports the view that it is a cD galaxy. In this paper (e.g. Table 6) we consider M87 as a cD when making comparisons (e.g. Section 4.2) to Virgo.

environmental effects in Virgo; see Kormendy & Bender (2012) for a comprehensive review.

Yet Virgo is not very rich compared with more typical clusters (Heiderman et al. 2009). The Coma cluster at $z = 0.024$ ($D = 100$ Mpc) has a central number density 10 000 Mpc^{-3} (The & White 1986) and is the densest cluster in the local Universe. However, ground-based data do not provide high enough resolution (1 arcsec–2 arcsec = 500–1000 pc) for accurate structural decomposition, an obstacle to earlier work.

In this paper we make use of data from the *Hubble Space Telescope* (*HST*) Treasury Survey (Carter et al. 2008) of Coma which provides high-resolution (50 pc) imaging from the Advanced Camera for Surveys (ACS). Our goal is to derive the demographics of galaxy components, in particular classical bulges/ellipticals and flattened disc-dominated components (including both large-scale discs and discy pseudo-bulges), in the Coma cluster, and to compare the results with lower density environments (LDEs) and to theoretical models, to constrain the assembly history of galaxies.

In Section 2 we present our mass-complete sample of cluster galaxies with stellar mass $M_\star \geq 10^9$ M$_\odot$. In Section 3 we describe our structural decomposition strategy. Section 3.1 describes our working assumption in this paper of using Sérsic index as a proxy for tracing the disc-dominated structures and classical bulges/ellipticals. Section 3.2 outlines our procedure for structural decomposition, and we refer the reader to Appendix A for a more detailed description. Section 3.3 overviews the scheme we use to assign morphological types (MT) to galaxies. In Section 4.1, we quantitatively assign galaxy types based on the structural decompositions. We also make a census (Section 4.2) of structures built by dissipation versus violent stellar processes, explore how stellar mass is distributed in different galaxy components (Section 4.3), and consider galaxy scaling relations (Section 4.4). In Section 4.5, we evaluate and discuss the effect of cluster environmental processes. In Section 5 we compare our empirical results with theoretical models, after first identifying Coma-like environments in the simulations. Readers not interested in the complete details about the theoretical model can skip to Sections 5.3 and 5.6. We summarize our results in Section 6.

We adopt a flat Λ cold dark matter cosmology with $\Omega_\Lambda = 0.7$ and $H_0 = 73$ km s^{-1} Mpc^{-1}. We use AB magnitudes throughout the paper, except where indicated otherwise.

2 DATA AND SAMPLE SELECTION

This study is based on the data products from the *HST*/ACS Coma Cluster Treasury Survey (Carter et al. 2008), which provides ACS Wide Field Camera images for 25 pointings spanning 274 arcmin^2 in the *F*475*W* and *F*814*W* filters. The total ACS exposure time per pointing is typically 2677 s in *F*475*W* and 1400 s in *F*814*W*. Most (19/25) pointings are located within 0.5 Mpc from the central cD galaxy NGC 4874, and the other 6/25 pointings are between 0.9 and 1.75 Mpc southwest of the cluster centre. The full width at half-maximum (FWHM) of the ACS point spread function (PSF) is ∼0.1 arcsec (Hoyos et al. 2011), corresponding to ∼50 pc at the 100 Mpc distance of the Coma cluster (Carter et al. 2008). Note that the 19 pointings cover only 19.7 per cent by area of the projected central 0.5 Mpc of Coma. This limited spatial coverage of ACS in the projected central 0.5 Mpc of Coma may introduce a possible bias in the sample due to cosmic variance. We quantify this effect in Appendix B5 and discuss the implications throughout the paper.

Hammer et al. (2010) discuss the images and SExtractor source catalogues for Data Release 2.1 (DR2.1). The *F*814*W* 5σ limit for point sources is 26.8 mag (Hammer et al. 2010), and we estimate the 5σ *F*814*W* surface brightness limit for extended sources within a 0.7 arcsec diameter aperture to be 25.6 mag arcsec^{-2}. Several of the ACS images in DR2.1 suffer from bias offsets on the interchip and/or interquadrant scale that cause difficulty in removing the sky background. We use the updated ACS images reprocessed to reduce the impact of this issue. The DR2.1 images are used where this issue is not present.

2.1 Selection of bright cluster members

We select our sample based on the eyeball catalogue of Trentham et al. (in preparation), with updates from Marinova et al. (2012). This catalogue provides visually determined morphologies and cluster membership status for galaxies with an apparent magnitude $F814W \leq 24$ mag. Morphology classifications in this catalogue come from a combination of RC3 (de Vaucouleurs et al. 1991) and visual inspection. In Section 4.1 we assign Hubble types based only on our own multicomponent decompositions.

Cluster membership is ranked from 0 to 4 following the method of Trentham & Tully (2002). Membership class 0 means the galaxy is a spectroscopically confirmed cluster member. The subset of spectroscopically confirmed cluster members was identified based on published redshifts (Colless & Dunn 1996; Mobasher et al. 2001; Adelman-McCarthy et al. 2008; Chiboucas et al. 2010) and is approximately complete in surface brightness at the galaxy half-light radius ($\mu_{\rm e,\,F814W}$) to ∼22.5 mag arcsec^{-2} (den Brok et al. 2011). The remaining galaxies without spectroscopic confirmation are assigned a rating of 1 (very probable cluster member), 2 (likely cluster member), 3 (plausible cluster member), or 4 (likely background object) based on a visual estimation that also considers surface brightness and morphology.

From this catalogue, we define a sample S1 of 446 cluster members having $F814W \leq 24$ mag and membership rating 0–3 located within the projected central 0.5 Mpc of Coma, which is the projected radius probed by the central ACS pointings. To S1 we add the second central cD galaxy NGC 4889, which is not observed by the ACS data. The majority (179) of S1 galaxies have member class 0, and 30, 131, and 106 have member class 1, 2, and 3, respectively.

2.2 Calculation of stellar masses

Stellar masses are a thorny issue. Uncertainties in the mass-to-light ratios of stellar populations (M/L) arise from a poorly known initial mass function (IMF) as well as degeneracies between age and metallicity. We calculate stellar masses based on the *HST F*475*W* and *F*814*W*-band photometry. First, we convert the *HST* (AB) photometry to the Cousins–Johnson (Vega) system using

$$I = F814W - 0.38 \quad (1)$$

from the WFPC2 Photometry Cookbook and

$$B - I = 1.287\,(F475W - F814W) + 0.538 \quad (2)$$

from Price et al. (2009).

Next, we calculate *I*-band M/L from the calibrations of Into & Portinari (2013) for a Kroupa, Tout & Gilmore (1993) IMF with

$$I_{\rm lum} = 10^{(-0.4(I-35-4.08))} \quad (3)$$

and

$$M_\star = I_{\rm lum} \times 10^{(0.641(B-I)-0.997)}, \quad (4)$$

where I corresponds to the apparent MAG_AUTO SExtractor magnitude,[3] 35 is the distance modulus to Coma, and 4.08 is the solar absolute magnitude in I band.

We use the above method to calculate stellar masses for all galaxies in S1 except NGC 4889, which does not have ACS data. For NGC 4889, we use *gr* Petrosian magnitudes from SDSS Data Release 10 (DR10; Ahn et al. 2013). Stellar masses are determined using the relations of Bell et al. (2003) and assuming a Kroupa IMF, namely

$$g_{\rm lum} = 10^{(-0.4(g-35-5.10))} \quad (5)$$

and

$$M_\star = g_{\rm lum} \times 10^{(-0.499+1.519(g-r)-0.1)}, \quad (6)$$

where g and r are apparent SDSS magnitudes, 35 is the distance modulus to Coma, and 5.10 is the solar absolute magnitude in g band.[4]

It is hard to derive the stellar mass of cD galaxies for several reasons. The stellar M/L ratio of cDs is believed to be high ($M_{\rm dyn}/L_B >$ 100; Schneider 2006), but is very uncertain as most of the light of a cD is in an outer envelope made of intracluster light and galaxy debris. Another problem is that even if one knew the correct stellar M/L ratio, it is likely that the available photometry from ACS and SDSS is missing light from the extended low surface brightness envelope. Given all these factors, it is likely that the above equations, which are typically used to convert colour to $M_\star$ for normal representative galaxies, are underestimating the M/L ratios and stellar masses of the cDs, so that the adopted stellar masses for the cDs ($M_\star \sim 6{-}8 \times 10^{11}$ M$_\odot$) are lower limits. Due to the uncertain stellar masses of the cDs, we present many of our results without them, and we take care to consider them separately from the less massive galaxy population of E, S0, and spiral galaxies.

2.3 Selection of final sample of massive galaxies

The left-hand panels of Fig. 1 show the distributions of $F814W$ magnitudes (upper panel) and stellar masses (lower panels) for sample S1, while in the right-hand panels of the same figure the correlations of stellar masses with $F814W$ magnitudes (upper panel) and $g - r$ colours (lower panel) are shown.

In this paper, we focus on massive ($M_\star \geq 10^9$ M$_\odot$) galaxies. Our rationale is that we are specifically interested in understanding the evolution of the most massive cluster galaxies through comparisons with model clusters (Section 5) which show mass incompleteness at galaxy stellar masses $M_\star < 10^9$ M$_\odot$. We found for sample S1 that imposing the mass cut $M_\star \geq 10^9$ M$_\odot$ effectively removes most galaxies identified in the Trentham et al. catalogue as dwarf/irregular and very low surface brightness galaxies. With this cut, we are left with 75 galaxies that consist primarily of E, S0, and spiral galaxies, two cDs, and only six dwarfs. 3 out of 75 galaxies are significantly cutoff from the ACS detector, and we ignore these sources. Of the remaining 72 galaxies, 69/72 have spectroscopic redshifts. The 3/72 galaxies without spectroscopic redshifts appear too red to be in Coma (Fig. 1d), and the estimated SDSS DR10 photometric redshifts are much larger than the redshift of Coma (0.024). We also neglect these three sources as they are unlikely to be Coma members. Our final working sample S2 consists of the 69 galaxies inside the projected central 0.5 Mpc with stellar mass $M_\star \geq 10^9$ M$_\odot$ and spectroscopic redshifts. Table 1 cross references our sample with other data sets.

3 METHOD AND ANALYSIS

3.1 Using Sérsic index as a proxy for tracing disc-dominated structures and classical bulges/ellipticals

As outlined in Section 1, galaxy bulges and stellar discs hold information on galaxy assembly history. The overall goal in this work is to separate galaxy components into groups of classical bulges/ellipticals versus disc-dominated structures.

It is common practice (e.g. Laurikainen et al. 2007; Gadotti 2009; Weinzirl et al. 2009) to characterize galaxy structures (bulges, discs, and bars) with generalized ellipses whose radial light distributions are described by the Sérsic (1968) profile:

$$I(r) = I_{\rm e} \exp\left(-b_{\rm n}\left[\left(\frac{r}{r_{\rm e}}\right)^{1/n} - 1\right]\right), \quad (7)$$

where I_e is the surface brightness at the effective radius $r_{\rm e}$ and b_n [5] is a constant that depends on Sérsic index n.

In this paper, we adopt the working assumption that in intermediate and high-mass ($M_\star \geq 10^9$ M$_\odot$) galaxies, a low Sérsic index n below a threshold value $n_{\rm disc\_max}$ corresponds to a dynamically cold disc-dominated structure. Note we specify 'disc-dominated' rather than 'pure disc' as we refer to barred discs and thick discs. While this assumption is not necessarily waterproof, it is based on multiple lines of compelling evidence that are outlined below.

(i) Freeman (1970) showed that many large-scale discs of S0 and spiral galaxies are characterized by an exponential light profile (Sérsic index $n = 1$) over 4–6 disc scalelengths. Since then, it has become standard practice in studies of galaxy structure to model the outer disc of S0s and spirals with an exponential profile (e.g. Kormendy 1977; Boroson 1981; Kent 1985; Byun & Freeman 1995; de Jong 1996; Baggett, Baggett & Anderson 1998; Allen et al. 2006; Laurikainen et al. 2007; Gadotti 2009; Weinzirl et al. 2009).

(ii) On smaller scales, flattened, rotationally supported inner discs with high V/σ (i.e. discy pseudo-bulges) have been associated with low Sérsic index $n \lesssim 2$ (Kormendy 1993; Kormendy & Kennicutt 2004; Athanassoula 2005; Jogee et al. 2005; Kormendy & Fisher 2005; Fisher & Drory 2008; Fabricius et al. 2012). This suggests $n_{\rm disc\_max}$ should be close to 2.
Fabricius et al. (2012) explore the major-axis kinematics of 45 S0–Scd galaxies with high-resolution spectroscopy. They demonstrate a systematic agreement between the shape of the velocity dispersion profile and the bulge type as indicated by the Sérsic index. Low Sérsic index bulges have both increased rotational support (higher $\langle V^2\rangle/\langle\sigma^2\rangle$ values) and on average lower central velocity dispersions. Classical bulges (discy pseudo-bulges) have centrally peaked (flat) velocity dispersion profiles whether identified visually or by a high Sérsic index.

[3] For galaxies COMAi125935.698p275733.36 = NGC 4874 and COMAi125931.103p275718.12, SExtractor vastly underestimates the total $F814W$ luminosity, and the calculation is instead made with the total luminosity derived from structural decomposition (Section 3.2).
[4] The Kroupa IMF offset term reported as −0.15 in Bell et al. (2003) was calculated assuming unrealistic conditions (Bell, private communication). The correct value is −0.1 and is used in Borch et al. (2006).

[5] The precise values of b_n are given from the roots of the equation $\Gamma(2n) - 2\gamma(2n, b_n) = 0$, where Γ is the gamma function and γ is the incomplete gamma function.

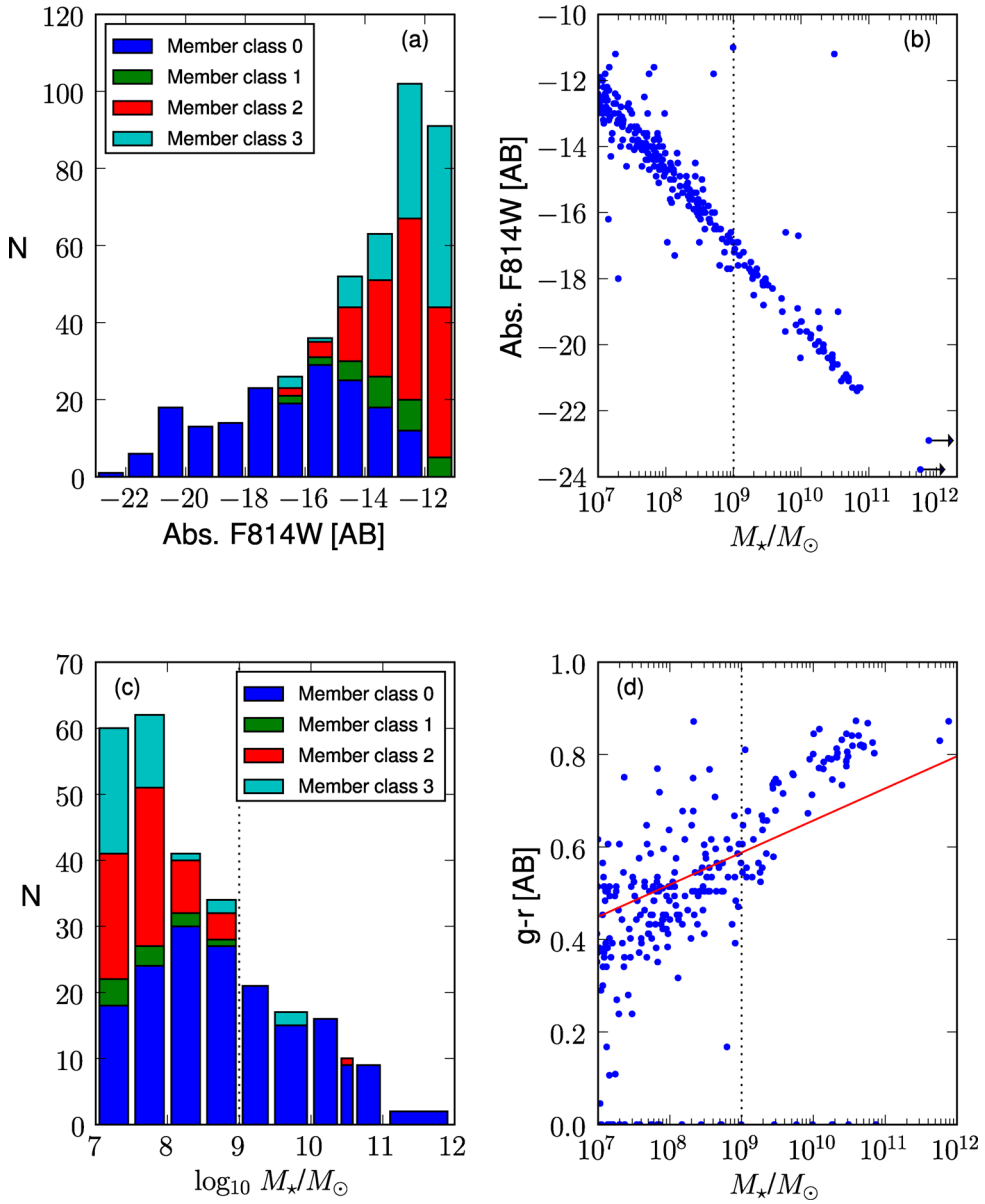

Figure 1. Shows in panels (a) to (d) the luminosity, stellar mass, and $g - r$ colour, respectively, for the 446 galaxies in sample S1 having $F814W \leq 24$, locations within the projected central 0.5 Mpc of the Coma cluster, and cluster membership rating 0–3, where rating 0 means spectroscopically confirmed and ratings 1–3 indicate increasingly less likely cluster membership. See Section 2.1 for details. In panel (b), the two most massive sources are cD galaxies, and the arrows indicate their adopted stellar masses are lower limits (Section 2.2). The solid line in panel (d) is the colour–luminosity break between the red and blue sequence of galaxies from Blanton et al. (2005), which we convert from luminosity to stellar mass using the relations of Bell et al. (2003). The dotted line in panels (b)–(d) indicates our main sample of 69 spectroscopically confirmed members with $M_\star \geq 10^9$ M$_\odot$.

(iii) At high ($z \sim 2$) redshift, where it is not yet possible to fully resolve galaxy substructures, it has become conventional to use the global Sérsic index $n \lesssim 2$ in massive galaxies to separate disc-dominated versus bulge-dominated galaxies (e.g. Ravindranath et al. 2004; van der Wel et al. 2011; Weinzirl et al. 2011). Weinzirl et al. (2011) further explore the distributions of ellipticities ($1 - b/a$) for the massive $z \sim 2$ galaxies with low ($n \leq 2$) and high ($n > 2$) global Sérsic index. They find galaxies with low global Sérsic index $n \leq 2$ have a distribution of projected ellipticities more similar to massive $z \sim 0$ spirals than to massive $z \sim 0$ ellipticals.

The above does not allow for low-n, dynamically hot structures. A low-n dynamically hot structure would be considered in our study as a pure photometric disc, a low-n bulge, or an unbarred S0 galaxy. The error due to misunderstood objects in the first two groups is expected to be small or non-existent. There is only one pure photometric disc in the sample (Section 4.1) and low-n bulges ($N = 20$) only make up 2.2 per cent of galaxy stellar mass (excluding the cDs, Section 4.2). Furthermore, fig. 15 of Fabricius et al. (2012) shows that no low-n bulge turns out to be dynamically hot.

There are 20 unbarred S0 galaxies in our sample, and these account for 18.5 per cent of the galaxy stellar mass (excluding the cD galaxies). About 75 per cent of these objects have stellar mass and luminosity consistent with dwarf spheroidal galaxies (Kormendy et al. 2009). Even if some of these systems are actually dwarf spheroidals, they may not be dynamically hot as some studies

Table 1. Cross identifications.

Galaxy name (1)	SDSS DR8 name (2)	2MASS XSC (or PSC name) (3)	GMP name (4)	Dressler (1980) name (5)
COMAi125926.458p275124.81	1237667444048658752	–	GMP3473	–
COMAi13007.123p275551.49	1237667444048724242	2MASSJ13000711+2755511	GMP2931	–
COMAi125930.270p28115.17	1237667324334571563	–	GMP3406	–
COMAi125937.200p275819.97	1237667444048658537	2MASSJ12593720+2758203	GMP3308	–
COMAi125953.929p275813.75	1237667444048658918	–	GMP3098	–
COMAi13018.351p28333.32	1237667324334637348	–	GMP2787	–
COMAi125937.010p28106.95	1237667324334571551	2MASSJ12593699+2801074	GMP3312	–
COMAi125946.943p275930.90	1237667324334571832	2MASSJ12594688+2759308	GMP3166	–
COMAi13030.954p28630.22	1237667324334637213	2MASSJ13003091+2806300	GMP2626	–
COMAi13035.420p275634.06	1237667444048724352	–	GMP2585	–
COMAi125950.183p275445.52	1237667444048658912	–	GMP3131	–
COMAi125959.476p275626.02	1237667444048658878	–	GMP3034	–
COMAi13000.949p275643.85	1237667444048658882	2MASSJ13000095+2756433	GMP3017	–
COMAi13034.430p275604.95	1237667444048724349	2MASSJ13003442+2756047	GMP2591	–
COMAi125931.893p275140.76	1237667444048658763	2MASSJ12593186+2751406	GMP3383	–
COMAi125931.103p275718.12	1237667444048658549	–	GMP3392	–
COMAi13041.193p28242.34	1237667324334702866	2MASSJ13004119+2802424	GMP2529	–
COMAi125845.533p274513.75	1237667323797635368	2MASSJ12584558+2745132	GMP4035	–
COMAi13018.545p28549.62	1237667324334637356	2MASSJ13001857+2805503	GMP2784	–
COMAi13021.673p275354.81	1237667444048724303	2MASXJ13002172+2753545	GMP2736	–
COMAi13024.823p275535.94	1237667444048724320	2MASSJ13002482+2755353	GMP2692	–
COMAi13051.149p28249.90	1237667324334702708	2MASSJ13005112+2802499	GMP2423	–
COMAi13011.143p28354.91	1237667324334637325	2MASSJ13001117+2803551	GMP2879	–
COMAi125937.990p28003.52	1237667324334571647	2MASSJ12593798+2800036	GMP3292	–
COMAi13018.873p28033.38	1237667324334637362	2MASXJ13001890+2800332	GMP2777	–
COMAi125911.543p28033.32	1237667324334506328	2MASSJ12591153+2800334	GMP3681	–
COMAi125904.797p28301.16	1237667324334506316	2MASXJ12590475+2803019	GMP3780	–
COMAi125909.468p28227.35	1237667324334506325	2MASXJ12590943+2802279	GMP3707	–
COMAi125935.286p275149.13	1237667444048658774	2MASXJ12593524+2751488	GMP3339	–
COMAi13005.405p28128.14	1237667324334637091	2MASXJ13000538+2801282	GMP2960	–
COMAi125950.105p275529.44	1237667444048658822	2MASXJ12595013+2755292	GMP3133	–
COMAi13018.772p275613.34	1237667444048723991	2MASXJ13001877+2756135	GMP2778	–
COMAi125938.321p275913.89	1237667444048658535	2MASXJ12593827+2759137	GMP3291	D154
COMAi125940.270p275805.71	1237667444048658530	2MASSJ12594026+2758058	GMP3254	D127
COMAi125944.208p275730.38	1237667444048658531	2MASXJ12594423+2757307	GMP3206	D126
COMAi125939.659p275714.03	1237667444048658528	2MASSJ12593965+2757141	GMP3269	D128
COMAi13044.632p28602.31	1237667324334702891	2MASXJ13004459+2806026	GMP2489	D191
COMAi125928.721p28225.92	1237667324334571539	2MASXJ12592868+2802258	GMP3433	D177
COMAi125942.301p275529.15	1237667444048658653	2MASXJ12594234+2755287	GMP3222	D125
COMAi13017.014p28350.07	1237667324334637347	2MASXJ13001702+2803502	GMP2805	D171
COMAi125956.697p275548.71	1237667444048658858	2MASXJ12595670+2755483	GMP3068	D123
COMAi13016.534p275803.15	1237667444048723984	2MASXJ13001655+2758032	GMP2815	D122
COMAi13006.395p28015.94	1237667324334637086	2MASXJ13000643+2800142	GMP2940	D150
COMAi13027.966p275721.56	1237667444048724118	2MASXJ13002798+2757216	GMP2654	D119
COMAi13012.868p28431.74	1237667324334637140	2MASXJ13001286+2804322	GMP2861	D173
COMAi125943.721p275940.82	1237667324334571645	2MASSJ12594372+2759409	GMP3213	D153
COMAi13028.370p275820.64	1237667444048724328	2MASXJ13002835+2758206	GMP2651	D147
COMAi13042.832p275746.95	1237667444048724176	2MASXJ13004285+2757476	GMP2510	D116
COMAi13038.761p28052.34	1237667324334702605	2MASXJ13003877+2800516	GMP2551	D146
COMAi13014.746p28228.69	1237667324334637152	2MASXJ13001475+2802282	GMP2839	D172
COMAi13022.170p28249.30	1237667324334637189	2MASXJ13002215+2802495	GMP2727	D170
COMAi125931.453p28247.60	1237667324334571535	2MASXJ12593141+2802478	GMP3390	D176
COMAi13018.093p275723.59	1237667444048723985	2MASSJ13001809+2757235	GMP2794	D120
COMAi13040.838p275947.80	1237667324334702869	2MASXJ13004081+2759476	GMP2535	D145
COMAi125852.097p274706.15	1237667323797635203	2MASXJ12585208+2747059	GMP3958	D072
COMAi125946.782p275825.99	1237667444048658525	2MASXJ12594681+2758252	GMP3170	D152
COMAi13008.003p28442.81	1237667324334637131	2MASXJ13000803+2804422	GMP2922	D174
COMAi125929.956p275723.26	1237667444048658522	2MASSJ12592995+2757231	GMP3414	D131
COMAi125929.403p275100.46	1237667444048658609	2MASXJ12592936+2751008	GMP3423	D088
COMAi125932.771p275901.04	1237667444048658523	2MASXJ12593276+2759008	GMP3367	D155
COMAi125944.407p275444.84	1237667444048658654	2MASXJ12594438+2754447	GMP3201	D124
COMAi125930.824p275303.05	1237667444048658616	2MASXJ12593079+2753028	GMP3400	D103
COMAi13039.767p275526.19	1237667444048724135	2MASXJ13003975+2755256	GMP2541	D118

Table 1 – *continued*

Galaxy name (1)	SDSS DR8 name (2)	2MASS XSC (or PSC name) (3)	GMP name (4)	Dressler (1980) name (5)
COMAi13042.766p275817.38	1237667324334702622	2MASXJ13004277+2758166	GMP2516	D144
COMAi13048.646p28526.69	1237667324334702681	2MASXJ13004867+2805266	GMP2440	D168
COMAi13017.683p275718.93	1237667444048723981	2MASXJ13001768+2757192	GMP2798	D121
COMAi13051.464p28234.86	1237667324334702705	2MASXJ13005158+2802341	GMP2417	D167
NGC 4889	1237667444048723983	2MASXJ13000809+2758372	GMP2921	D148
COMAi125935.698p275733.36 (NGC 4874)	1237667444048658532	2MASXJ12593570+2757338	GMP3329	D129

Notes. If there is no match in the 2MASS Extended Source catalogue (2MASX), where available, the 2MASS Point Source catalogue name (2MASS) is given in column (3). GMP name refers to the Godwin, Metcalfe & Peach (1983) catalogue.

(e.g. Kormendy et al. 2009, Kormendy & Bender 2012) claim that many dwarfs are actually disc systems closely related to dIrr, which have been stripped of gas via supernova feedback or environmental effects. The remaining 25 per cent would be misclassified elliptical galaxies as they are too bright and massive to be dwarfs. Note, however, that fig. 33 of Kormendy et al. (2009) shows that elliptical galaxies with $M_V < -18$ and Sérsic $n < 2$ are very rare. In the worse-case scenario that all of our unbarred S0 galaxies are dynamically hot structures, our measurement of the dynamically hot stellar mass in Section 4.2 would be too low by ∼30 per cent.

The second natural related working assumption in our paper is that in intermediate and high-mass ($M_\star \geq 10^9$ M$_\odot$) galaxies, components with Sérsic $n > n_{\rm disc\_max}$ are classical bulge/elliptical components (defined in Section 1). Such bulges/ellipticals are formed by the redistribution of stars during major and minor galaxy collisions. *N*-body simulations show that minor mergers consistently raise the bulge Sérsic index (Aguerri, Balcells & Peletier 2001; Eliche-Moral et al. 2006; Naab & Trujillo 2006). The effect of successive minor mergers is cumulative (Aguerri et al. 2001; Bournaud, Jog & Combes 2007b; Naab, Johansson & Ostriker 2009; Hilz et al. 2012).

We empirically set $n_{\rm disc\_max}$ to 1.66 based on looking at the Sérsic n of outer discs in those Coma galaxies that are barred, and by definition, must harbour outer disc since bars are disc features. Appendices B2 and D discuss the empirical details behind this choice.

3.2 Overview of our structural decomposition procedure

For our mass-complete sample of 69 intermediate-to-high mass ($M_\star \geq 10^9$ M$_\odot$) galaxies, we use deep, high-resolution (0.1 arcsec or 50 pc), *F*814*W*-band images of Coma from *HST*/ACS, which allow for accurate structural decomposition. We fit galaxies with one, two, or three Sérsic profiles, plus a nuclear point source, when needed (see Appendix A for details). We use GALFIT (Peng et al. 2002). In a model with one or more Sérsic profiles, there is expected to be coupling between the free parameters, particularly $r_{\rm e}$ and n, although most previous studies have generally ignored this effect. Weinzirl et al. (2009) explore the issue of parameter coupling for barred and unbarred spiral galaxies.

We take some precautions to ensure accurate decompositions.

(i) We fit all structures with a generalized Sérsic profile where the Sérsic index is a free parameter (Section 3.3). This limits the number of a priori assumptions on the physical nature or shape of galaxy structures.

(ii) In clusters, the featureless (i.e. no spiral arms delineated by young stars, rings of SF, or gas/dust lanes) outer discs of gas-poor S0s are not readily distinguished from the equally featureless outer stellar components of classical ellipticals. We do this in essence by applying $n_{\rm disc\_max}$ to the Sérsic index n of the outer galaxy structure.

(iii) Not requiring outer discs to have an exponential $n = 1$ profile accommodates non-exponential disc structures (e.g. discs with down-bending truncations or up-bending antitruncations; Freeman 1970; van der Kruit 1979; van der Kruit & Searle 1981a,b; de Grijs, Kregel & Wesson 2001; Pohlen et al. 2002; Matthews & Gallagher 1997; Erwin, Beckman & Pohlen 2005; Pohlen & Trujillo 2006; Maltby et al. 2012) that are rotationally supported.

(iv) Stellar bars, ovals/lenses, and nuclear point sources are modelled when needed, which is critical for obtaining a reliable characterization of the bulge (e.g. Balcells et al. 2003; Laurikainen et al. 2005, 2007; Weinzirl et al. 2009).

Our structural decomposition scheme and decision sequence are described in detail in Appendix B, illustrated in Figs 2 and 3, and briefly outlined below.

(i) *Stage 1 (single Sérsic fitted with nuclear point source if needed)*. The single Sérsic model is adopted if either the galaxy does not show any coherent structures (e.g. inner/outer discs, bars, bulges, rings, or spiral arms) indicating the need for additional Sérsic components, or, alternatively, if the galaxy has a core – a light profile that deviates downward from the inward extrapolation of the Sérsic profile (see Appendix C). Such galaxies are interpreted as photometric ellipticals if the single Sérsic index is above a threshold value $n_{\rm disc\_max}$ associated with discs (Section 3.1, Appendices B2 and D); otherwise they are considered photometric discs. Three galaxies show convincing evidence for being cores, and these are luminous objects with high single Sérsic $n > n_{\rm disc\_max}$ (see Appendix B2, Table 2, and Appendix C). The results of Stage 1 are listed in Table 3. See Appendix B1 for additional details on the single Sérsic fits.

(ii) *Stage 2 (double Sérsic model with nuclear point source if needed)*. Galaxies showing coherent structure in the Stage 1 residuals are subjected to a two-component Sérsic + Sérsic fit, with nuclear point source if needed (see Fig. 3). This two-component model is intended to model the inner (C1) and outer (C2) galaxy structures.

There are two possible outcomes. (a) If the outer component C2 is an outer disc based on having Sérsic index $n \leq n_{\rm disc\_max}$, then the galaxy is considered a spiral or S0 with an outer disc having a photometric bulge and, in some cases, a large-scale bar. (b) If the outer component C2 does not meet our definition of an outer disc, then the galaxy is considered a photometric elliptical having an outer component C2 with $n > n_{\rm disc\_max}$ and an inner component C1 of any n. See Appendix B2 for details.

(iii) *Stage 3 (triple Sérsic model with nuclear point source if needed)*. Case (a) in Stage 2 identifies spiral and S0 galaxies with

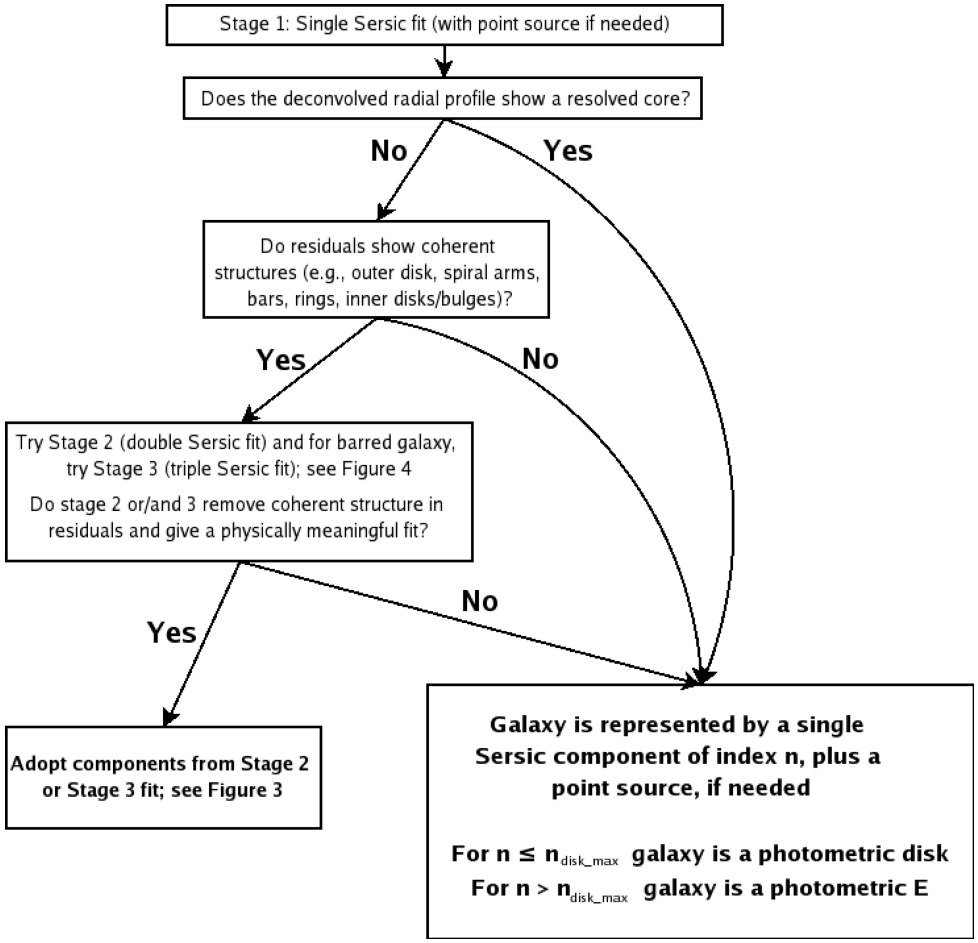

Figure 2. Provides an overview of our structural decomposition method. All galaxies are subjected to Stage 1, and most are further processed in Stage 2. A galaxy best fitted with a single Sérsic profile plus point source (if needed) is interpreted as a photometric elliptical or photometric disc. A galaxy with extra coherent structure that cannot be described with a single Sérsic profile is subjected to a multiple-component fit in Stage 2 and, if needed, Stage 3. Fig. 3 describes Stage 2 and Stage 3 in more detail.

an outer disc. These galaxies are further processed as follows. (a) If there is evidence for a large-scale bar (see Appendix B2), then a triple Sérsic profile is fitted in Stage 3 for the photometric bulge, disc, and bar. (b) Otherwise, the galaxy is considered as unbarred and the double Sérsic fit for a photometric bulge and disc is adopted. In both cases (a) and (b), it is important to note that the photometric bulge is allowed to have any Sérsic index n, thus allowing for structures with $n \leq n_{\rm disc\_max}$ and structures with $n > n_{\rm disc\_max}$.

3.3 Overview of our galaxy classification scheme

The decomposition scheme discussed above and in Figs 2 and 3 leads naturally to the galaxy classification system outlined in Fig. 4, where there are five main galaxy types, G1 to G5. Systems best fitted by single Sérsic models (plus a nuclear point source if present) represent galaxies of type G1 and G2. Systems best fitted by two or three Sérsic profiles (plus a nuclear point source if present) represent galaxies of type G3 to G5.

(i) G1. Photometric disc with $n \leq n_{\rm disc\_max}$ (plus a nuclear point source if present).

(ii) G2. Photometric elliptical with $n > n_{\rm disc\_max}$ (plus a nuclear point source if present).

(iii) G3. Unbarred S0 or spiral having an outer disc with $n \leq n_{\rm disc\_max}$ and an inner photometric bulge of any n (plus a nuclear point source if present).

(iv) G4. Barred S0 or spiral having an outer disc with $n \leq n_{\rm disc\_max}$, a bar, and an inner photometric bulge of any n (plus a nuclear point source if present).

(v) G5. Photometric elliptical having an outer component with $n > n_{\rm disc\_max}$ and an inner component of any n.

This galaxy classification scheme has multiple advantages. First, it allows us to identify low-n disc-dominated structures within galaxies, both on large scales and in the central regions, in the form of outer discs with $n \leq n_{\rm disc\_max}$ in spirals and S0s, photometric bulges with $n \leq n_{\rm disc\_max}$ in spirals and S0s (representing discy pseudo-bulges), and inner discs within ellipticals represented by a component C1 having $n \leq n_{\rm disc\_max}$. Furthermore, it allows a census of galaxy components with $n > n_{\rm disc\_max}$ more akin to classical bulges/ellipticals. Our scheme does not allow for low-n dynamically hot components. As discussed in Section 3.1, this is not a problem because in our sample such structures are not expected to be present in large numbers.

Table 4 lists the distribution of best-fitting models for the sample of galaxies with stellar mass $M_\star \geq 10^9$ M$_\odot$, and the breakdown of galaxies into classes G1 to G5. Table 5 lists the structural parameters

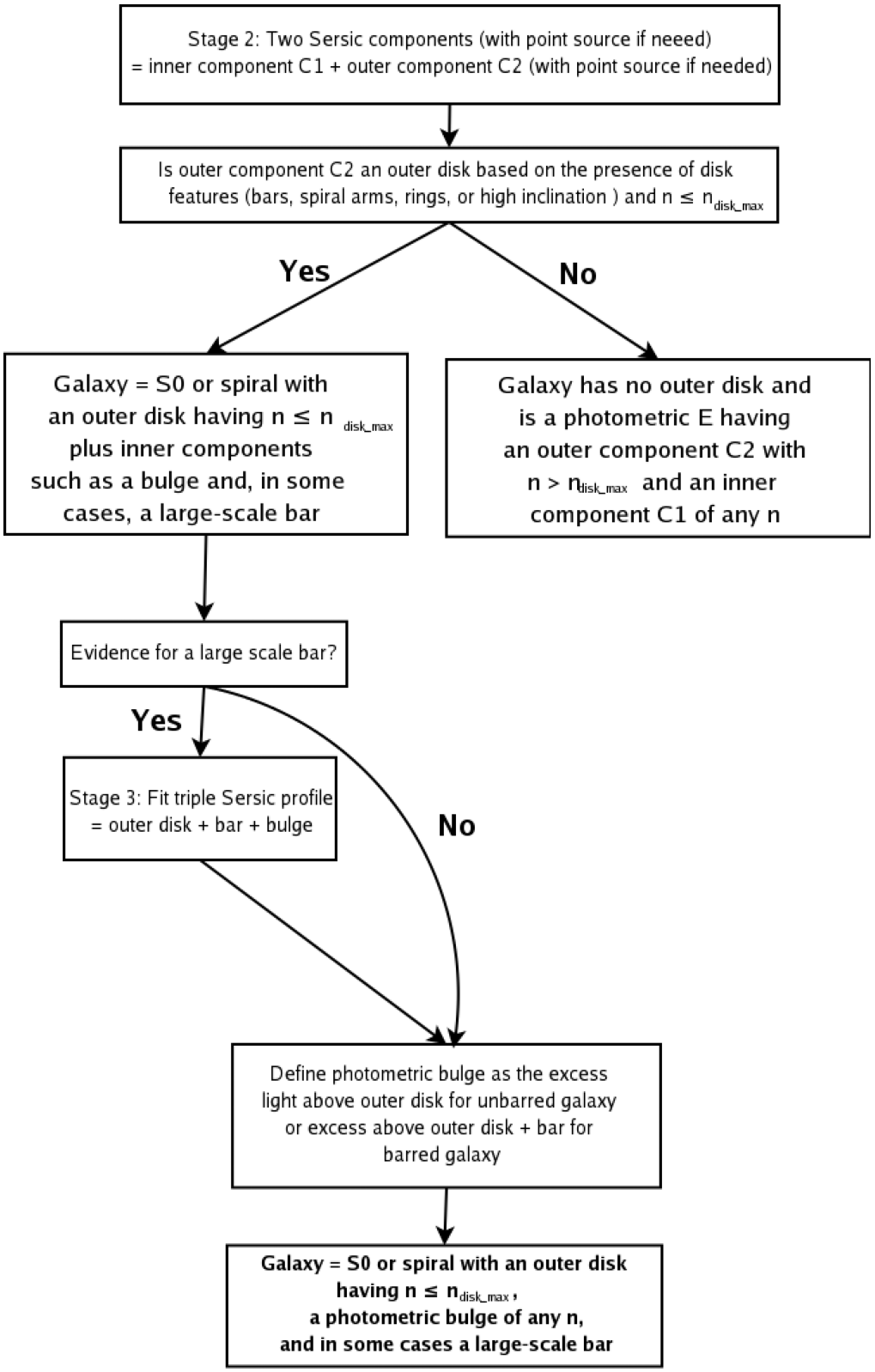

Figure 3. Shows the steps following stages 2 and 3 from Fig. 2. A galaxy without an extended outer disc is interpreted as a photometric E, while a galaxy with such a disc is labelled either an S0 or spiral. When evidence for a large-scale bar is found in a galaxy with an outer disc, Stage 3 is used to model the bar component.

Table 2. Properties of cored ellipticals.

Galaxy name	Core Sérsic (γ, r_b)	2D Sérsic profile w/o core masked (n, r_e)	2D Sérsic profile w/o core masked (n, r_e)
(1)	(2)	(3)	(4)
COMAi125909.468p28227.35	(0.16, 0.13 arcsec)	(2.54, 4.2)	(2.54, 4.20 arcsec)
NGC 4874 (ACS *F*814*W*)	(0.15, 1.40 arcsec)	(2.89, 35.4 arcsec)	(11.4, 875.0 arcsec)
NGC 4874 (SDSS *i* band)	(0.15, 2.32 arcsec)	(4.30, 88.3 arcsec)	(4.70, 107.0 arcsec)
NGC 4889 (SDSS *i* band)	(0.06, 1.88 arcsec)	(3.90, 42.9 arcsec)	(7.80, 129.0 arcsec)

Notes. Galaxies are identified as having a core following the procedure in Appendix C. Two of the cored galaxies (NGC 4874 and NGC 4889) are cD galaxies.

Table 3. Galaxy properties and single Sérsic profile structural parameters.

Galaxy name	RA	Dec.	$M_\star$ ($M_\odot$)	*F*814*W* magnitude	r_e (kpc)	n
(1)	(2)	(3)	(4)	(5)	(6)	(7)
COMAi125926.458p275124.81	194.860 245	27.856 893	1.03e+09	17.43	0.97	1.88
COMAi13007.123p275551.49	195.029 679	27.930 971	1.03e+09	17.42	0.62	2.76
COMAi125930.270p28115.17	194.876 126	28.020 883	1.05e+09	17.46	1.04	1.90
COMAi125937.200p275819.97	194.905 001	27.972 214	1.12e+09	17.68	0.29	4.51
COMAi125953.929p275813.75	194.974 706	27.970 489	1.17e+09	17.41	1.10	1.30
COMAi13018.351p28333.32	195.076 465	28.059 258	1.17e+09	17.13	1.32	1.23
COMAi125937.010p28106.95	194.904 209	28.018 598	1.23e+09	17.34	0.69	2.08
COMAi125946.943p275930.90	194.945 597	27.991 917	1.40e+09	17.02	1.49	1.65
COMAi13030.954p28630.22	195.128 977	28.108 396	1.46e+09	17.07	1.41	1.94
COMAi13035.420p275634.06	195.147 586	27.942 797	1.72e+09	16.83	1.92	1.81
COMAi125950.183p275445.52	194.959 098	27.912 647	1.81e+09	16.95	1.57	1.41
COMAi125959.476p275626.02	194.997 820	27.940 564	1.83e+09	16.53	2.41	2.30
COMAi13000.949p275643.85	195.003 956	27.945 514	1.92e+09	16.40	2.00	3.38
COMAi13034.430p275604.95	195.143 461	27.934 709	1.94e+09	16.65	2.11	2.10
COMAi125931.893p275140.76	194.882 888	27.861 324	1.96e+09	16.78	0.94	1.88
COMAi125931.103p275718.12	194.879 597	27.955 035	1.99e+09	16.87	2.47	1.61
COMAi13041.193p28242.34	195.171 639	28.045 097	2.15e+09	16.83	0.86	1.66
COMAi125845.533p274513.75	194.689 724	27.753 820	2.21e+09	16.56	2.14	2.09
COMAi13018.545p28549.62	195.077 272	28.097 119	2.25e+09	16.64	1.62	1.73
COMAi13021.673p275354.81	195.090 308	27.898 559	2.71e+09	16.37	1.46	2.57
COMAi13024.823p275535.94	195.103 430	27.926 652	2.73e+09	16.41	2.68	2.15
COMAi13051.149p28249.90	195.213 122	28.047 197	2.78e+09	15.52	5.35	3.17
COMAi13011.143p28354.91	195.046 429	28.065 253	2.83e+09	16.38	1.42	2.12
COMAi125937.990p28003.52	194.908 292	28.000 979	2.97e+09	16.53	1.16	2.00
COMAi13018.873p28033.38	195.078 639	28.009 273	2.98e+09	16.58	0.38	3.29
COMAi125911.543p28033.32	194.798 099	28.009 258	3.26e+09	16.40	1.22	1.84
COMAi125904.797p28301.16	194.769 991	28.050 323	3.78e+09	16.09	2.16	2.28
COMAi125909.468p28227.35	194.789 451	28.040 932	5.14e+09	15.94	1.88	2.54
COMAi125935.286p275149.13	194.897 029	27.863 650	5.27e+09	15.96	1.06	1.54
COMAi13005.405p28128.14	195.022 521	28.024 486	8.40e+09	15.11	2.61	2.58
COMAi125950.105p275529.44	194.958 773	27.924 845	8.88e+09	15.62	1.35	2.32
COMAi13018.772p275613.34	195.078 218	27.937 041	9.56e+09	15.09	3.23	2.57
COMAi125938.321p275913.89	194.909 675	27.987 192	9.96e+09	14.93	3.67	3.50
COMAi125940.270p275805.71	194.917 794	27.968 254	1.01e+10	15.04	2.52	5.94
COMAi125944.208p275730.38	194.934 203	27.958 439	1.20e+10	14.60	3.55	3.89
COMAi125939.659p275714.03	194.915 246	27.953 900	1.21e+10	15.05	1.33	3.65
COMAi13044.632p28602.31	195.185 968	28.100 644	1.38e+10	14.86	1.82	2.84
COMAi125928.721p28225.92	194.869 671	28.040 534	1.39e+10	14.95	1.67	2.97
COMAi125942.301p275529.15	194.926 256	27.924 765	1.61e+10	14.56	1.16	7.49
COMAi13017.014p28350.07	195.070 896	28.063 911	1.79e+10	14.75	1.35	3.91
COMAi125956.697p275548.71	194.986 241	27.930 200	1.82e+10	14.35	4.71	3.80
COMAi13016.534p275803.15	195.068 895	27.967 542	1.84e+10	14.24	2.98	4.58
COMAi13006.395p28015.94	195.026 649	28.004 430	1.87e+10	13.82	5.01	7.52
COMAi13027.966p275721.56	195.116 526	27.955 989	2.11e+10	14.51	1.55	4.68
COMAi13012.868p28431.74	195.053 620	28.075 485	2.11e+10	14.52	1.40	3.21
COMAi125943.721p275940.82	194.932 172	27.994 675	2.13e+10	14.48	1.38	3.81
COMAi13028.370p275820.64	195.118 212	27.972 400	2.17e+10	14.24	4.29	4.04
COMAi13042.832p275746.95	195.178 470	27.963 042	2.49e+10	14.17	2.70	4.47

Table 3 – *continued*

Galaxy name	RA	Dec.	$M_\star$ ($M_\odot$)	$F814W$ magnitude	r_e (kpc)	n
(1)	(2)	(3)	(4)	(5)	(6)	(7)
COMAi13038.761p28052.34	195.161 508	28.014 541	2.51e+10	13.87	5.34	4.31
COMAi13014.746p28228.69	195.061 442	28.041 304	2.88e+10	14.06	1.58	4.70
COMAi13022.170p28249.30	195.092 378	28.047 029	2.88e+10	13.84	2.97	4.08
COMAi125931.453p28247.60	194.881 057	28.046 557	2.88e+10	14.22	1.82	2.84
COMAi13018.093p275723.59	195.075 391	27.956 554	2.89e+10	14.41	1.27	2.41
COMAi13040.838p275947.80	195.170 159	27.996 612	2.97e+10	14.00	3.15	3.27
COMAi125852.097p274706.15	194.717 073	27.785 042	3.05e+10	14.02	1.90	3.29
COMAi125946.782p275825.99	194.944 929	27.973 886	3.44e+10	13.83	3.38	4.33
COMAi13008.003p28442.81	195.033 348	28.078 560	3.51e+10	14.10	1.13	2.59
COMAi125929.956p275723.26	194.874 818	27.956 462	3.92e+10	13.32	3.85	4.89
COMAi125929.403p275100.46	194.872 516	27.850 130	4.26e+10	13.87	1.68	4.07
COMAi125932.771p275901.04	194.886 550	27.983 624	4.49e+10	13.20	5.50	5.86
COMAi125944.407p275444.84	194.935 031	27.912 457	4.62e+10	13.67	2.26	2.96
COMAi125930.824p275303.05	194.878 435	27.884 182	5.02e+10	13.61	1.54	3.77
COMAi13039.767p275526.19	195.165 696	27.923 943	5.02e+10	13.44	2.93	3.64
COMAi13042.766p275817.38	195.178 194	27.971 495	5.73e+10	13.43	2.37	4.00
COMAi13048.646p28526.69	195.202 693	28.090 749	6.69e+10	13.30	2.21	3.02
COMAi13017.683p275718.93	195.073 683	27.955 259	7.06e+10	13.28	2.13	2.85
COMAi13051.464p28234.86	195.214 436	28.043 019	7.48e+10	13.07	2.85	3.92
NGC 4889	195.033 750	27.977 000	5.78e+11	10.57	22.65	4.37
COMAi125935.698p275733.36 (NGC 4874)	194.898 743	27.959 269	7.69e+11	10.96	17.35	3.05

Notes. Rows are sorted by increasing $M_\star$.

from the best single or multicomponent model. In summary, we fit 6, 38, and 25 galaxies with 1, 2, and 3 Sérsic profiles, respectively. Our best-fitting models have reduced χ^2 of the order of 1. In terms of galaxy types G1 to G5, we assign 1, 5, 24, 25, and 14 objects to classes G1, G2, G3, G4, and G5, respectively. The number of Stage 3 fits implies that the bar fraction among galaxies with an extended outer disc is 50.0 ± 7.1 per cent, and this is consistent with the bar fraction in Coma derived by Marinova et al. (2012).

4 EMPIRICAL RESULTS ON GALAXY STRUCTURE

4.1 Galaxy types and morphology–density relation in the centre of Coma

We next map classes G1 to G5 to more familiar Hubble types, namely cD, photometric E, S0, and spiral. The Hubble types assigned here depend only on the morphology classes (G1 to G5) associated with structural decomposition; they are independent of the MT from the Trentham et al. (in preparation) catalogue discussed in Section 2. The results are shown in Table 4, and this process is explained in detail below.

The one object in class G1 (photometric disc) has a single Sérsic index $n \leq n_{\rm disc\_max}$ and a nuclear point source. This object has no visible spiral arms, so it is an S0. Objects assigned to class G2 (photometric ellipticals) have single Sérsic index $n > n_{\rm disc\_max}$ and include two known central cD galaxies, NGC 4874 and NGC 4889. We label these two sources separately as cD galaxies because they contain a disproportionately large fraction of the stellar mass. Classes G3 (unbarred S0, spiral) and G4 (barred S0, spiral) represent S0 or spiral disc galaxies with a possible large-scale bar. We label the six galaxies in either class G3 or G4 showing spiral arms in the data or residual images as spirals, while the remaining sources are labelled S0. Class G5 objects are identified as photometric ellipticals having an outer component with $n > n_{\rm disc\_max}$ and an inner component of any n.

Considering the Hubble types assigned above, we find evidence of a strong absence of spiral galaxies. In the projected central 0.5 Mpc of the Coma cluster, there are two cDs (NGC 4874 and NGC 4889), spirals are rare, and the morphology breakdown of (E+S0):spirals is (25.3 per cent+65.7 per cent):9.0 per cent by numbers and (32.0 per cent+62.2 per cent):5.8 per cent by stellar mass. Note that our ratio of E-to-S0 galaxies is lower than found elsewhere for Coma (e.g. Gavazzi et al. 2003) and for other clusters (e.g. Dressler 1980; Fasano et al. 2000; Poggianti et al. 2009), where it is ∼1–2. This is driven by the effect of cosmic variance on our sample (Appendix B5). Also, the total stellar mass cited here does not include the cDs as their stellar mass is quite uncertain (see Section 2.2).

In contrast to the central parts of Coma, LDEs are typically dominated by spirals. This is quantitatively illustrated by Table 6, which compares the results in Coma with the lower density Virgo cluster and the field. We note that Virgo has significantly lower projected galaxy number densities and halo mass (Binggeli, Tammann & Sandage 1987) than the centre of Coma. McDonald, Courteau & Tully (2009) study a sample of 286 Virgo cluster member galaxies that is complete down to $B_T = 16$ (Vega mag). At stellar mass $M_\star \geq 10^9$ $M_\odot$, if M87 is counted as a giant elliptical, the (E+S0):spirals breakdown is (34.1 per cent+31.6 per cent):34.8 per cent by numbers and (59.2 per cent+19.3 per cent):21.4 per cent by stellar mass. There is evidence (Mihos et al. 2005, 2009; Kormendy et al. 2009) that M87 has a cD halo, and after excluding M87, the (E+S0):spirals breakdown changes slightly to (33.5 per cent+31.6 per cent):34.8 per cent by numbers and (57.2 per cent+20.3 per cent):22.5 per cent by stellar mass. In the field, the (E+S0):spiral morphology breakdown is ∼20 per cent:80 per cent by number for bright galaxies (Dressler 1980).

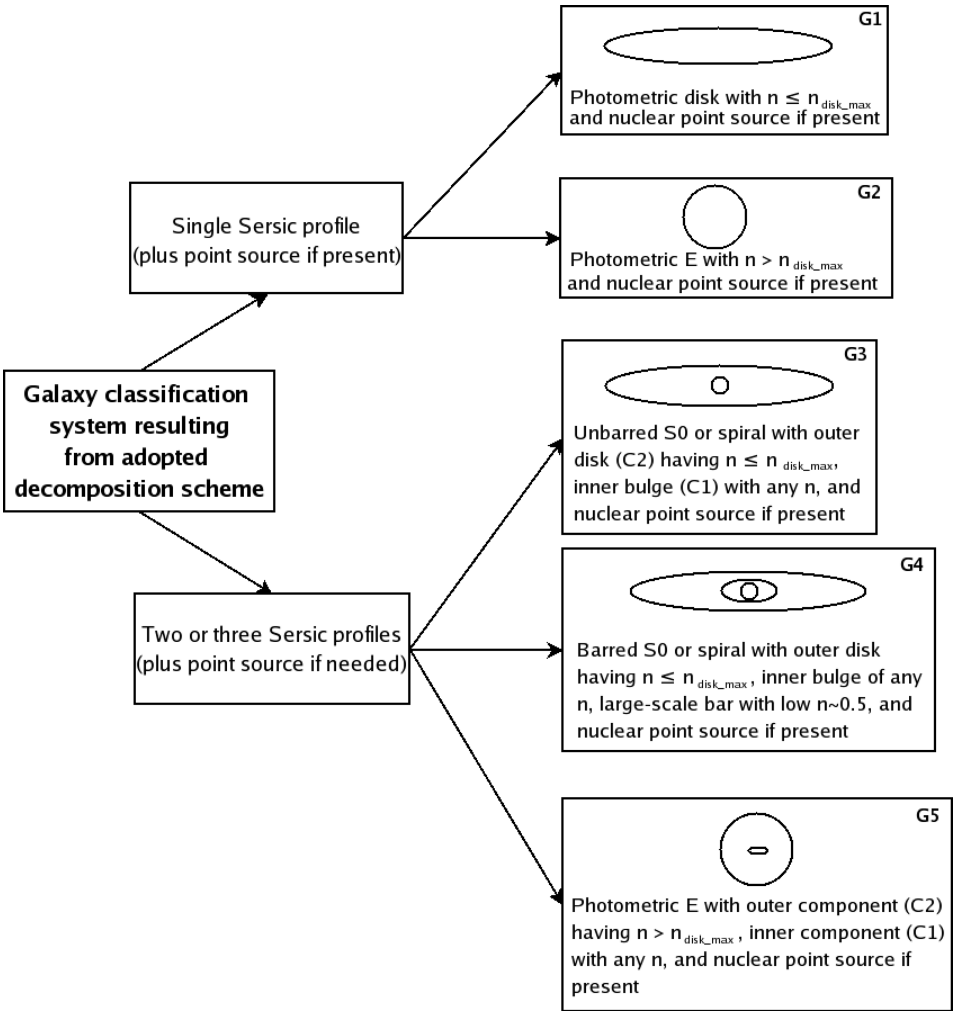

Figure 4. Overview of our galaxy classification system (Section 3.3). Galaxies are deemed to be best represented by a either a single or multicomponent Sérsic profile (plus point source, if needed). Galaxies fitted with a single Sérsic profile are further interpreted as a pure disc (if Sérsic index $n \leq n_{\rm disc\_max}$) or photometric elliptical (if Sérsic index $n > n_{\rm disc\_max}$). When a multicomponent Sérsic profile is required, the galaxy is either an unbarred/barred S0 or spiral, or a photometric E with inner and outer components. S0s and spirals must have an outer component C2 with Sérsic index $n \leq n_{\rm disc\_max}$. The inner component C1 can have any n. If the outer component C2 has Sérsic index $n > n_{\rm disc\_max}$, the galaxy is a photometric elliptical with inner component C1 of any n. The value of $n_{\rm disc\_max}$ is set to 1.66 based on several considerations (See Appendices B2 and D). We determine $n_{\rm disc\_max}$ to be the maximum Sérsic index of the outer disc in spiral and S0 galaxies showing clear signs of an outer disc, such as bars, spiral arms, rings, or high inclination.

4.2 What fraction of total galactic stellar mass is in disc-dominated structures versus classical bulges/ellipticals?

Here and in Section 4.3, we discuss the stellar mass breakdown among galaxy components within each galaxy type. Our results are summarized in Tables 7 and 8.

Recall that in Section 2.2, the total stellar masses were computed through applying calibrations of M/L to the *HST* $F475W$ and $F814W$ photometry. To calculate the stellar mass in galaxy substructures we assume a constant M/L ratio and simply multiply the $F814W$ light ratio of each component by the total galaxy stellar mass. A more rigorous approach is to also perform the decompositions in the $F475W$ band and to fold the colours of galaxy substructures into the calculation. In Appendix B6, we consider the effect of galaxy colour gradients for a subset of galaxies; the effect of the colour gradients on the stellar mass fractions is small (∼5 per cent) and does not impact our conclusions.

Table 7 summarizes our attempt at providing a census of the stellar mass among disc-dominated components and classical bulges/ellipticals, in the projected central 0.5 Mpc of Coma, excluding the two cDs. We highlight the main results below.

(i) *Stellar mass in low-*n *flattened disc-dominated structures (43 per cent).* The total stellar mass in small and large-scale disc-dominated components is ∼36.0 per cent. Bars are disc-dominated components in the sense that they are flattened non-axisymmetric components. Bar proportions typically range from 2.5:1 to 5:1 in their equatorial plane (Binney & Tremaine 1987). The stellar mass percentage in bars is 6.8 per cent. Thus, the total fraction mass in disc-dominated components is 43 per cent.

(ii) *Stellar mass in high-n classical bulges/ellipticals (57 per cent).* The remaining stellar mass is in components with $n > n_{\rm disc\_max}$. These components include the outer components of photometric ellipticals, the central components with $n > n_{\rm disc\_max}$ in photometric ellipticals, and the bulges of S0s and spirals with $n > n_{\rm disc\_max}$. The per cent stellar mass in these systems is 57 per cent.

Table 4. Distribution of best-fitting structural decompositions for stellar mass $M_\star \geq 10^9$ M$_\odot$.

Morphology	Number per bin	Stage 1 w/o Point source	Stage 1 w/o Point source	Stage 2 w/o Point source	Stage 2 w/o Point source	Stage 3 w/o Point source	Stage 3 w/o Point source
(1)	(2)	(3)	(4)	(5)	(6)	(7)	(8)
All Galaxies	69	3	3	14	24	14	11
In terms of galaxy types G1 to G5							
G1: photometric disc	1	0	1	0	0	0	0
G2: photometric E	5	3	2	0	0	0	0
G3: unbarred S0, spiral	24	0	0	8	16	0	0
G4: barred S0, spiral	25	0	0	0	0	14	11
G5: photometric E with extra inner component	14	0	0	6	8	0	0
In terms of Hubble types cD, E, S0, and spiral							
cD	2	2	0	0	0	0	0
Photometric E	17	1	2	6	8	0	0
S0	44	0	1	8	12	14	9
Spiral	6	0	0	0	4	0	2

Notes. This table shows the distribution of best-fitting models and the breakdown of galaxies into classes G1 to G5 arrived at by applying the structural decomposition and galaxy classification schemes described in Section 3.3 and Figs 2–4.

(iii) *Environmental dependence of disc-dominated structures*. Finally, we discuss how $f_{\rm disc\_dominated}$, the fraction of galactic stellar mass in disc-dominated structures, varies with environment. For the lower density field-like environments studied by Weinzirl et al. (2009), this fraction $f_{\rm disc\_dominated}$ is ∼89.6 per cent for galaxies with $M_\star \geq 10^{10}$ M$_\odot$. Applying the same mass cut in Coma, the fraction $f_{\rm disc\_dominated}$ is ∼40.1 per cent, which is lower than in the field as expected.

Due to the effect of cosmic variance on our sample (Appendix B5), our measurement of disc-dominated stellar mass is larger by an estimated factor of 1.27, compared to what would be obtained from an unbiased sample. This is estimated by weighting the fraction of hot and cold stellar mass in elliptical, S0, and spiral galaxies (Table 8) with the morphology–density distribution from GOLD Mine for the projected central 0.5 Mpc of Coma.

We also note here the results for the Virgo cluster, in which Kormendy et al. (2009) find that in galaxies with $M_\star \gtrsim 5 \times 10^9$ M$_\odot$, more than 2/3 of the stellar mass is in classical bulges/ellipticals, implying that $f_{\rm disc\_dominated}$ is less than 1/3. It may seem surprising that our value of $f_{\rm disc\_dominated}$ in Coma is higher than the value of 1/3 for Virgo. However, we believe this apparent discrepancy is due to the fact that the Virgo study includes the giant elliptical galaxy M87, which is marginally classified as a cD (Kormendy et al. 2009), while our study excludes the two cDs in the central part of Coma. If we include these two cDs and adopt a conservative lower limit for their stellar mass, then the fraction $f_{\rm disc\_dominated}$ of stellar mass in the low-n component would be less than 27 per cent, since the cDs add their mass to high-n stellar components (see Appendix B4).

4.3 What fraction of stellar mass within S0, E, spirals is in disc-dominated structures versus classical bulges/ellipticals?

We now discuss how the stellar mass is distributed among E, S0, and spiral Hubble types in the projected central 0.5 Mpc of Coma. As above, fractional stellar masses are reported without including the cD galaxies.

(i) *Mass distribution among high-n classical bulges/ellipticals versus low-n discy pseudo-bulges in Coma S0s and spirals*. Bulges account for ∼30.5 per cent of the stellar mass across E, S0, and spiral galaxies. The ratio R of stellar mass in high-n ($n \gtrsim 1.7$) classical bulges to low-n ($n \lesssim 1.7$) discy pseudo-bulges is 28.3percent/2.2 per cent or 12.9.

(ii) *Mass distributions among bulges in Coma S0s versus S0s in lower density environments*. We next compare the bulges of Coma S0s versus S0s in LDEs. The results are summarized in Table 9. We base this comparison on the results of Laurikainen et al. (2010), who derive structural parameters from 2*D* multicomponent decompositions of 117 S0s in LDEs that include a mix of field and Virgo environments. For S0s in these LDEs with $M_\star \geq 7.5 \times 10^9$ M$_\odot$, the ratio R of stellar mass in high-n ($n \gtrsim 1.7$) classical bulges to low-n ($n \lesssim 1.7$) discy pseudo-bulges is 30.6 per cent/4.7 per cent or 6.5, while it is 41.7 per cent/2.4 per cent or 17.4 in the projected central 0.5 Mpc of Coma. Note that the difference in mass stored in high-n and low-n bulges is not due to a greater frequency of high-n bulges, which is similar at this mass range.

(iii) *Mass distribution in outer and inner components of photometric ellipticals in Coma.* By definition in Section 4.1, photometric ellipticals have no outer disc. The outer components of these ellipticals have Sérsic n from 1.72 to 6.95, with a median value of 2.1. The total fractional stellar mass of the outer structures in ellipticals relative to our sample (minus the cDs) is ∼25.9 per cent. Photometric ellipticals may contain an inner component of any Sérsic n, and we find a range in n of 0.31 to 5.88 in Sérsic index, with a median of 1.0. Inner components with $n \leq n_{\rm disc\_max}$ represent compact inner discs analogous to the discy pseudo-bulges in S0s and spirals; most of these inner components (9/14 or 64.3 ± 12.8 per cent) qualify as inner discs.

4.4 Scaling relations for outer discs and bulges

Here, we explore scaling relations for the bulges and outer discs in the projected central 0.5 Mpc of the Coma cluster. We assess how these structures compare with outer discs and bulges in LDEs, such as field, groups, and even low-density clusters similar to the Virgo cluster, where environmental processes and merger histories are likely to be different.

Table 5. Structural parameters for the best model.

Galaxy name	G*n*	Hubble type	Point source/*T*, C1/*T*, C2/*T*, Bar/*T* (per cent, per cent, per cent, per cent)	C1 r_e (kpc)	C1 *n*	C2 r_e (kpc)	C2 *n*	Bar r_e (kpc)	Bar *n*
(1)	(2)	(3)	(4)	(5)	(6)	(7)	(8)	(9)	(10)
COMAi125926.458p275124.81	G5	E	(0.22, 92.40, 7.36, 0.00)	1.05	1.72	0.42	0.85	–	–
COMAi13007.123p275551.49	G5	E	(0.00, 100.00, 0.00, 0.00)	0.63	1.94	0.32	5.88	–	–
COMAi125930.270p28115.17	G5	E	(0.46, 89.20, 10.30, 0.00)	1.13	1.83	0.62	0.70	–	–
COMAi125937.200p275819.97	G5	E	(0.00, 79.90, 20.10, 0.00)	0.31	6.20	0.20	0.89	–	–
COMAi125953.929p275813.75	G3	spiral	(0.46, 43.00, 56.50, 0.00)	0.79	1.31	1.31	0.63	–	–
COMAi13018.351p28333.32	G3	S0	(0.05, 42.50, 57.40, 0.00)	0.85	1.24	1.75	0.52	–	–
COMAi125937.010p28106.95	G5	E	(0.51, 91.10, 8.42, 0.00)	0.79	2.13	0.35	0.51	–	–
COMAi125946.943p275930.90	G3	S0	(0.09, 7.22, 92.70, 0.00)	0.31	0.98	1.47	1.01	–	–
COMAi13030.954p28630.22	G4	S0	(0.33, 2.13, 75.40, 22.20)	0.14	1.11	1.87	1.20	0.61	0.85
COMAi13035.420p275634.06	G3	S0	(0.06, 28.10, 71.80, 0.00)	0.73	1.05	2.51	0.76	–	–
COMAi125950.183p275445.52	G4	S0	(0.28, 1.85, 86.80, 11.10)	0.19	0.76	1.68	0.91	0.88	0.42
COMAi125959.476p275626.02	G3	S0	(0.38, 42.00, 57.60, 0.00)	1.07	1.67	2.67	0.72	–	–
COMAi13000.949p275643.85	G3	S0	(0.35, 27.70, 72.00, 0.00)	0.47	1.56	2.43	1.15	–	–
COMAi13034.430p275604.95	G3	S0	(0.00, 40.80, 59.20, 0.00)	1.15	1.80	2.83	1.00	–	–
COMAi125931.893p275140.76	G5	E	(0.19, 89.40, 10.40, 0.00)	1.04	2.09	0.62	0.65	–	–
COMAi125931.103p275718.12	G1	S0	(0.11, 0.00, 100.00, 0.00)	–	–	2.38	1.52	–	–
COMAi13041.193p28242.34	G3	spiral	(0.29, 30.60, 69.10, 0.00)	0.41	1.08	1.11	0.84	–	–
COMAi125845.533p274513.75	G5	E	(0.08, 100.00, 0.00, 0.00)	2.98	2.09	1.52	1.71	–	–
COMAi13018.545p28549.62	G3	S0	(0.14, 34.90, 64.90, 0.00)	0.76	0.97	2.83	0.86	–	–
COMAi13021.673p275354.81	G3	S0	(0.74, 30.40, 68.90, 0.00)	0.40	1.14	1.71	0.56	–	–
COMAi13024.823p275535.94	G3	spiral	(0.23, 14.20, 85.50, 0.00)	0.58	1.36	3.06	1.20	–	–
COMAi13051.149p28249.90	G3	S0	(0.05, 16.30, 83.60, 0.00)	0.96	1.57	5.98	1.35	–	–
COMAi13011.143p28354.91	G3	S0	(0.13, 19.20, 80.70, 0.00)	0.66	2.64	1.48	1.40	–	–
COMAi125937.990p28003.52	G4	spiral	(0.76, 22.60, 67.50, 9.09)	0.37	2.38	1.40	0.50	0.67	0.33
COMAi13018.873p28033.38	G4	S0	(0.00, 54.20, 34.70, 11.10)	0.18	2.95	0.86	1.04	0.51	0.56
COMAi125911.543p28033.32	G3	S0	(0.19, 23.90, 75.90, 0.00)	0.54	0.95	1.55	1.21	–	–
COMAi125904.797p28301.16	G4	S0	(0.09, 4.23, 76.80, 18.90)	0.21	1.22	2.72	1.12	0.83	0.85
COMAi125909.468p28227.35	G2	E	(0.00, 100.00, 0.00, 0.00)	1.88	2.54	–	–	–	–
COMAi125935.286p275149.13	G5	E	(0.05, 85.80, 14.10, 0.00)	1.37	2.08	0.70	0.31	–	–
COMAi13005.405p28128.14	G4	S0	(0.00, 14.20, 72.20, 13.60)	0.35	1.18	3.60	0.92	1.29	0.45
COMAi125950.105p275529.44	G4	S0	(0.00, 26.70, 66.00, 7.31)	0.80	2.37	1.99	1.66	0.51	0.28
COMAi13018.772p275613.34	G4	S0	(0.00, 9.13, 69.10, 21.80)	0.49	0.98	2.87	0.69	1.64	0.60
COMAi125938.321p275913.89	G3	spiral	(0.08, 25.30, 74.60, 0.00)	0.71	2.06	3.27	0.89	–	–
COMAi125940.270p275805.71	G4	S0	(0.00, 33.40, 65.70, 0.94)	0.31	3.39	1.82	0.86	0.48	0.14
COMAi125944.208p275730.38	G5	E	(0.00, 85.30, 14.70, 0.00)	5.43	5.82	1.95	0.56	–	–
COMAi125939.659p275714.03	G3	S0	(0.64, 33.70, 65.70, 0.00)	0.32	1.91	1.97	1.08	–	–
COMAi13044.632p28602.31	G3	S0	(0.00, 26.80, 73.20, 0.00)	0.35	1.51	2.36	0.80	–	–
COMAi125928.721p28225.92	G4	S0	(0.00, 25.30, 33.70, 41.00)	0.40	1.65	3.28	0.57	1.54	1.05
COMAi125942.301p275529.15	G3	S0	(0.00, 25.20, 74.80, 0.00)	0.08	1.53	0.98	1.48	–	–
COMAi13017.014p28350.07	G4	S0	(0.00, 47.20, 31.60, 21.20)	0.70	4.67	3.57	0.58	0.80	0.64
COMAi125956.697p275548.71	G4	S0	(0.18, 49.60, 26.20, 24.00)	1.89	4.33	3.57	0.25	2.48	0.41
COMAi13016.534p275803.15	G3	S0	(0.00, 84.10, 15.90, 0.00)	3.26	6.16	3.59	0.48	–	–
COMAi13006.395p28015.94	G3	S0	(0.00, 66.10, 33.90, 0.00)	1.60	6.78	2.08	0.84	–	–
COMAi13027.966p275721.56	G4	S0	(0.00, 42.80, 41.30, 15.90)	0.42	2.67	3.32	0.32	1.01	0.98
COMAi13012.868p28431.74	G4	S0	(0.00, 67.10, 19.10, 13.80)	0.77	2.42	5.07	0.41	3.00	0.53
COMAi125943.721p275940.82	G3	S0	(0.00, 69.20, 30.80, 0.00)	0.76	3.20	1.83	0.72	–	–
COMAi13028.370p275820.64	G4	S0	(0.05, 33.80, 31.40, 34.80)	0.85	2.53	5.02	0.38	3.61	0.59
COMAi13042.832p275746.95	G4	S0	(0.00, 43.90, 46.40, 9.68)	0.75	3.01	3.81	0.47	1.51	0.39
COMAi13038.761p28052.34	G4	S0	(0.13, 16.80, 71.90, 11.10)	0.46	1.68	3.81	0.85	2.86	0.61
COMAi13014.746p28228.69	G3	S0	(0.43, 78.20, 21.40, 0.00)	0.90	3.68	2.26	0.47	–	–
COMAi13022.170p28249.30	G4	S0	(0.00, 15.20, 73.40, 11.50)	0.31	1.35	3.49	1.24	1.31	0.48
COMAi125931.453p28247.60	G3	S0	(0.00, 78.60, 21.40, 0.00)	1.61	3.51	2.36	0.86	–	–
COMAi13018.093p275723.59	G2	E	(0.17, 100.00, 0.00, 0.00)	1.27	2.37	–	–	–	–
COMAi13040.838p275947.80	G5	E	(0.13, 99.91, 0.00, 0.00)	3.16	2.34	0.34	1.83	–	–
COMAi125852.097p274706.15	G5	E	(0.00, 50.00, 50.00, 0.00)	2.12	6.95	1.74	1.41	–	–
COMAi125946.782p275825.99	G4	S0	(0.00, 15.70, 67.70, 16.60)	0.31	1.75	3.44	0.67	1.23	0.72
COMAi13008.003p28442.81	G3	S0	(0.00, 85.00, 15.00, 0.00)	0.99	3.00	1.66	0.57	–	–
COMAi125929.956p275723.26	G4	S0	(0.37, 24.20, 25.50, 49.90)	0.45	1.75	5.59	0.33	3.15	1.02
COMAi125929.403p275100.46	G5	E	(0.00, 100.00, 0.00, 0.00)	2.37	1.86	0.28	2.19	–	–
COMAi125932.771p275901.04	G4	S0	(0.02, 49.00, 46.70, 4.25)	2.21	6.05	3.01	0.83	0.50	0.54
COMAi125944.407p275444.84	G4	S0	(0.00, 34.30, 62.10, 3.65)	0.75	2.59	2.92	1.09	1.38	0.23
COMAi125930.824p275303.05	G4	spiral	(0.36, 41.90, 41.20, 16.50)	0.54	1.89	6.41	0.66	1.79	0.46

Table 5 – *continued*

Galaxy name	G*n*	Hubble type	Point source/*T*, C1/*T*, C2/*T*, Bar/*T* (per cent, per cent, per cent, per cent)	C1 r_e (kpc)	C1 *n*	C2 r_e (kpc)	C2 *n*	Bar r_e (kpc)	Bar *n*
(1)	(2)	(3)	(4)	(5)	(6)	(7)	(8)	(9)	(10)
COMAi13039.767p275526.19	G4	S0	(0.01, 46.30, 53.40, 0.34)	1.28	3.05	3.59	1.42	0.89	0.28
COMAi13042.766p275817.38	G4	S0	(0.00, 66.90, 31.30, 1.80)	1.27	2.99	6.23	0.35	1.42	0.17
COMAi13048.646p28526.69	G5	E	(0.11, 70.20, 29.70, 0.00)	3.12	5.17	1.87	1.10	–	–
COMAi13017.683p275718.93	G2	E	(0.21, 100.00, 0.00, 0.00)	2.13	2.80	–	–	–	–
COMAi13051.464p28234.86	g5	E	(0.00, 100.00, 0.00, 0.00)	3.90	2.01	0.61	2.21	–	–
NGC 4889	G2	cD	(0.00, 100.00, 0.00, 0.00)	57.7	7.8	–	–	–	–
COMAi125935.698p275733.36 (NGC 4874)	G2	cD	(0.00, 100.00, 0.00, 0.00)	391.3	11.4	–	–	–	–

Notes. Rows are sorted by increasing $M_\star$. In columns 4–8, the meaning of C1 and C2 depends on Hubble type. For cD and elliptical (E) galaxies, C1 is the outermost structure. For E galaxies, C2 represents the inner component of any *n*. For S0 and spiral galaxies, C1 is the bulge and C2 is the outer disc. The bar component represents bars/ovals in S0 and spiral galaxies. For cored galaxies (NGC 4874, NGC 4889, COMAi125909.468p28227.35), the reported model corresponds to the 2D fit where the cored region of the galaxy has been masked (see Table 2 and Appendix C).

Table 6. Morphology–density relation.

Region (1)	Mass or mag cut (2)	Galaxy type[a,b] (3)	Per cent by numbers (4)	Per cent by stellar mass (5)
Central 0.5 Mpc of Coma (This work)	$M_\star \geq 10^9$ M$_\odot$	(E+S0):spiral	(25.3 + 65.7):9.0	(32.0 + 62.2):5.8
Virgo (McDonald et al. 2009)	$M_\star \geq 10^9$ M$_\odot$	(E+S0):spiral	(33.8 + 31.3):35.0	(57.2 + 20.3):22.5
Virgo (McDonald et al. 2009)	$M_B \leq -19$	(E+S0):spiral	(28.2 + 36.9):35.0	(57.3 + 20.2):22.5
Field (Dressler 1980)	Bright galaxies	(E+S0):spiral	(∼20):∼80	-

Notes. [a]Coma has two cD galaxies in the central 0.5 Mpc.
[b]M87 in Virgo is considered an elliptical galaxy by McDonald et al. (2009). The detection of intracluster light around M87 (Mihos et al. 2005, 2009) is definitive proof that it is a cD galaxy (see also the discussion in Kormendy et al. 2009). Here, we consider M87 a cD galaxy and do not include it in the above statistics for ellipticals.

Table 7. Total galactic stellar mass in disc-dominated structures versus classical bulges/ellipticals.

Structure (1)	Per cent of stellar mass in the projected central 0.5 Mpc of Coma (2)
Disc-dominated components with $n \leq n_{\rm disc\_max}$	
Outer discs of S0s	27.7
Outer discs of spirals	2.94
Bulges with $n \leq n_{\rm disc\_max}$ (pseudo- or discy bulge) in S0s	2.07
Bulges with $n \leq n_{\rm disc\_max}$ (pseudo- or discy bulge) in spirals	0.13
Inner component with $n \leq n_{\rm disc\_max}$ (inner discs) in photometric E	3.26
Total	**36.1**
Bars	
Bars in S0s	6.11
Bars in spirals	0.73
Total	**6.84**
Non-disc 'hot' components with $n > n_{\rm disc\_max}$	
Outer component with $n > n_{\rm disc\_max}$ in photometric E	26.0
Inner component with $n > n_{\rm disc\_max}$ in photometric E	2.74
Inner component with $n > n_{\rm disc\_max}$ in S0s	26.2
Inner component with $n > n_{\rm disc\_max}$ in spirals	2.06
Total	**57.0**

Notes. These numbers apply to the galaxies in the projected central 0.5 Mpc of Coma, after excluding the two cDs. We exclude the two cDs due to their uncertain stellar mass and the reasons outlined at the end of Section 2.2.

For this comparison, we use the results of Gadotti (2009), who studies face-on ($b/a \geq 0.9$) galaxies from the SDSS Data Release 2 in a volume limited sample at $0.02 \leq z \leq 0.07$. He derives galaxy structure from 2D decompositions of multiband *gri* images that account for bulge, disc, and bar components. The Coma sample S0s/spirals have stellar mass $10^9 \leq M_\star \leq 6 \times 10^{10}$ M$_\odot$, and for this comparison we consider only galaxies with stellar mass $5 \times 10^9 \leq M_\star \leq 6 \times 10^{10}$ M$_\odot$. We proceed with the caveat that the sample from Gadotti (2009) is incomplete in mass for $M_\star \lesssim 5 \times 10^{10}$ M$_\odot$.

Table 8. Fraction of stellar mass in disc-dominated structures versus classical bulges/ellipticals in different galaxies.

Structure (1)	Per cent of stellar mass within each galaxy type (2)	Per cent of stellar mass in the projected central 0.5 Mpc of Coma (3)
Photometric E (N = 17)		
Outer component with $n > n_{\rm disc\_max}$	81.2	26.0
Inner component with $n > n_{\rm disc\_max}$	8.6	2.74
Inner component with $n \leq n_{\rm disc\_max}$	10.2	3.26
Point sources	0.09	0.03
Total	**100**	**32.0**
S0 (N = 44)		
Outer disc with $n \leq n_{\rm disc\_max}$	44.4	27.7
Bars	9.8	6.11
Bulges with $n > n_{\rm disc\_max}$ (classical bulge)	42.2	26.2
Bulge components with $n \leq n_{\rm disc\_max}$ (discy pseudo-bulge)	3.3	2.07
Point sources	0.06	0.04
Total	**100**	**62.1**
Spiral (N = 6)		
Outer disc with $n \leq n_{\rm disc\_max}$	50.0	2.94
Bars	12.4	0.73
Bulges with $n > n_{\rm disc\_max}$ (classical bulge)	35.0	2.06
Bulge components with $n \leq n_{\rm disc\_max}$ (discy pseudo-bulge)	2.2	0.13
Point sources	0.3	0.02
Total	**100**	**5.90**

Notes. The totals listed in column 3 correspond to column 5 of Table 6. These numbers apply to the galaxies in the projected central 0.5 Mpc of Coma, after excluding the two cDs. We exclude the two cDs due to their uncertain stellar mass and the reasons outlined at the end of Section 2.2.

Table 9. Bulge Sérsic index in S0s across different environments.

Bulge Sérsic index of S0s (1)	Environment (2)	Stellar mass cut (3)	Per cent of S0s (4)	Per cent of bulge stellar mass in S0s (5)
		This work		
$n \leq n_{\rm disc\_max}$	Projected Central 0.5 Mpc of Coma, high density	$M_\star \geq 10^9$ M$_\odot$	38.6 ± 7.3	3.06
$n > n_{\rm disc\_max}$	Projected Central 0.5 Mpc of Coma, high density	$M_\star \geq 10^9$ M$_\odot$	59.1 ± 7.4	42.2
		This work		
$n \leq n_{\rm disc\_max}$	Projected Central 0.5 Mpc of Coma, high density	$M_\star \geq 7.5 \times 10^9$ M$_\odot$	21.4 ± 7.8	2.4
$n > n_{\rm disc\_max}$	Projected Central 0.5 Mpc of Coma, high density	$M_\star \geq 7.5 \times 10^9$ M$_\odot$	78.6 ± 7.8	41.7
		Laurikainen et al. (2010)		
$n \leq n_{\rm disc\_max}$	Lower density	$M_\star \geq 7.5 \times 10^9$ M$_\odot$	22.3 ± 3.9	4.7
$n > n_{\rm disc\_max}$	Lower density	$M_\star \geq 7.5 \times 10^9$ M$_\odot$	77.7 ± 3.9	30.6

Notes. This table shows the fraction of S0 galaxies with bulge Sérsic index above and below the value $n_{\rm disc\_max} = 1.66$ determined empirically in Appendix B2. The first four rows pertain to the Coma cluster and represent different stellar mass cuts. The bottom two rows are for S0 galaxies studied by Laurikainen et al. (2010) from much LDEs than the rich Coma cluster. Column 5 represents the per cent of total bulge stellar mass to total galaxy stellar mass calculated over S0s satisfying each specific bulge index and stellar mass cut.

Fig. 5 compares properties of large-scale discs (size, luminosity) with galaxy $M_\star$. Fig. 5(a) explores the *projected* half-light radius in the *i* band ($r_{\rm e}$) of outer discs along the major axis at a given galaxy $M_\star$ in Coma versus LDEs. It shows that at a given galaxy $M_\star$, the average disc $r_{\rm e}$ is smaller in the projected central 0.5 Mpc of Coma compared with LDEs by ∼30–82 per cent. While the scatter in disc $r_{\rm e}$ is large, the separation between the two mean values in each mass bin is larger than the sum of the errors. The suggestion that outer discs in Coma are more compact is consistent with the results of previous analyses of disc structure in Coma (Aguerri et al. 2004; Gutiérrez et al. 2004). Fig. 5(b) makes a similar comparison for the outer disc luminosity between Coma and LDEs. We use here the ACS *F*814*W* photometry for Coma and the SDSS *i*-band photometry from Gadotti (2009). At a given stellar mass, the average outer disc luminosities are fainter by ∼40–70 per cent, excluding the lowest mass bin.

We next consider the effect of M/L to test if the difference in outer disc luminosity could imply a difference in outer disc mass. For Coma, we show the *galaxy-wide* $(M/L)_i$ ratio estimated, while for the Gadotti (2009) sample we show *i*-band M/L ratios in the outer discs, $(M/L)_{d,\,i}$. Fig. 5(c) compares the resulting (M/L) values against galaxy $M_\star$. The average $(M/L)_i$ in Coma is larger than the average $(M/L)_{d,\,i}$ in LDEs by a factor of ∼1.3−2 at a given galaxy $M_\star$, excluding the lowest mass bin. This difference in $(M/L)_i$ accounts for ∼48–80 per cent of the average offset in disc luminosity. This suggests that *some* of the difference in outer disc luminosity might be driven by a real difference in outer disc mass. Cappellari (2013), in comparison, concludes that spirals in Coma transformed

$$5 \times 10^9 \leq M_\star \leq 6 \times 10^{10} M_\odot$$

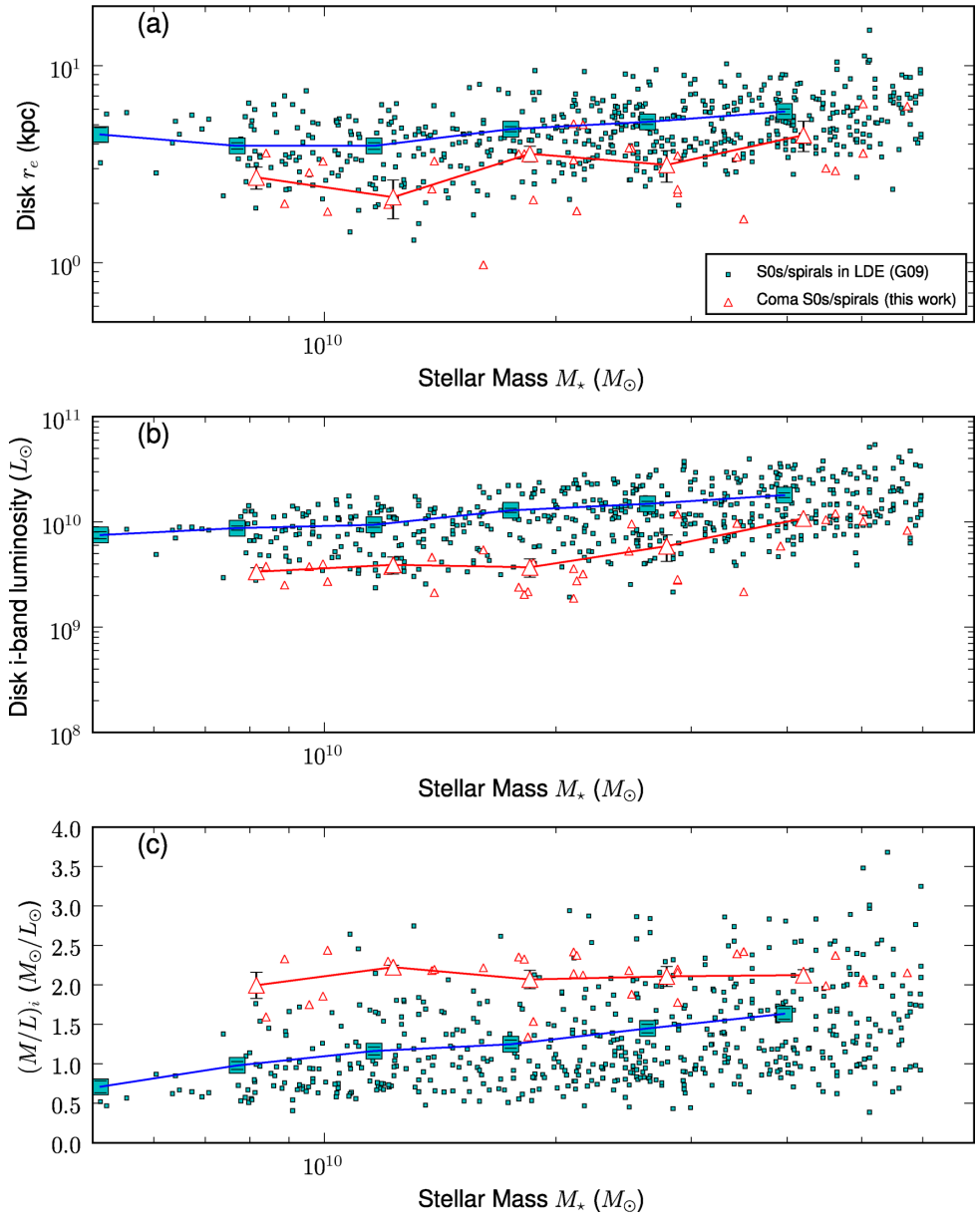

Figure 5. Panels (a) and (b) compare the properties of large-scale discs (r_e, luminosity) with galaxy stellar mass $M_\star$. Massive ($5 \times 10^9 \leq M_\star \leq 6 \times 10^{10}$ $M_\odot$) S0/spiral galaxies from the projected central 0.5 Mpc of Coma as well as low-density environments (LDEs) are considered. The LDE sample is from Gadotti (2009) and includes galaxies in SDSS Data Release 2 that are face-on ($b/a \geq 0.9$) and have redshift $0.02 \leq z \leq 0.07$. In panel (b), the *i*-band luminosity represents the ACS *F*814*W* photometry for Coma galaxies and the SDSS *i*-band photometry for the LDE galaxies. Panel (c) compares *i*-band mass-to-light ratio $(M/L)_i$ with galaxy $M_\star$. For Coma, the galaxy wide mass-to-light ratio is plotted, while for LDEs the *outer disc* $(M/L)_i$ is shown. In all panels, the mean values (large symbols) in galaxy $M_\star$ for Coma and LDEs are slightly offset along the *x*-axis, as shown by the red triangle and blue squares, in order to avoid the error bars from overlapping. The mean values are calculated in 0.18 dex bins. The error bars on the mean values represent the standard error on the mean. This figure demonstrates that at a given galaxy stellar mass, the average disc half-light radius r_e in the *i* band is smaller in the projected central 0.5 Mpc of Coma compared to LDEs.

into fast rotating early-type galaxies while decreasing in *global* half-light radius with little mass variation.

Fig. 6 examines how bulge size (r_e), bulge luminosity, bulge Sérsic index, and bulge-to-disc *light ratio* (B/D) scale with galaxy $M_\star$. Figs 6(a)–(c) show that bulge size, bulge luminosity, and bulge Sérsic index as a function of galaxy $M_\star$ are not systematically offset in Coma versus LDEs. Fig. 6(d) shows there is a great scatter in B/D versus galaxy $M_\star$.

Fig. 7(a) shows B/D versus bulge Sérsic index. At a given bulge Sérsic index, galaxies in Coma show a systematically higher average

$$5 \times 10^9 \leq M_\star \leq 6 \times 10^{10} M_\odot$$

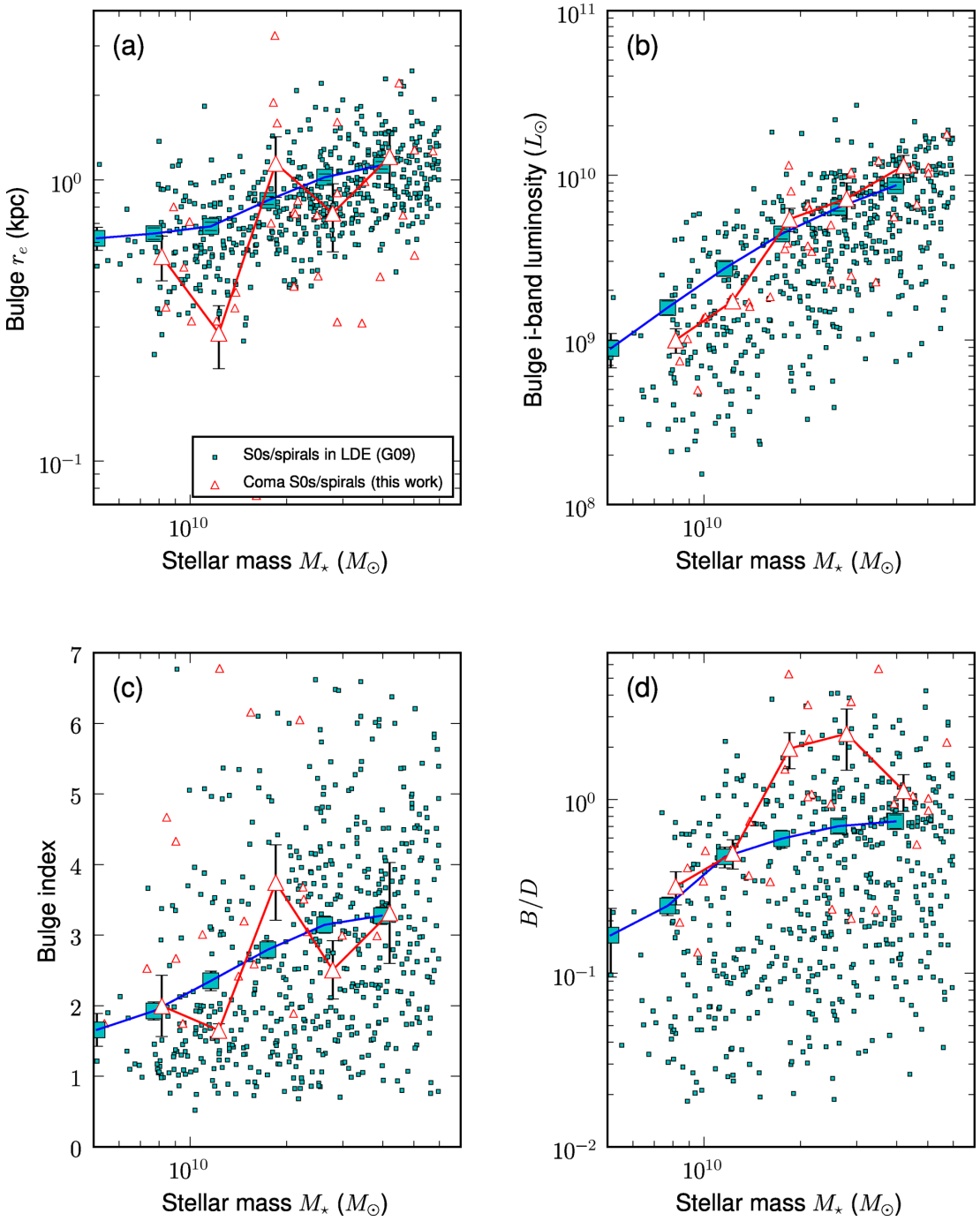

Figure 6. Is similar to Fig. 5, except that it emphasizes S0/spiral galaxy bulges. See Section 4.4 and Fig. 5 for extra details on the sample from Gadotti (2009). Panels (a), (b), (c), and (d) show bulge size (r_e), bulge *i*-band luminosity, bulge Sérsic index, and bulge-to-disc *light ratio* (B/D), respectively, versus galaxy $M_\star$. In all panels, the error bars on the mean values (large symbols) represent the standard error on the mean, and in all panels the mean values in galaxy $M_\star$ for Coma and LDEs are slightly offset along the *x*-axis, as shown by the red triangle and blue squares, in order to avoid the error bars from overlapping. This figure demonstrates that at a given galaxy stellar mass, there appears to be no systematic offset between bulges in Coma and LDEs.

B/D ratio than galaxies in LDEs. A linear regression fit reveals a clear offset in B/D for a given bulge index. Fig. 7(b) indicates that at a given bulge Sérsic index the bulge luminosities in Coma and LDEs are very consistent. Fig. 7(c), on the other hand, shows a clear offset in disc luminosity (∼0.6 mag), indicating that differences in B/D are due, at least in part, to outer disc size/luminosity.

From this investigation, we have learned of a reduction in the average sizes and luminosities in the outer discs of Coma galaxies that

$$5 \times 10^9 \leq M_\star \leq 6 \times 10^{10} M_\odot$$

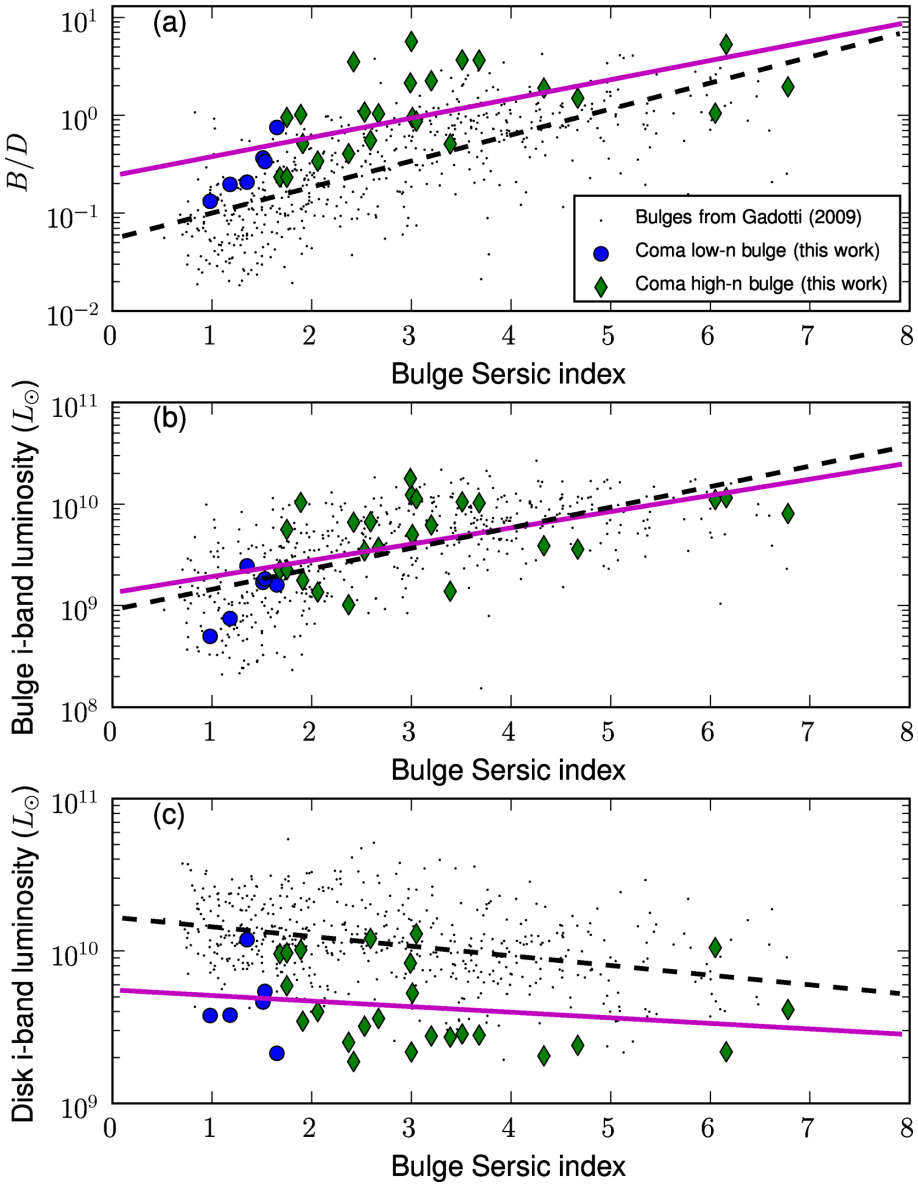

Figure 7. Shows a comparison of bulges in massive ($5 \times 10^9 \leq M_\star \leq 6 \times 10^{10}$ M$_\odot$) S0/spiral galaxies in LDEs from Gadotti (2009) versus galaxies in the projected central 0.5 Mpc of Coma. See Section 4.4 and Fig. 5 for extra details on the sample from Gadotti (2009). Bulges in Coma are divided into groups of low Sérsic index ($n \leq n_{\rm disc\_max}$) and high Sérsic index ($n > n_{\rm disc\_max}$). Panel (a) shows bulge-to-disc *light ratio* (B/D) versus bulge Sérsic index. Panels (b) and (c) show bulge and disc *i*-band luminosity, respectively, versus bulge Sérsic index. In each panel, the *solid line* represents the fit to Coma bulges of all Sérsic n, and the *dashed line* is the corresponding fit to bulges of all Sérsic n from LDEs. The offset in B/D in panel (a) appears to be driven, at least in part, by the offset in disc luminosity in panel (c).

may translate into a lower mean outer disc stellar mass. This may be explained in part by cluster environmental effects. We consider this point further in Section 4.5.

4.5 Environmental processes in Coma

Many studies provide evidence for the action of environmental processes in Coma. The predominantly intermediate or old stellar populations in the centre of the cluster (e.g. Poggianti et al. 2001; Trager, Faber & Dressler 2008; Edwards & Fadda 2011) are indirect evidence for the action of starvation. Furthermore, the properties of Coma S0s display radial cluster trends that favour formation processes that are environment mediated (Rawle et al. 2013, Head et al. 2014). Several examples of ram-pressure stripping have been directly observed in Coma (Yagi et al. 2007, 2010; Yoshida et al. 2008; Smith et al. 2010; Fossati et al. 2012). There is also much evidence for the violent effects of tidal forces. The presence of a diffuse intracluster medium around Coma central galaxies NGC 4874 and NGC 4889 has long been discussed (Kormendy & Bahcall 1974; Melnick, Hoessel & White 1977; Thuan & Kormendy 1977; Bernstein et al. 1995; Adami et al. 2005; Arnaboldi 2011). At the cluster centre, the intracluster light represents up to 20 per cent

of the cluster galaxy luminosity (Adami et al. 2005). This central intracluster light is not uniform given the presence of plumes and tidal tails (Gregg & West 1998; Adami et al. 2005), and debris fields are also found further outside the cluster centre (Gregg & West 1998; Trentham & Mobasher 1998).

Below, we comment on how our results add to this picture.

(i) *Reduced growth and truncations of outer disc in Coma S0s/spirals*. In Section 4.4, we found that at a given galaxy stellar mass, the average half-light radius (r_e) of the outer disc in S0s/spirals is ∼30–82 per cent smaller, and the average disc *i*-band luminosity is ∼40–70 per cent fainter in Coma than in LDEs (Fig. 5). These observations may be explained in part by cluster environmental effects (e.g., strangulation, ram-pressure stripping, tidal stripping) that suppress the growth of large-scale discs. Hot gas stripping (strangulation) can plausibly suppress disc growth by limiting the amount of gas that can cool and become part of the outer disc. Tidal stripping via galaxy harassment is predicted (e.g. Moore et al. 1999) to be particularly efficient at removing mass from extended discs. Ram-pressure stripping is most effective at removing H I gas in the outskirts of a large-scale disc. The evidence (Yagi et al. 2007, 2010; Yoshida et al. 2008; Fossati et al. 2012) suggests that ram-pressure stripping happens quickly, and if so it should be effective at preventing the growth of large-scale discs after the host galaxy enters the cluster.

(ii) *Low Sérsic index in S0/spiral outer discs*. Fig. 8 demonstrates that the majority of outer discs have low Sérsic index (66.0 ± 8.2 per cent with $n < 1$ and 18.0 ± 12.8 per cent with $n < 0.5$). This effect is not artificially driven by bars because the low $n < 1$ discs include barred and unbarred galaxies to similar proportions, and additionally, the discs are fitted separately from the bars in our work. Similar examples have been found in Virgo. Kormendy & Bender (2012) find several examples of Gaussian ($n \sim 0.5$) discs among both barred and unbarred galaxies, which commonly occur in barred galaxies (e.g. Kormendy & Kennicutt 2004). Gaussian-like discs among unbarred galaxies are much more surprising (Kormendy & Bender 2012). Fig. 8 shows that the large fraction of $n < 1$ outer discs in Coma is not driven by barred galaxies alone. It is not easy to compare the fraction of low $n < 1$ discs in Coma versus LDEs because most work to date in LDEs (e.g. Allen et al. 2006; Laurikainen et al. 2007, 2010; Weinzirl et al. 2009) fit the outer disc with a fixed $n = 1$ exponential profile.

Environmental processes could be creating the Gaussian-like discs. Kormendy & Bender (2012) have suggested this and invoked dynamical heating. We could be seeing a stronger and/or different manifestation in Coma. Ram-pressure stripping and tidal stripping can plausibly reduce the Sérsic *n* by cutting off the outskirts of the outer stellar/gaseous disc.

(iii) *Bulge-to-disc ratio (*B/D*)*. The mean bulge Sérsic index rises with mean B/D light ratio in both the central part of Coma and LDEs, consistent with the idea that the development of high B/D ratio in galaxies is usually associated with processes, such as major mergers, which naturally results in a high *n*. Such a correlation was also found previously in field spirals (e.g. Andredakis, Peletier & Balcells 1995; Weinzirl et al. 2009).

We also find that at a given bulge index, the B/D light ratio is higher for Coma. This environmental effect appears to be due, at least in part, to the fact that at a given bulge *n*, the bulge luminosity is similar in Coma and LDEs, but the outer discs have lower luminosity by a factor of a few in Coma (Fig. 7). This reduced disc growth is likely due to cluster environmental effects suppressing the growth of large-scale outer discs. This conclusion for Coma nicely parallel studies of ram-pressure stripping (Cayatte et al. 1990, 1994; Kenney, van Gorkom & Vollmer 2004; Chung et al. 2007, 2009; Kenney et al. 2008) and dynamical heating (Kormendy & Bender 2012) in the less extreme Virgo cluster.

5 COMPARISON OF EMPIRICAL RESULTS WITH THEORETICAL PREDICTIONS

5.1 Overview of the models

In this section, we compare our empirical results for Coma with simulations of clusters. The simulated clusters are derived from a semi-analytical model (SAM) based on Neistein & Weinmann (2010). The SAM is able to produce reasonable matches (Wang, Weinmann & Neistein 2012) to the galaxy stellar mass function determined by Li & White (2009) for massive $M_\star \gtrsim 5 \times 10^8$ M$_\odot$ galaxies at low redshift ($0.001 < z < 0.5$) over all environments (including Virgo and Coma) probed in the Northern hemisphere component of SDSS Data Release 7 (DR7). A brief summary of the SAM formalism is given below. Interested readers should see Neistein & Weinmann (2010) and Wang et al. (2012) for additional details.

The SAM uses merger trees extracted from the Millennium *N*-body simulation (Springel et al. 2005). Galaxies are modelled as vectors of stellar mass, cold gas, and hot gas. Baryonic physics are handled with semi-analytic prescriptions. In between merger events, the efficiencies of quiescent evolutionary processes, such as cold and hot gas accretion, gas cooling, SF, and supernovae feedback, are modelled as functions of halo mass and redshift only. The star formation rate (SFR) is proportional to the amount of cold gas, and the SF efficiency is a function of halo mass and redshift. In the model, the baryonic mass (i.e. the sum of stellar and cold gas mass) is used to define major ($M_1/M_2 \geq 1/4$) and minor ($1/10 < M_1/M_2 < 1/4$) mergers. As we will discuss in Section 5.4, the results are highly sensitive to whether the stellar mass ratio or baryonic mass ratio are used.

Immediately after a major merger, the remnant's stellar B/T ratio is always one. This is because the model assumes any existing stellar discs are destroyed, and all stars undergo violent relaxation to form a bulge/elliptical. After a major merger, an extended stellar disc is rebuilt via gas cooling, causing B/T to fall. Any further major mergers will reset B/T to 1. During a minor merger, the stellar component of the satellite of baryonic mass M_1 is added to the bulge.

During a major/minor merger, some fraction of cold gas is converted to stars in a short induced starburst ∼10 Myr in duration. The amount of merger-induced SF depends explicitly on the cold gas mass. Stars formed in *major* merger-induced starbursts are considered part of the bulge (see Section 5.6). This is a reasonable assumption given that (a) the bursts of SF are much shorter than the overall duration of the mergers and (b) all existing stars *from both progenitors* are violently relaxed during final coalescence. It seems less likely that the starburst stars induced in minor mergers should be violently relaxed since minor mergers are not very efficient at violently relaxing stars in the host galaxy. We consider this issue further in Section 5.6. Therefore, in the model used in this paper, the bulge stellar mass traces the mass assembled via major and minor mergers. Galaxies without bulges have had no resolvable merger history. The model does not build bulges through the coalescence of clumps condensing in violent disc instabilities (Bournaud et al. 2007a; Elmegreen et al. 2009).

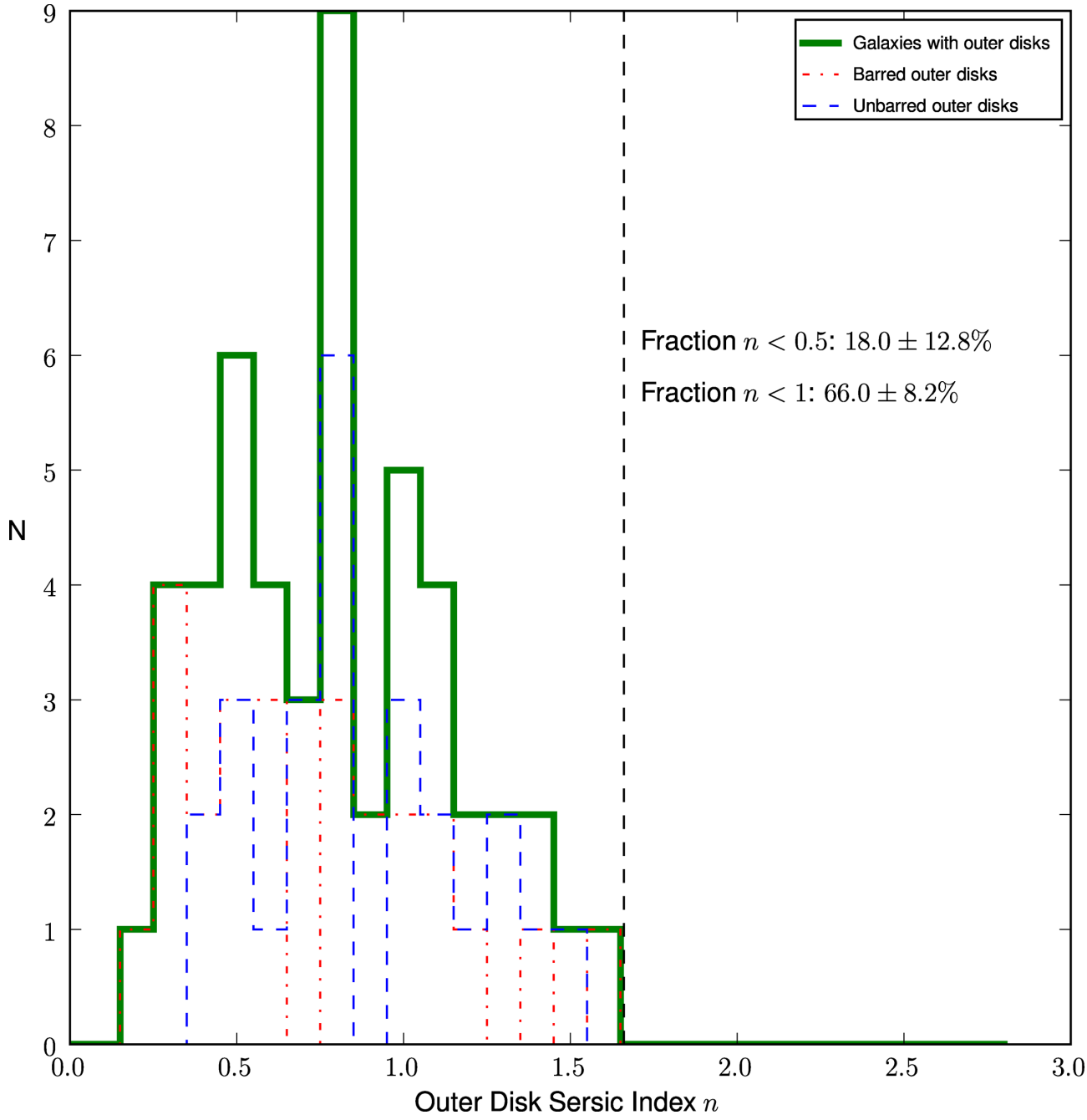

Figure 8. The distribution of Sérsic index for outer discs in S0/spiral galaxies. The vertical line represents the empirically determined upper limit, $n_{\rm disc\_max}$, in the Sérsic index of outer barred discs, which can be considered unambiguous cases of outer discs due to the presence of a bar. The dash–dotted and dashed lines show the distributions for barred and unbarred outer discs, respectively. See Section 3.3 and Appendix B2 for details.

Galaxy clusters impose additional environmental effects that complicate modelling with SAMs. The SAM used here accounts for stripping of hot gas (i.e. strangulation; Larson et al. 1980) by assuming that hot gas is stripped exponentially with a time-scale of 4 Gyr. Other processes like ram-pressure stripping/disruption of stellar mass (Moore et al. 1996, 1998, 1999; Gnedin 2003), dynamical friction heating by satellite (El-Zant, Kim & Kamionkowski 2004), and gravitational heating by infalling substructures (Khochfar & Ostriker 2008) are neglected. It is not clear how much the inclusion of ram-pressure stripping in the SAM would affect our results. While hydrodynamical simulations clearly demonstrate the strong influence of ram-pressure stripping on gas mass, galaxy morphology, and SF (e.g. Quilis, Moore & Bower 2000; Tonnesen & Bryan 2008, 2009, 2010), some SAMs (e.g. Okamoto & Nagashima 2003; Lanzoni et al. 2005) suggest that accounting for ram-pressure stripping has only a small affect. Tidal stripping creates a population of intracluster stars that can contribute between 10 and 40 per cent of the optical light in rich clusters (e.g. Bernstein et al. 1995; Feldmeier et al. 2004; Zibetti et al. 2005). The inclusion of tidal stripping in SAMs is important for addressing a wide range of systematic effects (e.g. Bullock, Kravtsov & Weinberg 2001; Weinmann et al. 2006; Henriques, Bertone & Thomas 2008; Henriques & Thomas 2010), but tidal stripping is not present in this SAM.

5.2 The mass function and cumulative number density in Coma

In order to compare galaxies in the simulations with those in the centre of Coma, we first need to identify model clusters that best represent Coma. We do this based on the global properties of Coma, namely the halo mass and size, galaxy stellar mass function, and radial profile of cumulative projected galaxy number density. As the ACS coverage of Coma encompasses a fraction (19.7 per cent) of the projected central 0.5 Mpc, we calculate these properties in Coma with DR7 of the NYU Value-Added Galaxy Catalog (NYU-VAGC; Blanton et al. 2005), which provides full spatial coverage of Coma. NYU-VAGC DR7 is based on SDSS DR7 data (Abazajian et al. 2009) and provides catalogues generated from an independent, and improved, reduction of the public data (Padmanabhan et al. 2008).

We select Coma cluster member galaxies from NYU-VAGC assuming that Coma cluster galaxies have radial velocity in the range $v_{\rm min} = 4620$ km s^{-1} to $v_{\rm max} = 10\,000$ km s^{-1}, which is the range in radial velocity among spectroscopically confirmed members in the ACS survey. We also adopt the Coma virial radius and virial mass to be 2.9 and $1.4 \times 10^{15}\,h_{70}^{-1}$ M$_\odot$, respectively, measured by Łokas & Mamon (2003) with a 30 per cent accuracy, where $h_{70}^{-1} = H_0/70$. For our adopted H_0 of 73, we scale these numbers by $(73/70)^{-1}$, so that the virial radius and virial mass are $2.8\,h_{73}^{-1}$ Mpc and $1.3 \times 10^{15}\,h_{73}^{-1}$ M$_\odot$, respectively. We select galaxies with the following criteria.

(i) Radial velocity in range 4620 to 10 000 km s^{-1}.
(ii) Projected radius, $R_{\rm p}$ from the cluster centre (i.e. NGC 4874) less than the virial radius.
(iii) Brightness exceeding the SDSS spectroscopic completeness limit of $r = 17.7$ mag, or $M_r \leq -17.3$ mag at the 100 Mpc distance of Coma. This corresponds to a stellar mass of 1.3×10^9 M$_\odot$ assuming a $g - r$ colour of 0.67, which is the average among Coma galaxies in the NYU-VAGC selected in this manner.

Panel (b) of Fig. 9 shows the resulting projected galaxy density profile for this set of Coma galaxies.

We next calculate the global galaxy stellar mass function within the virial radius. Fig. 9(c) shows the result. This mass function includes normal massive galaxies (E, S0, spiral) as well as the two cDs (NGC 4874 and NGC 4889). As described in Section 2.2, we derive the stellar mass by applying equations (5) and (6) to SDSS *gr* photometry.

Using the cD galaxy stellar masses as lower limits at the high-mass end of the galaxy stellar mass function in Fig. 9(c), we measure a slope $\alpha = -1.16$ and characteristic mass $M^* = 1.25 \times 10^{11}$ M$_\odot$ for the global galaxy stellar mass function of Coma inside the cluster virial radius.

5.3 Global properties of model clusters versus Coma

Next, we compare the above global properties of the Coma cluster with the simulated clusters in the theoretical model in order to identify the model clusters that best represent Coma. We consider all 160 friend-of-friend (FOF; Davis et al. 1985) groups in the Millennium simulation having a halo mass in the range 5×10^{14}–10^{16} M$_\odot$. We refer to the most massive halo, and its gravitationally bound subhaloes, in each FOF group as a 'cluster'.

To find potential matching clusters, we identify massive ($M_\star \geq 10^9$ M$_\odot$) member galaxies in each cluster in a way that is consistent with the selection of Coma member galaxies in Section 5.2.

(i) Radial velocity matching the range in line-of-sight velocities in the *xy*, *xz*, *yz* projections of the cluster.
(ii) Projected radius, $R_{\rm p}$, from the cluster centre less than the cluster virial radius.
(iii) Luminosity brighter than the SDSS spectroscopic completeness limit of $M_r \leq -17.3$ mag at the 100 Mpc distance of Coma.

To gauge how well the simulated clusters compare with Coma in terms of global properties, we examine the match in cumulative number density, mass function, and halo parameters (virial mass and radius).

In Fig. 9, we gauge how the global properties of Coma compare with those of all 160 cluster simulations. Fig. 9(a) shows the combinations of virial radius and halo masses of the simulated clusters. The Coma halo parameters (virial mass and radius) adopted in Section 5.2 are well matched to the largest and most massive model clusters.

Fig. 9(b) shows the radial profile of cumulative galaxy number density. The central galaxy number densities in the simulated clusters span three orders of magnitude from $\sim 10^4$ to $\sim 4 \times 10^5$ Mpc^{-3}, overlapping with the high central density in Coma ($\sim 3 \times 10^4$ Mpc^{-3}). The thick dotted line denotes the cluster model with the best-matching halo parameters from Fig. 9(a). This halo model does a good job at matching the galaxy number density profile of Coma at projected radius $R_{\rm p} > 0.7$ Mpc, but not at smaller projected radii. In comparison, the model with the best-matching cumulative number density profile, shown as the open circle in Fig. 9(a), is smaller by $\sim$60 per cent in halo mass than Coma. The next nine best matches to cumulative number density also differ in halo mass by $\sim$30 per cent or more from the halo mass in Coma, which is estimated to be accurate to within 30 per cent (Section 5.2).

Fig. 9(c) compares the galaxy stellar mass function between Coma and the simulated model clusters. All the model clusters produce too many extremely massive ($M_\star \gtrsim 5 \times 10^{11}$ M$_\odot$) galaxies. These very high mass galaxies are not devoid of ongoing SF like ellipticals in Coma (Section 4.5). Rather, these galaxies have present-day SFR of $\sim$10 M$_\odot$ yr^{-1}. Furthermore, the cluster mass functions show slopes that are marginally too steep ($\alpha \sim -1.5$ versus $\alpha = -1.16$) on the low-mass end (Section 5.2).

We note that when this SAM model was compared with SDSS observations of galaxies averaged over all environments at low redshift (Wang et al. 2012), the model galaxy stellar mass function shows a similar, but less extreme, discrepancy with the galaxy stellar mass function of Li & White (2009) in terms of producing too many of the most massive galaxies. Fig. 9(c) includes the galaxy stellar mass function from Li & White (2009) as a dashed line for comparison.

In Fig. 10 we make the comparison with three sets of model clusters (a total of 30 model clusters) containing the 10 best matches to Coma in terms of the cumulative galaxy number density, galaxy stellar mass function, and halo parameters. Matching to one criterion (e.g. cumulative number density) does not ensure a good match to the other two criteria.

We are left with the sobering conclusion that the simulations cannot produce a model cluster simultaneously matching multiple global properties of Coma, our local benchmark for one of the richest nearby galaxy clusters. The large discrepancy in the galaxy stellar mass function between the model and Coma could be due to a number of factors. The model currently does not include tidal stripping/disruption of stars and ram-pressure stripping (Section 5.1), which would reduce the stellar mass of galaxies on all mass scales.

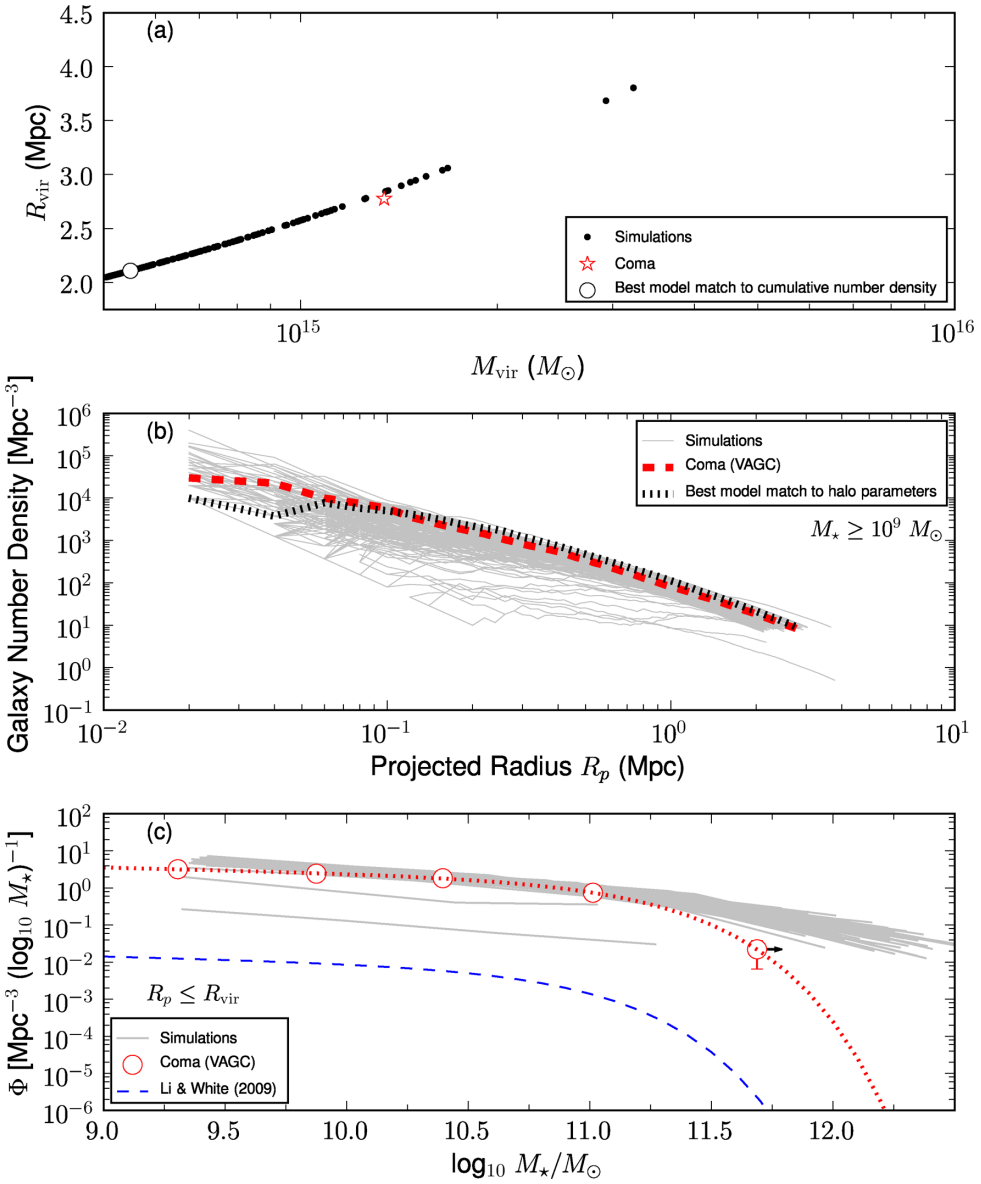

Figure 9. Shows how the global parameters of the Coma cluster compare with all 160 clusters in the Millennium simulation having a halo mass in the range 5×10^{14}–10^{16} M$_\odot$. The solid lines and black data points represent the simulated clusters. In panel (a), the virial mass and virial radius adopted for Coma are 2.8 h_{73}^{-1} Mpc and $1.3 \times 10^{15}\ h_{73}^{-1}$ M$_\odot$ (Section 5.2). The open circle is the model cluster having the best match to the projected galaxy number density of Coma. In panels (b) and (c), the cumulative projected galaxy number density and the galaxy mass stellar function of Coma at projected radius $R_{\rm p} \leq R_{\rm vir}$ are based on data from the NYU-VAGC (Blanton et al. 2005). In panel (b), the dotted line represents the cumulative galaxy number density of the model cluster best matching the Coma halo parameters. In panel (c), for the Coma galaxy stellar mass function, we measure a slope $\alpha = -1.16$ and characteristic mass $M^* = 1.17 \times 10^{11}$ M$_\odot$. The last mass bin in the global mass function for Coma contains the two cD galaxies, and the arrow on this bin indicates that the adopted stellar masses for the cDs are lower limits. The simulations are based on a model that produces a reasonable match to the galaxy stellar mass function of Li & White (2009) averaged over all environments at $0.001 < z < 0.5$ (dashed line). However, they cannot produce a model cluster that simultaneously matches multiple global properties (halo properties, galaxy number density, and galaxy stellar mass function), of Coma, our local benchmark for one of the richest nearby galaxy clusters.

The importance of ram-pressure stripping is further discussed in Section 5.5, where we find that the cold gas fraction in the model galaxies is much higher in Coma galaxies.

5.4 Strong dependence of results on mass ratio used to define mergers

Merger history and galaxy B/T are highly dependent on the mass used (stellar mass, baryonic mass, and halo mass) to define merger mass ratio M_1/M_2. For a single representative cluster model, Fig. 11 highlights the key differences that arise when M_1/M_2 is defined as the ratio of stellar mass (Def 1, left-hand column) versus cold gas plus stars (Def 2, right-hand column). This representative cluster was selected because it is the best-matching cluster to the cumulative galaxy number density distribution in Coma (Fig. 10). The first row of Fig. 11 shows the cumulative percentage of galaxies with a major merger since redshift z. In the second row of Fig. 11, the histograms show the percentage of galaxies with a last major merger at redshift

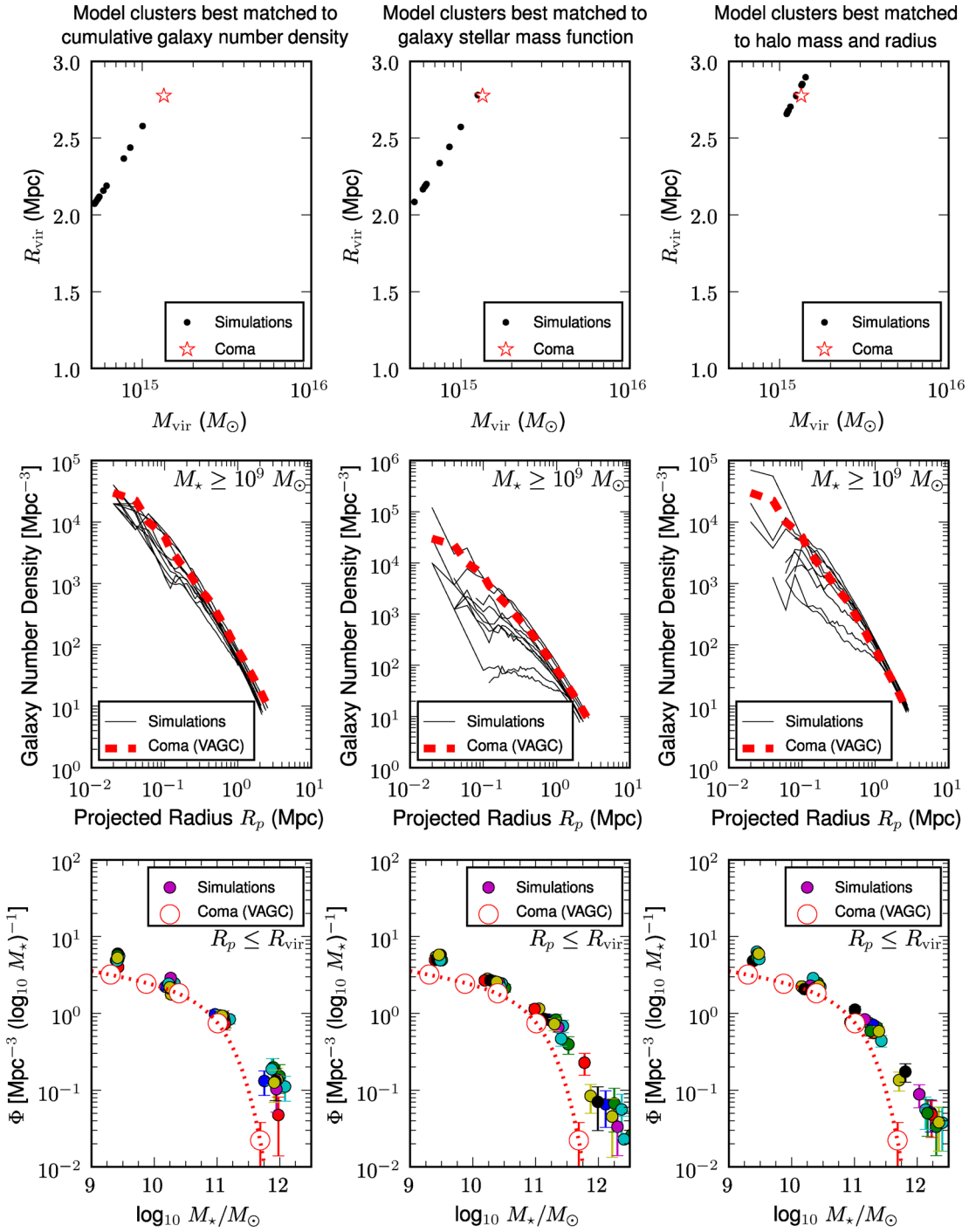

Figure 10. Shows the three sets of simulated model clusters (30 model clusters in total) chosen to best match, separately, the cumulative galaxy number density (column 1), the galaxy stellar mass function (column 2), and halo parameters (halo mass and virial radius, column 3). The solid lines and solid circles in each panel represent the different simulated clusters. Rows 1, 2, and 3 show how the different simulated clusters compare with the global properties (halo mass and radius, cumulative galaxy number density, and galaxy stellar mass function) determined with data from the NYU-VAGC (Blanton et al. 2005) for Coma in Section 5.2. No model cluster simultaneously matches all three global properties.

z. The third row shows the percentage of galaxies with a given B/T value, sorted by galaxies with and without a major merger. Finally, the last row of Fig. 11 gives the distribution of present-day B/T versus redshift of the last major merger.

In the following sections, we consider a model where the merger mass ratio M_1/M_2 depends on stellar mass plus cold gas, as this ratio is understood to be the most appropriate definition (Hopkins et al. 2009b). Traditionally, observers have tended to use stellar mass ratios in identifying mergers (e.g. Lin et al. 2004; Bell et al. 2006; Jogee et al. 2009; Robaina et al. 2010) as stellar masses are readily measured for a large number of galaxies. However, with the advent of the Atacama Large Millimeter Array (ALMA), it will be increasingly possible to incorporate the cold gas mass for a large number of galaxies.

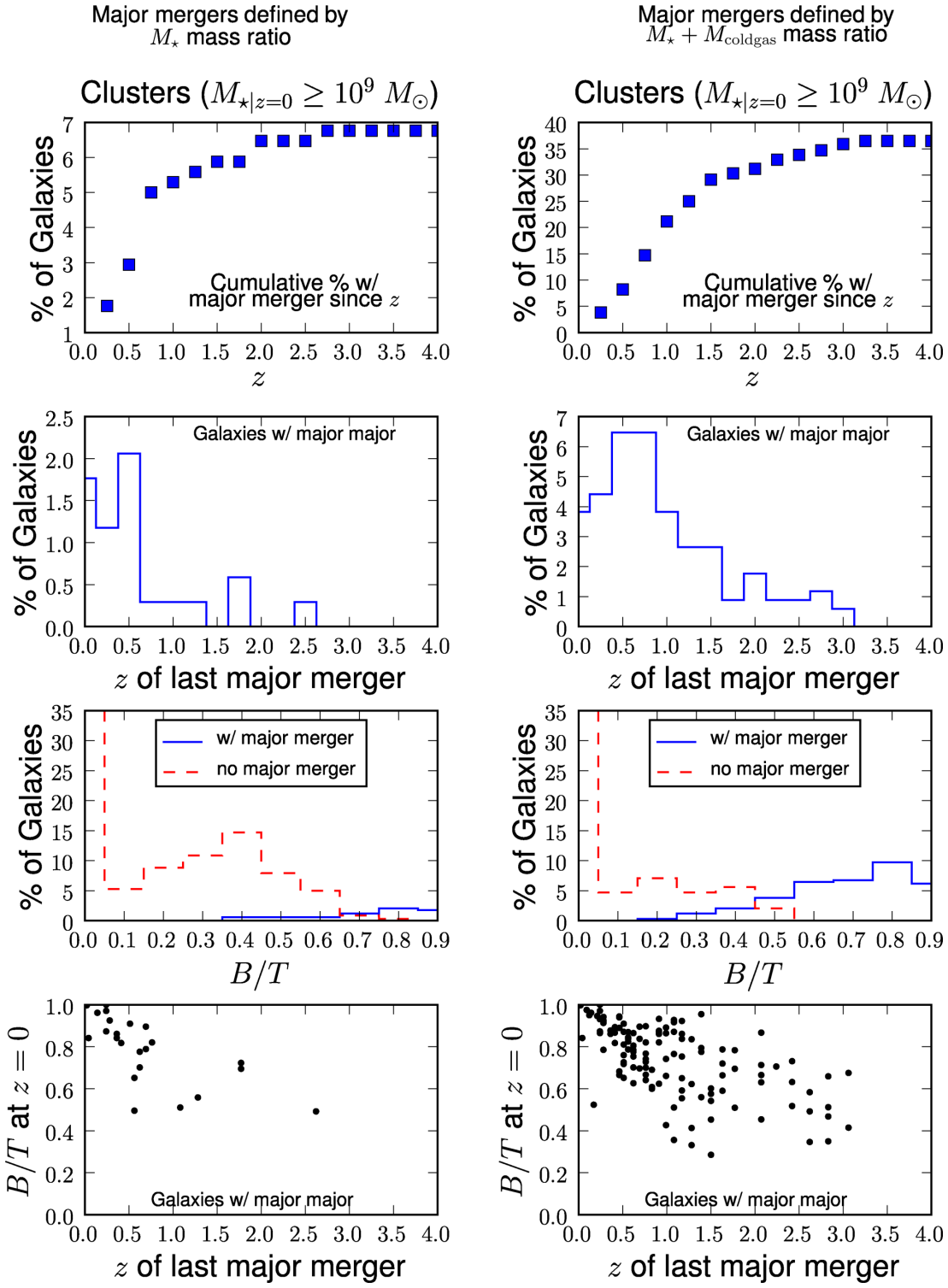

Figure 11. Highlights the effect that the definition of the merger mass ratio M_1/M_2 has on certain galaxy properties (merger history and B/T), for a representative model cluster (see Section 5.4). Note we require a major merger to have $M_1/M_2 \geq 1/4$. The left-hand column is the manifestation of the model cluster when M_1/M_2 refers to the stellar mass ratio, and in the right-hand column the merger mass ratio represents cold gas plus stars. The two mass ratio definitions lead to vastly different merger histories and significantly affect the resulting distribution of B/T.

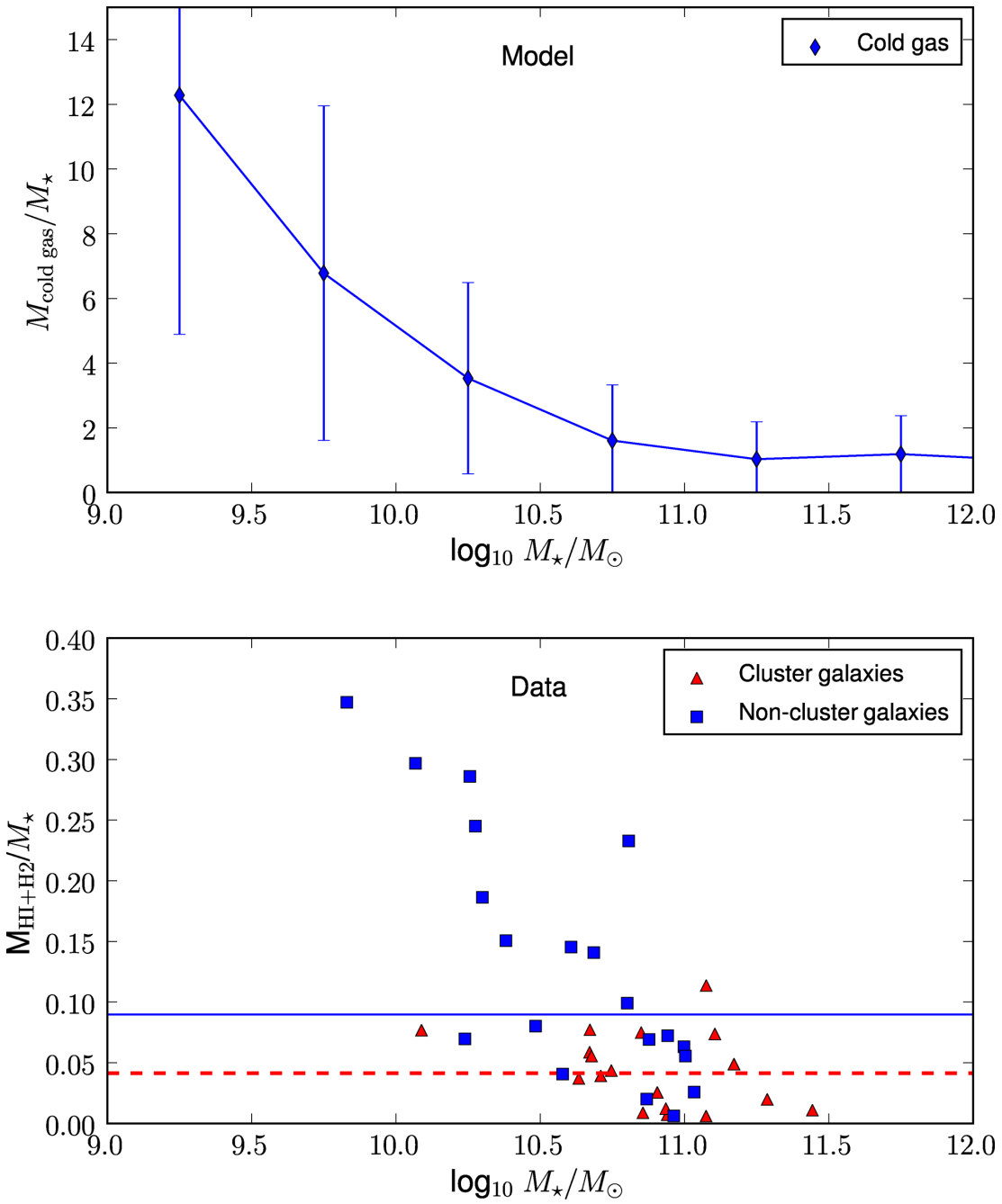

Figure 12. The top panel shows the ratio of cold gas to stellar mass ($M_{\rm cold\_gas}/M_\star$) for the best cluster model matched by cumulative galaxy number density (see Fig. 10, column 1). The error bars represent the 1σ standard deviation around the mean value. The bottom panel shows the ratio of observed cold gas (H I+H_2) to stellar mass ($M_{\rm H\,I+H_2}/M_\star$) for galaxies studied by Boselli et al. (1997) that are part of or near the Coma cluster. The dashed line is the median ratio (0.04) for Coma cluster galaxies, and the solid line is the median ratio (0.09) for the non-cluster galaxies. At $10^{10} \lesssim M_\star \lesssim 10^{11}$ $M_\odot$, the model predicts a cold gas to stellar mass ratio that is a factor of ∼25–87 times higher than the median value observed in Coma cluster galaxies.

5.5 Cold gas mass in Coma galaxies versus model galaxies

In the SAM used here, the cold gas fraction $f_{\rm gas}$ (defined as the ratio of cold gas to the baryonic mass made of cold gas, hot gas, and stars) and the ratio ($M_{\rm cold\_gas}/M_\star$) of cold gas to stellar mass are both overly high. The issue of high cold gas fraction in this model was highlighted and discussed in Wang et al. (2012). Here, we quantify how far off the model values are compared with what is expected for a rich cluster like Coma.

Fig. 12 illustrates the degree to which the ratio ($M_{\rm cold\_gas}/M_\star$) is overestimated by comparing with data from Boselli et al. (1997), who measure atomic ($M_{\rm H\,I}$) and molecular gas ($M_{\rm H_2}$) masses for Coma cluster member galaxies and non-cluster galaxies. The top panel shows that the average ratio of cold gas to stellar mass ($M_{\rm cold\_gas}/M_\star$) ranges from ∼1 to 12 for a representative model cluster. The bottom panel shows that the ratio of $M_{\rm H\,I+H_2}/M_\star$ for Coma cluster galaxies from Boselli et al. (1997) is usually <0.1;

non-cluster galaxies are more gas rich, but the ratio of $M_{\rm H\,I+H_2}/M_\star$ is still $\ll$1. At $10^{10} \lesssim M_\star \lesssim 10^{11}$ M$_\odot$, the model predicts a cold gas to stellar mass ratio that is a factor of ∼25–87 times higher than the median in Coma cluster galaxies.

5.6 Data versus model predictions for stellar mass in dynamically hot and cold components

We next proceed to compare the observed versus model predictions for the distribution of mass in dynamically hot and cold stellar components. The following comparisons are made in the projected central 0.5 Mpc of Coma and the model clusters.

We first start by describing how the model builds bulges and ellipticals. In the model, the total bulge stellar mass $M_{\star,\,\rm Bulge,\,model}$ consists of stellar mass accreted in major and minor mergers, plus stellar mass from SF induced in both types of mergers.

Next, we discuss how to compare the model with the data. For our sample of Coma galaxies (excluding the two cD systems) with $M_\star \geq 10^9$ M$_\odot$, we compute the ratio $R1_{\rm data}$ as the stellar mass in all components with $n > n_{\rm disc\_max}$ to the sum of galaxy stellar mass. The reasons for not including the cD systems were discussed in Section 2.2. From Section 4.2, $R1_{\rm data}$ is 57 per cent.

We next compare this ratio to the corresponding quantity in the model. The comparison is not entirely straightforward as the model does not give a Sérsic index. We therefore have to associate components in the model to the corresponding high $n > n_{\rm disc\_max}$ classical bulges/ellipticals in the data. The most natural step is to assume that the stellar mass built during major mergers is redistributed into such high-n components. We call the result $R2_{\rm model}$. We find that for $M_\star \geq 10^9$ M$_\odot$, $R2_{\rm model}$ has a wide dispersion: ∼35–79 per cent for the 30 model clusters shown in Fig. 10, with a median value of ∼66 per cent. The representative cluster discussed in Section 5.4 and Figs 11 and 12 has a value of ∼72 per cent.

Guidance on the Sérsic index of structures formed during minor mergers can be gleaned from Hopkins et al. (2009b). In the general case of an unequal mass merger, the coalescence of the smaller progenitor (mass M_1) with the centre of the primary will destroy (i.e. violently relax) the smaller galaxy and also potentially violently relax an additional mass $\leq M_1$ in the primary. The stars that are violently relaxed in the minor merger become part of the bulge in the primary galaxy. Thus, we define $R3_{\rm model}$ to be $R2_{\rm model}$ plus the stellar accretion from minor mergers. For $M_\star \geq 10^9$ M$_\odot$, $R3_{\rm model}$ is only slightly higher than $R2_{\rm model}$ by a few per cent. $R3_{\rm model}$ ranges from ∼35 to 82 per cent, with a median value of ∼71 per cent, and the representative cluster (Section 5.4, Figs 11 and 12) has a value of ∼71 per cent.

The comparison of $R1_{\rm data}$ with $R2_{\rm model}$ and $R3_{\rm model}$ is a global comparison of the total stellar mass fraction within high-n components *summed over all* the galaxies with $M_\star \geq 10^9$ M$_\odot$. Next, we push the data versus model comparison one step further by doing it in bins of stellar mass, as shown in Fig. 13.

The top panel of Fig. 13 plots the mean ratio of stellar mass fraction in dynamically hot components ($f_{\star,\,\rm hot}$) as a function of total galaxy stellar mass, for data versus model. For each stellar mass bin shown in Fig. 13, the value of $f_{\star,\,\rm hot}$ is calculated for *each galaxy* as $M_{\star,\,\rm hot}/M_\star$. In the data, $M_{\star,\,\rm hot}$ is taken as the stellar mass of any high $n > n_{\rm disc\_max}$ component in the galaxy. The model shown here is the best cluster model matched by cumulative galaxy number density (see Fig. 10, column 1). For this model, two lines are shown: the solid line takes $M_{\star,\,\rm hot}$ as the stellar mass accreted and formed during major mergers, while the dotted line also adds in the stellar mass accreted during minor mergers.

In the top panel of Fig. 13 there is significant disagreement between the fractions of $f_{\star,\,\rm hot}$ for the Coma data and the model. As shown by the second dotted model curve in Fig. 13, adding in the stellar mass accreted in minor mergers to the model only changes the fraction by a few per cent. The values of $f_{\star,\,\rm hot}$ are chiefly representative of the contributions from major mergers.

The bottom panel of Fig. 13 plots the analogous mean ratio of stellar mass fraction in dynamically cold components ($f_{\star,\,\rm cold} = M_{\star,\,\rm cold}/M_\star$) as a function of total galaxy stellar mass. In the model, the two lines show two different expressions for $M_{\star,\,\rm cold}$. For the solid line, we take $M_{\star,\,\rm cold}$ to be the mass of the outer disc $M_{\star,\rm Outer\_disc}$, which represents the difference between the bulge mass ($M_{\star,\rm Bulge,model}$) and the total stellar mass. One problem with this approach is that it ignores small-scale nuclear discs formed in the bulge region. We tackle this problem by defining a second dotted model line that accounts for stars formed via induced SF during minor mergers. It is clear in the bottom panel of Fig. 13 that the model overpredicts the mass in discs as a function of galaxy stellar mass. Note that the contribution to $f_{\star,\,\rm cold}$ from minor merger induced SF is $\lesssim$ 17 per cent in a stellar mass given bin.

The main conclusion from Fig. 13 is that the best-matching cluster model is underpredicting the mean fraction $f_{\star,\,\rm hot}$ of stellar mass locked in hot components over a wide range in galaxy stellar mass ($10^9 \leq M\star \lesssim 8 \times 10^{10}$ M$_\odot$). Similarly this model overpredicts the mean value for $f_{\star,\,\rm cold}$. The effect of cosmic variance on our sample (Section 4.2 and Appendix B5) means our measured $f_{\star,\,\rm hot}$ is lower than the true value by an estimated factor of 1.16. Therefore, the underprediction of $f_{\star,\,\rm hot}$ in the model is worse than what we are citing. While the discussion in this section focused only on a single model cluster, the results and conclusions would be similar if we had analysed alternate simulated clusters, such as those matched to the cluster galaxy stellar mass function (see Fig. 10, column 2) or halo parameters (see Fig. 10, column 3).

There could be several explanations as to why the models are underproducing the fraction of dynamically hot stellar mass ($f_{\star,\,\rm hot}$) and overproducing the fraction of dynamically cold stellar mass ($f_{\star,\,\rm cold}$). One possibility is that the absence of key cluster processes (especially ram-pressure stripping and tidal stripping) in the models is leading to the overproduction of the model galaxy's cold gas reservoir (Section 5.5), compared to a real cluster galaxy, whose outer gas would be removed. This means that in the models, SF in gas that would otherwise be removed from the galaxy builds additional dynamically cold stellar mass following the last major merger. Another possibility is that the models ignore the production of bulges via the merging of star-forming clumps (Bournaud et al. 2007a; Elmegreen et al. 2009). It is still debated whether this mode can efficiently produce classical bulges, but if it does, then its non-inclusion in the models could lead to the underprediction of $f_{\star,\,\rm hot}$.

In summary, our comparison of empirical results to theoretical predictions underscores the need to include in SAMs environmental processes, such as ram-pressure stripping and tidal stripping, which affect the cold gas content of galaxies, as well as more comprehensive models of bulge assembly. It is clear that galaxy evolution is a function of *both* stellar mass and environment.

6 SUMMARY AND CONCLUSIONS

We present a study of the Coma cluster in which we constrain galaxy assembly history in the projected central 0.5 Mpc by performing

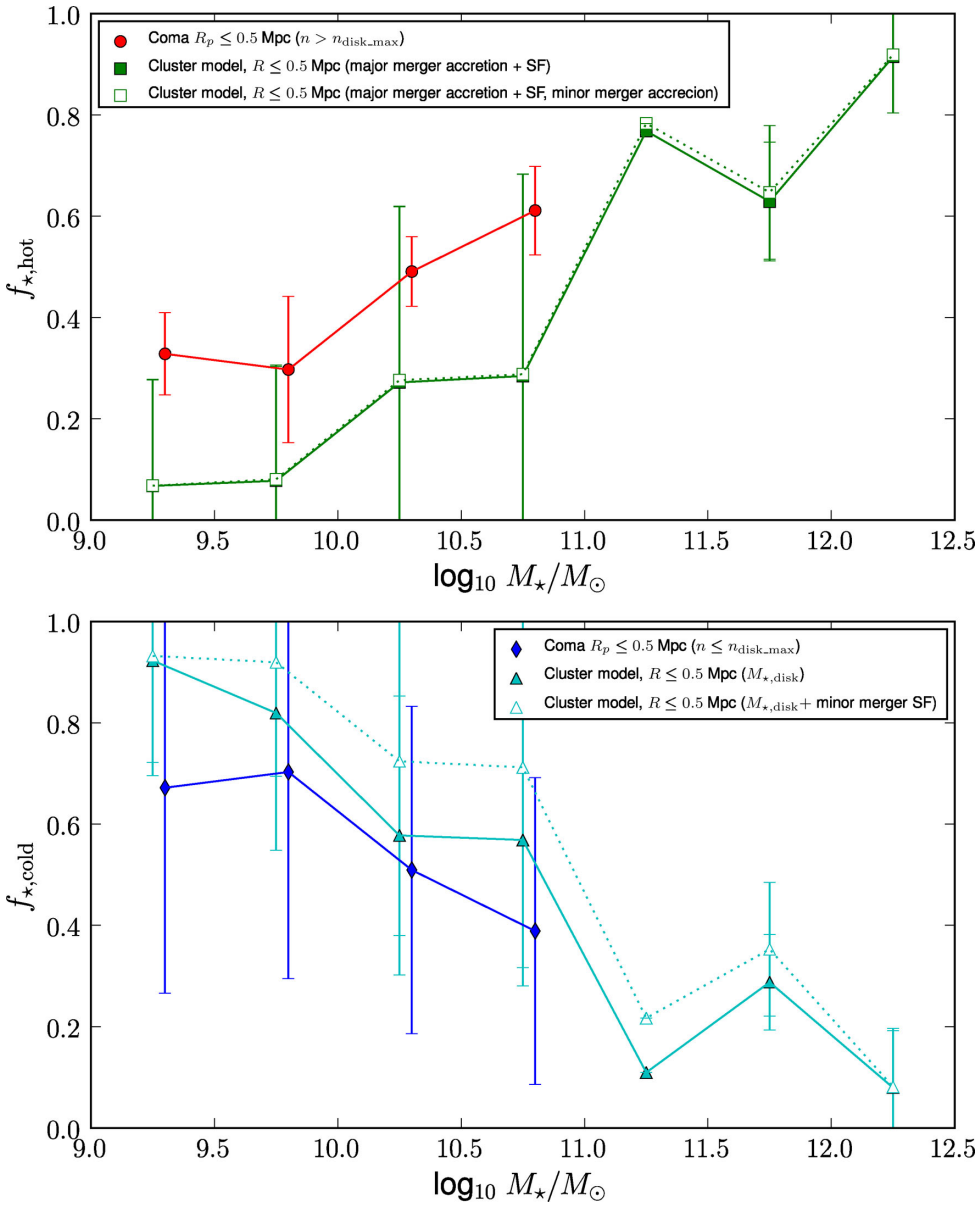

Figure 13. Top: the mean ratio of stellar mass fraction in dynamically hot components ($f_{\star,\rm hot} = M_{\star\,\rm hot}/M_\star$) is plotted as a function of total galaxy $M_\star$. In the data, $M_{\star,\rm hot}$ is taken as the stellar mass of any high $n > n_{\rm disc\_max}$ classical bulge/elliptical component in the galaxy, excluding the cD galaxies (see Section 2.2). The model shown here is the best cluster model matched by cumulative galaxy number density (see Fig. 10, column 1). For this model, the solid line takes $M_{\star,\rm hot}$ as the stellar mass built during major mergers, namely major merger stellar accretion plus induced SF, while the dashed line further adds in minor merger stellar accretion. Bottom: the mean stellar mass fraction in dynamically cold flattened components ($f_{\star,\rm cold} = M_{\star,\rm cold}/M_\star$) is plotted as a function of total galaxy stellar mass $M_\star$. In the data, $M_{\star,\rm cold}$ is taken as the stellar mass of any low $n \leq n_{\rm disc\_max}$ disc-dominated component in the galaxy. The model is represented by the solid and dashed lines. With the solid line we take $M_{\star,\rm cold}$ to be the mass of the *outer* disc $M_{\star,\rm Outer\_disc}$, which is given by ($M_\star - M_{\star,\rm Bulge,model}$). For the dotted line, we consider $M_{\star,\rm cold}$ to be the mass $M_{\star,\rm all\_disc}$ of inner and outer discs. We compute the latter mass as $M_{\star,\rm Outer\_disc}$ plus the mass of stars formed via induced SF during minor mergers. In both panels, only the projected central 0.5 Mpc of the clusters is considered. The error bars represent the 1σ standard deviation on the mean. The mean values for Coma are slightly offset in $M_\star$ for readability. The main conclusion is that the best-matching simulated clusters are underpredicting the mean fraction of $f_{\star,\rm hot}$ and overpredicting $f_{\star,\rm cold}$ over a wide range in galaxy stellar mass.

multicomponent structural decomposition on a mass-complete sample of 69 galaxies with stellar mass $M_\star \geq 10^9$ M$_\odot$. Some strengths of this study include the use of superb high-resolution (0.1 arcsec), *F*814*W* images from the *HST*/ACS Treasury Survey of the Coma cluster, and the adoption of a multicomponent decomposition strategy where no a priori assumptions are made about the Sérsic index of bulges, bars or discs. We use structural decomposition to identify the two fundamental kinds of galaxy structure – dynamically cold, disc-dominated components and dynamically hot classical bulges/ellipticals – by adopting the working assumption that the Sérsic index n is a reasonable proxy for tracing different structural components. We define disc-dominated structures as components with a low Sérsic index n below an empirically determined threshold value $n_{\rm disc\_max} \sim 1.7$ (Section 3.1). Galaxies with an outer disc are called spirals or S0s. We explore the effect of environment by performing a census of disc-dominated structures versus classical bulges/ellipticals in Coma. We also compare our empirical results on galaxies in the centre of the Coma cluster

with theoretical predictions from a SAM. Our main results are summarized below.

(i) *Breakdown of stellar mass in Coma between low-n disc-dominated structures and high-*n *classical bulges/ellipticals*. We make the first attempt (Section 4.2 and Tables 7 and 8) at exploring the distribution of stellar mass in Coma in terms of dynamically hot versus dynamically cold stellar components. After excluding the two cDs because of their uncertain stellar masses, we find that in the projected central 0.5 Mpc of the Coma cluster, galaxies with stellar mass $M_\star \geq 10^9$ $M_\odot$ have 57 per cent of their cumulative stellar mass locked up in high-n ($n \gtrsim 1.7$) classical bulges/ellipticals while the remaining 43 per cent is in the form of low-n ($n \lesssim 1.7$) disc-dominated structures (outer discs, inner discs, discy pseudo-bulges, and bars). Accounting for the effect of cosmic variance and colour gradients in calculating these stellar mass fractions would not significantly change this census (Appendices B5 and B6).

(ii) *Impact of environment on morphology–density relation*. Using our structural decomposition to assign galaxies the Hubble types E, S0, or spiral, we find evidence of a strong morphology–density relation. In the projected central 0.5 Mpc of the Coma cluster, spirals are rare, and the morphology breakdown of (E+S0):spirals is (91.0 per cent):9.0 per cent by numbers and (94.2 per cent):5.8 per cent by stellar mass (Section 4.1 and Table 6).

(iii) *Impact of environment on outer discs*. In the central parts of Coma, the properties of large-scale discs are likely indicative of environmental processes that suppress disc growth or truncate discs (Section 4.5). In particular, at a given galaxy stellar mass, outer discs are smaller by ∼30–82 per cent and fainter in the i band by ∼40–70 per cent (Fig. 5). The suggestion that outer discs in Coma are more compact is consistent with the results of previous analyses of disc structure in Coma (Aguerri et al. 2004; Gutiérrez et al. 2004).

(iv) *Impact of environment on bulges*. The ratio R of stellar mass in high-n ($n \gtrsim 1.7$) classical bulges to low-n ($n \lesssim 1.7$) discy pseudo-bulges is 17.3 in Coma. We measure R to be a factor of ∼2.2−2.7 higher in Coma compared with various samples from LDEs (Sections 4.2–4.3, Tables 7–8). We also find that at a given bulge Sérsic index n, the bulge-to-total ratio B/D, and the i-band light ratio are offset to higher values in Coma compared with LDEs. This effect appears to be due, at least in part, to the above-mentioned lower disc luminosity in Coma.

(v) *Comparison of data to theoretical predictions*. We compare our empirical results on galaxies in the centre of the Coma cluster with theoretical predictions based on combining the Millennium cosmological simulations of dark matter (Springel et al. 2005) with baryonic physics from a SAM (Neistein & Weinmann 2010; Wang et al. 2012).

It is striking that no model cluster can simultaneously match the global properties (halo mass/size, cumulative galaxy number density, and galaxy stellar mass function) of Coma (Figs 9 and 10), and the cold gas to stellar mass ratio in the model clusters are at least 25 times higher than is measured in Coma.

As suggested by Hopkins et al. (2009b), we find galaxy merger history is highly dependent on how the merger mass ratio M_1/M_2 is defined. Specifically, there is a factor of ∼5 difference in merger rate when the merger mass ratio is based on the baryonic mass versus the stellar mass (Fig. 11). Traditionally, observers have tended to use stellar mass ratios in identifying mergers, but with the advent of ALMA, it will be increasingly possible and important to incorporate the cold gas mass.

For representative 'best-matching' simulated clusters, we compare the empirical and theoretically predicted fraction $f_{\star,\,\rm hot}$ and $f_{\star,\,\rm cold}$ of stellar mass locked, respectively, in high-n, dynamically hot versus low-n, dynamically cold stellar components. Over a wide range of galaxy stellar mass ($10^9 \leq M_\star \lesssim 8 \times 10^{10}$), the model underpredicts the mean fraction $f_{\star,\,\rm hot}$ of stellar mass locked in hot components by a factor of $\gtrsim$1.5. Similarly, the model overpredicts the mean value for $f_{\star,\,\rm cold}$ (Section 5.6 and Fig. 13).

We suggest that this disagreement might be due to two main factors. First, key cluster processes (especially ram-pressure stripping and tidal stripping), which impact that the cold gas content and disc-dominated components of galaxies, are absent. Secondly, the models ignore the production of bulges via the merging of star-forming clumps (Bournaud et al. 2007a; Elmegreen et al. 2009). These results underscore the need to implement in theoretical models environmental processes, such as ram-pressure stripping and tidal stripping, as well as more comprehensive models of bulge assembly. It is clear that galaxy evolution is not a solely a function of stellar mass, but it also depends on environment.

ACKNOWLEDGEMENTS

SJ and TW acknowledge support from the National Aeronautics and Space Administration (NASA) LTSA grant NAG5-13063, NSF grant AST-0607748, and *HST* grants GO-11082 and GO-10861 from STScI, which is operated by AURA, Inc., for NASA, under NAS5-26555. SJ and TW also acknowledge support from the Norman Hackerman Advanced Research Program (NHARP) ARP-03658-0234-2009, National Aeronautics and Space Administration (NASA) LTSA grant NAG5-13063, and NSF grant AST-0607748. SJ and TW acknowledge support for this research by the DFG cluster of excellence 'Origin and Structure of the Universe' (www.universe-cluster.de). MB acknowledges support from grant AYA2009-11137 from the Spanish Ministry of Science and Technology. We thank Roderik Overzier, T. J. Cox, and Jennifer Lotz for stimulating discussions. This work made use of observations with the NASA/ESA *Hubble Space Telescope* obtained at the Space Telescope Science Institute, which is operated by the Association of Universities for Research in Astronomy, Inc., under NASA contract NAS 5-26555. These observations are associated with programme GO10861. We acknowledge the usage of the HyperLeda data base (http://leda.univ-lyon1.fr). Funding for the Sloan Digital Sky Survey (SDSS) has been provided by the Alfred P. Sloan Foundation, the Participating Institutions, the National Aeronautics and Space Administration, the National Science Foundation, the U.S. Department of Energy, the Japanese Monbukagakusho, and the Max Planck Society. The SDSS website is http://www.sdss.org/. The SDSS is managed by the Astrophysical Research Consortium (ARC) for the Participating Institutions. The Participating Institutions are The University of Chicago, Fermilab, the Institute for Advanced Study, the Japan Participation Group, The Johns Hopkins University, Los Alamos National Laboratory, the Max-Planck-Institute for Astronomy (MPIA), the Max-Planck-Institute for Astrophysics (MPA), New Mexico State University, University of Pittsburgh, Princeton University, the United States Naval Observatory, and the University of Washington.

REFERENCES

Abazajian K. N. et al., 2009, ApJS, 182, 543
Adami C. et al., 2005, A&A, 429, 39
Adelman-McCarthy J. K. et al., 2008, ApJS, 175, 297

Aguerri J. A. L., Balcells M., Peletier R. F., 2001, A&A, 367, 428
Aguerri J. A. L., Iglesias-Paramo J., Vilchez J. M., Muñoz-Tuñón C., 2004, AJ, 127, 1344
Ahn C. P. et al., 2013, ApJS, 211, 17
Allen P. D., Driver S. P., Graham A. W., Cameron E., Liske J., de Propris R., 2006, MNRAS, 371, 2
Andredakis Y. C., Peletier R. F., Balcells M., 1995, MNRAS, 275, 874
Aragon-Salamanca A., Baugh C. M., Kauffmann G., 1998, MNRAS, 297, 427
Arnaboldi M., 2011, paper presented at the ES0 Workshop on Fornax, Virgo, Coma et al.: Stellar Systems in High Density Environments, http://www.eso.org/sci/meetings/2011/fornax_virgo2011/talks_pdf/Arnaboldi_Magda.pdf
Athanassoula E., 2005, MNRAS, 358, 1477
Baggett W. E., Baggett S. M., Anderson K. S. J., 1998, AJ, 116, 1626
Balcells M., Graham A. W., Domínguez-Palmero L., Peletier R. F., 2003, ApJ, 582, L79
Balcells M., Graham A. W., Peletier R. F., 2007a, ApJ, 665, 1084
Balcells M., Graham A. W., Peletier R. F., 2007b, ApJ, 665, 1104
Barazza F. D., Jogee S., Marinova I., 2007, in Combes F., Palous J., eds, Proc. IAU Symposium 235, Galaxy Evolution across the Hubble Time. Cambridge Univ. Press, Cambridge, p. 76
Barazza F. D., Jogee S., Marinova I., 2008, ApJ, 675, 1194
Barentine J. C., Kormendy J., 2012, ApJ, 754, 140
Barnes J. E., 1988, ApJ, 331, 699
Barnes J. E., Hernquist L. E., 1991, ApJ, 370, L65
Bell E. F., McIntosh D. H., Katz N., Weinberg M. D., 2003, ApJS, 149, 289
Bell E. F., Phleps S., Somerville R. S., Wolf C., Borch A., Meisenheimer K., 2006, ApJ, 652, 270
Bernstein G. M., Nichol R. C., Tyson J. A., Ulmer M. P., Wittman D., 1995, AJ, 110, 1507
Binggeli B., Tammann G. A., Sandage A., 1987, AJ, 94, 251
Binney J., Merrifield M., 1998, Galactic Astronomy. Princeton Univ. Press, Princeton
Binney J., Tremaine S., 1987, Galactic Dynamics. Princeton Univ. Press, Princeton
Birnboim Y., Dekel A., 2003, MNRAS, 345, 349
Blanton M. R. et al., 2005, AJ, 129, 2562
Böker T., Laine S., van der Marel R. P., Sarzi M., Rix H.-W., Ho L. C., Shields J. C., 2002, AJ, 123, 1389
Borch A. et al., 2006, A&A, 453, 869
Boroson T., 1981, ApJS, 46, 177
Boselli A., Gavazzi G., Lequeux J., Buat V., Casoli F., Dickey J., Donas J., 1997, A&A, 327, 522
Bournaud F., Elmegreen B. G., Elmegreen D. M., 2007a, ApJ, 670, 237
Bournaud F., Jog C. J., Combes F., 2007b, A&A, 476, 1179
Brooks A. M., Governato F., Quinn T., Brook C. B., Wadsley J., 2009, ApJ, 694, 396
Bullock J. S., Kravtsov A. V., Weinberg D. H., 2001, ApJ, 548, 33
Bureau M., Athanassoula E., 2005, ApJ, 626, 159
Byun Y. I., Freeman K. C., 1995, ApJ, 448, 563
Cappellari M., 2013, ApJ, 778, L2
Carter D. et al., 2008, ApJS, 176, 424
Cayatte V., van Gorkom J. H., Balkowski C., Kotanyi C., 1990, AJ, 100, 604
Cayatte V., Kotanyi C., Balkowski C., van Gorkom J. H., 1994, AJ, 107, 1003
Ceverino D., Dekel A., Bournaud F., 2010, MNRAS, 404, 2151
Chiboucas K., Tully R. B., Marzke R. O., Trentham N., Ferguson H. C., Hammer D., Carter D., Khosroshahi H., 2010, ApJ, 723, 251
Chung A., van Gorkom J. H., Kenney J. D. P., Vollmer B., 2007, ApJ, 659, L115
Chung A., van Gorkom J. H., Kenney J. D. P., Crowl H., Vollmer B., 2009, AJ, 138, 1741
Cole S., Lacey C. G., Baugh C. M., Frenk C. S., 2000, MNRAS, 319, 168
Colless M., Dunn A. M., 1996, ApJ, 458, 435
Combes F., Sanders R. H., 1981, A&A, 96, 164
Combes F., Debbasch F., Friedli D., Pfenniger D., 1990, A&A, 233, 82
Côté P. et al., 2006, ApJS, 165, 57
Davis M., Efstathiou G., Frenk C. S., White S. D. M., 1985, ApJ, 292, 371
de Grijs R., Kregel M., Wesson K. H., 2001, MNRAS, 324, 1074
de Jong R. S., 1996, A&AS, 118, 557
De Lucia G., Blaizot J., 2007, MNRAS, 375, 2
de Vaucouleurs G., de Vaucouleurs A., Corwin H. G., Jr, Buta R. J., Paturel G., Fouque P., 1991, Third Reference Catalogue of Bright Galaxies. Springer-Verlag, New York
Dekel A., Birnboim Y., 2006, MNRAS, 368, 2
Dekel A., Sari R., Ceverino D., 2009a, ApJ, 703, 785
Dekel A. et al., 2009b, Nature, 457, 451
den Brok M. et al., 2011, MNRAS, 414, 3052
Dressler A., 1980, ApJ, 236, 351
Edwards L. O. V., Fadda D., 2011, AJ, 142, 148
El-Zant A. A., Kim W.-T., Kamionkowski M., 2004, MNRAS, 354, 169
Eliche-Moral M. C., Balcells M., Aguerri J. A. L., González-García A. C., 2006, A&A, 457, 91
Elmegreen B. G., Elmegreen D. M, Fernandez M. X., Lemonias J. J., 2009, ApJ, 692, 12
Erwin P., Beckman J. E., Pohlen M., 2005, ApJ, 626, L81
Fabricius M. H., Saglia R. P., Fisher D. B., Drory N., Bender R., Hopp U., 2012, ApJ, 754, 67
Fasano G., Poggianti B. M., Couch W. J., Bettoni D., Kjæ rgaard P., Moles M., 2000, ApJ, 542, 673
Feldmeier J. J., Ciardullo R., Jacoby G. H., Durrell P. R., 2004, ApJ, 615, 196
Fisher D. B., Drory N., 2008, AJ, 136, 773
Fossati M., Gavazzi G., Boselli A., Fumagalli M., 2012, A&A, 544, A128
Freeman K. C., 1970, ApJ, 160, 811
Fujita Y., Nagashima M., 1999, ApJ, 516, 619
Gadotti D. A., 2009, MNRAS, 393, 1531
Gavazzi G., Boselli A., Donati A., Franzetti P., Scodeggio M., 2003, astro-ph/0309388
Gnedin O. Y., 2003, ApJ, 589, 752
Godwin J. G., Metcalfe N., Peach J. V., 1983, MNRAS, 202, 113
Governato F., Willman B., Mayer L., Brooks A., Stinson G., Valenzuela O., Wadsley J., Quinn T., 2007, MNRAS, 374, 1479
Graham A. W., 2001, AJ, 121, 820
Graham A. W., Guzmán R., 2003, AJ, 125, 2936
Graham A. W., Worley C. C., 2008, MNRAS, 388, 1708
Graham A. W., Erwin P., Trujillo I., Asensio Ramos A., 2003, AJ, 125, 2951
Gregg M. D., West M. J., 1998, Nature, 396, 549
Gunn J. E., Gott J. R., III, 1972, ApJ, 176, 1
Gutiérrez C. M., Trujillo I., Aguerri J. A. L., Graham A. W., Caon N., 2004, ApJ, 602, 664
Hammer D. et al., 2010, ApJS, 191, 143
Hashimoto Y., Oemler A., Jr, Lin H., Tucker D. L., 1998, ApJ, 499, 589
Head J. T. C. G., Lucey J. R., Hudson M. J., Smith R. J., 2014, MNRAS, 440, 1690
Heiderman A. et al., 2009, ApJ, 705, 1433
Henriques B. M. B., Thomas P. A., 2010, MNRAS, 403, 768
Henriques B. M. B., Bertone S., Thomas P. A., 2008, MNRAS, 383, 1649
Hernquist L., Mihos J. C., 1995, ApJ, 448, 41
Hilz M., Naab T., Ostriker J. P., Thomas J., Burkert A., Jesseit R., 2012, MNRAS, 425, 3119
Hilz M., Naab T., Ostriker J. P., 2013, MNRAS, 429, 2924
Hopkins P. F., Cox T. J., Dutta S. N., Hernquist L., Kormendy J., Lauer T. R., 2009a, ApJS, 181, 135
Hopkins P. F., Cox T. J., Younger J. D., Hernquist L., 2009b, ApJ, 691, 1168
Hoyos C. et al., 2011, MNRAS, 411, 2439
Into T., Portinari L., 2013, MNRAS, 430, 2715
Jogee S., Scoville N., Kenney J. D. P., 2005, ApJ, 630, 837
Jogee S. et al., 2009, ApJ, 697, 1971
Kautsch S. J., Grebel E. K., Barazza F. D., Gallagher J. S., III, 2006, A&A, 445, 765
Kenney J. D. P., van Gorkom J. H., Vollmer B., 2004, AJ, 127, 3361
Kenney J. D. P., Tal T., Crowl H. H., Feldmeier J., Jacoby G. H., 2008, ApJ, 687, L69

Kent S. M., 1985, ApJS, 59, 115
Kereš D., Katz N., Weinberg D. H., Davé R., 2005, MNRAS, 363, 2
Kereš D., Katz N., Fardal M., Davé R., Weinberg D. H., 2009, MNRAS, 395, 160
Khochfar S., Burkert A., 2001, ApJ, 561, 517
Khochfar S., Ostriker J. P., 2008, ApJ, 680, 54
Khochfar S., Silk J., 2006, MNRAS, 370, 902
Khochfar S., Silk J., 2009, MNRAS, 397, 506
Kormendy J., 1977, ApJ, 217, 406
Kormendy J., 1993, in DeJonghe H., Habing H. J., eds, Proc. IAU Symp. 153, Galactic Bulges. Kluwer, Dordrecht, p. 209
Kormendy J., Bahcall J. N., 1974, AJ, 79, 671
Kormendy J., Barentine J. C., 2010, ApJ, 715, L176
Kormendy J., Bender R., 2012, ApJS, 198, 2
Kormendy J., Fisher D. B., 2005, Rev. Mex. Astron. Astrophys. Conf. Ser., 23, 101
Kormendy J., Kennicutt R. C., Jr, 2004, ARA&A, 42, 603
Kormendy J., Fisher D. B., Cornell M. E., Bender R., 2009, ApJS, 182, 216
Kormendy J., Drory N., Bender R., Cornell M. E., 2010, ApJ, 723, 54
Krist J., 1995, in Shaw R. A., Payne H. E., Hayes J. J. E., eds, ASP Conf. Ser. 77, Astronomical Data Analysis Software and Systems IV. Astron. Soc. Pac., San Francisco, p. 349
Kroupa P., Tout C. A., Gilmore G., 1993, MNRAS, 262, 545
Lanzoni B., Guiderdoni B., Mamon G. A., Devriendt J., Hatton S., 2005, MNRAS, 361, 369
Larson R. B., Tinsley B. M., Caldwell C. N., 1980, ApJ, 237, 692
Laurikainen E., Salo H., Buta R., Knapen J. H., 2007, MNRAS, 381, 401
Laurikainen E., Salo H., Buta R., Knapen J. H., 2009, ApJ, 692, L34
Laurikainen E., Salo H., Buta R., Knapen J. H., Comerón S., 2010, MNRAS, 405, 1089
Li C., White S. D. M., 2009, MNRAS, 398, 2177
Lin L. et al., 2004, ApJ, 617, L9
Łokas E. L., Mamon G. A., 2003, MNRAS, 343, 401
Lucy L. B., 1974, AJ, 79, 745
Maltby D. T. et al., 2012, MNRAS, 419, 669
Marinova I. et al., 2012, ApJ, 746, 136
Martinez-Valpuesta I., Shlosman I., Heller C., 2006, ApJ, 637, 214
Matthews L. D., Gallagher J. S., III, 1997, AJ, 114, 1899
McDonald M., Courteau S., Tully R. B., 2009, MNRAS, 394, 2022
Melnick J., Hoessel J., White S. D. M., 1977, MNRAS, 180, 207
Mihos J. C., Harding P., Feldmeier J., Morrison H., 2005, ApJ, 631, L41
Mihos J. C., Janowiecki S., Feldmeier J. J., Harding P., Morrison H., 2009, ApJ, 698, 1879
Mobasher B. et al., 2001, ApJS, 137, 279
Moore B., Katz N., Lake G., Dressler A., Oemler A., 1996, Nature, 379, 613
Moore B., Lake G., Katz N., 1998, ApJ, 495, 139
Moore B., Lake G., Quinn T., Stadel J., 1999, MNRAS, 304, 465
Naab T., Johansson P. H., Ostriker J. P., 2009, ApJ, 699, L178
Naab T., Trujillo I., 2006, MNRAS, 369, 625
Naab T., Khochfar S., Burkert A., 2006, ApJ, 636, L81
Neistein E., Weinmann S. M., 2010, MNRAS, 405, 2717
Okamoto T., Nagashima M., 2003, ApJ, 587, 500
Oser L., Naab T., Ostriker J. P., Johansson P. H., 2012, ApJ, 744, 63
Ostriker J. P., Tremaine S. D., 1975, ApJ, 202, L113
Padmanabhan N. et al., 2008, ApJ, 674, 1217
Peng C. Y., Ho L. C., Impey C. D., Rix H.-W., 2002, AJ, 124, 266
Pfenniger D., Norman C., 1990, ApJ, 363, 391
Poggianti B. M. et al., 2001, ApJ, 563, 118
Poggianti B. M. et al., 2009, ApJ, 697, L137
Pohlen M., Trujillo I., 2006, A&A, 454, 759
Pohlen M., Dettmar R.-J., Lütticke R., Aronica G., 2002, A&A, 392, 807
Price J. et al., 2009, MNRAS, 397, 1816
Quilis V., Moore B., Bower R., 2000, Science, 288, 1617
Ravindranath S., Ho L. C., Peng C. Y., Filippenko A. V., Sargent W. L. W., 2001, AJ, 122, 653
Ravindranath S. et al., 2004, ApJ, 604, L9
Rawle T. D., Lucey J. R., Smith R. J., Head J. T. C. G., 2013, MNRAS, 433, 2667
Richardson W. H., 1972, J. Opt. Soc. Am., 62, 55
Robaina A. R., Bell E. F., van der Wel A., Somerville R. S., Skelton R. E., McIntosh D. H., Meisenheimer K., Wolf C., 2010, ApJ, 719, 844
Robertson B., Cox T. J., Hernquist L., Franx M., Hopkins P. F., Martini P., Springel V., 2006, ApJ, 641, 21
Schneider P., ed., 2006, Extragalactic Astronomy and Cosmology. Springer, Berlin
Sérsic J. L., 1968, Observatorio Astronomico. Univ. de Cordoba, Cordoba
Smith R. J. et al., 2010, MNRAS, 408, 1417
Springel V. et al., 2005, Nature, 435, 629
Steinmetz M., Navarro J. F., 2002, New Astron., 7, 155
The L. S., White S. D. M., 1986, AJ, 92, 1248
Thuan T. X., Kormendy J., 1977, PASP, 89, 466
Tonnesen S., Bryan G. L., 2008, ApJ, 684, L9
Tonnesen S., Bryan G. L., 2009, ApJ, 694, 789
Tonnesen S., Bryan G. L., 2010, ApJ, 709, 1203
Toomre A., 1977, in Tinsley B. M., Larson R. B. G., Campbell D., eds, Evolution of Galaxies and Stellar Populations. Yale Univ. Observatory, New Haven, p. 401
Trager S. C., Faber S. M., Dressler A., 2008, MNRAS, 386, 715
Trentham N., Mobasher B., 1998, MNRAS, 293, 53
Trentham N., Tully R. B., 2002, MNRAS, 335, 712
Trujillo I., Erwin P., Asensio Ramos A., Graham A. W., 2004, AJ, 127, 1917
van der Kruit P. C., 1979, A&AS, 38, 15
van der Kruit P. C., Searle L., 1981a, A&A, 95, 105
van der Kruit P. C., Searle L., 1981b, A&A, 95, 116
van der Wel A. et al., 2011, ApJ, 730, 38
Wang L., Weinmann S. M., Neistein E., 2012, MNRAS, 421, 3450
Weinmann S. M., van den Bosch F. C., Yang X., Mo H. J., Croton D. J., Moore B., 2006, MNRAS, 372, 1161
Weinzirl T., Jogee S., Khochfar S., Burkert A., Kormendy J., 2009, ApJ, 696, 411
Weinzirl T. et al., 2011, ApJ, 743, 87
Yagi M., Komiyama Y., Yoshida M., Furusawa H., Kashikawa N., Koyama Y., Okamura S., 2007, ApJ, 660, 1209
Yagi M. et al., 2010, AJ, 140, 1814
Yoshida M. et al., 2008, ApJ, 688, 918
Zibetti S., White S. D. M., Schneider D. P., Brinkmann J., 2005, MNRAS, 358, 949

APPENDIX A: USING GALFIT

The proper operation of GALFIT depends on certain critical inputs. We briefly describe below how these important inputs are handled.

(i) *PSF.* Accurate modelling of the PSF is essential in deriving galaxy structural properties. GALFIT convolves the provided PSF with the galaxy model in each iteration before calculating the χ^2. Because the PSF varies with position across the ACS Wide Field Camera chips, it is ideal to separately model the PSF for each galaxy position. We use the grid of model ACS PSFs in the *F*475*W* and *F*814*W* filters from Hoyos et al. (2011). This grid of PSFs was created with TINYTIM (Krist 1995) and DRIZZLYTIM.[6]

For a given set of multidrizzle parameters, DRIZZLYTIM transforms $x - y$ coordinates in the final science frames back to the system of individually distorted flat-fielded (FLT) images. DRIZZLYTIM invokes TINYTIM to create a PSF with the specified parameters (e.g. position and filter) and then places the PSF at the appropriate position in blank FLT frames. The FLT frames are passed through MULTIDRIZZLE with the same parameters as the science images. Finally, a Charge Diffusion Kernel is applied to the PSFs in the geometrically distorted images. The grid of ACS PSFs from Hoyos et al. (2011) models a PSF for every 150 pixels in the *x*- and *y*-directions.

[6] DRIZZLYTIM is written by Luc Simard.

For each galaxy in our sample we select the model PSF closest in proximity to the galaxy.

(ii) *Sigma images.* A sigma image is the 2D map of the 1σ standard deviations in pixel counts of the input image. GALFIT uses the sigma image as the relative weight of pixels for calculating the goodness of fit. Achieving a reduced $\chi^2 \sim 1$ with a successful model fit requires that the sigma image be correct. A sigma image can either be provided, or GALFIT can be allowed to calculate one based on the properties of the data image (image units of counts or counts per second, effective gain, read noise, number of combined exposures). We choose the latter option and allow GALFIT to calculate the sigma images.

(iii) *Background subtraction.* While it is possible for GALFIT to freely fit the background sky, this is not recommended (Peng et al. 2002). In a multiple-component fit to a galaxy with at least two components, freely fitting the sky can exaggerate or suppress the wings of the central Sérsic profile and incorrectly measure the bulge half-light radius and Sérsic index. To avoid this, for each galaxy the background sky is measured and held fixed during the fit. The sky background is based on ellipse fitting with the IRAF/`ELLIPSE` task. Ellipses are fit to the galaxy and the surrounding area, with the ellipses in the surrounding area being fixed to the shape and orientation of the galaxy. The gradient along the semimajor axis is calculated, and the sky is estimated as the mean of elliptical annuli over a span in semimajor axis where the gradient reaches a prescribed small value. In each case, the area fitted by the ellipses exceeds the area subtended by the galaxy. Visual inspection of the ellipse fits shows that the perceived flat gradient corresponds to empty sky and not an extended galaxy outer profile with a very small gradient.

(iv) *Image thumbnails and masks.* Thumbnail cutouts of the intermediate-mass galaxies are made to lessen the computational time for fitting. Following Hoyos et al. (2011), square image thumbnails centred on the target galaxy are made using the output from SExtractor. Image size in pixels is determined with

$$\text{size} = 4 \times \text{A\_IMAGE} \times \text{KRON\_RADIUS}. \quad \text{(A1)}$$

The image units are transformed from counts per second to counts by multiplying by the exposure time. Image masks are based on the segmentation images provided from SExtractor. The segmentation images are modified to unmask the background and target galaxy being fitted. Any bright sources that visibly overlap with the target galaxy are also unmasked so that overlapping sources can be fitted simultaneously. Masks for relatively bright sources that do not overlap with the galaxy being fitted are expanded in semimajor axis by a factor of 1.5. We visually check by blinking the data image and modified segmentation image to verify that the unmasked region encompasses all of the target galaxy, including those with large diffuse haloes that SExtractor does not capture (Hoyos et al. 2011).

APPENDIX B: DETAILS OF STRUCTURAL DECOMPOSITION

This appendix contains the full details concerning the structural decomposition scheme outlined in Section 3.2.

B1 Single Sérsic fits

We first fit all galaxies with a single Sérsic profile before attempting the multicomponent fits. This step is useful for measuring the total luminosity of a galaxy as well as measuring the centroid (Weinzirl et al. 2009). The Sérsic profile has seven free parameters: centroid, luminosity, half-light radius r_e, Sérsic index n, axis ratio, position angle, and disciness/boxiness. We fix the disciness/boxiness so that the fitted structures are perfect ellipses. We estimate the other six parameters based on the parameters in SExtractor and allow them to optimize in the fit. The detailed image preparation and inputs for the proper operation of GALFIT are described in Appendix A.

Fig. B1 compares our results for the single Sérsic fits (with no point source) with those of Hoyos et al. (2011), who also perform single Sérsic fits with GALFIT and GIM2D using Coma ACS Treasury Survey data. Note that the galaxies in our sample requiring one Sérsic profile are distinguished in Fig. B1. With the exception of COMAi125935.698p275733.36 (NGC 4874), our results for these sources requiring one Sérsic profile well match those derived by Hoyos et al. (2011). For NGC 4874, we measure the r_e and n of NGC 4874 to be 17.3 kpc and 3.05, respectively, while Hoyos et al. (2011) measure r_e and n to be 3.2 kpc and 1.3.

For sources requiring more than one Sérsic profile, our single Sérsic magnitudes agree well in general with those of Hoyos et al. (2011), except for one case (COMAi13051.149p28249.90) where Hoyos et al. (2011) underestimate the magnitude by $\sim$5.5 mag. There are also outliers in both r_e and n. In 10 (5) instances (including COMAi13051.149p28249.90), the difference in r_e (n) exceeds a factor of 1.5.

There are two key differences in our fitting methodology (see Appendix A) compared with Hoyos et al. (2011). Most importantly, we entirely unmask the target galaxy and background in the segmentation-based masks so that GALFIT fits to pixels beyond what SExtractor associates with each galaxy. Hoyos et al. (2011) confine a galaxy to a customized mask generated based on the output of SExtractor. This approach misses a finite fraction of the flux in the target galaxy. This may explain why in Fig. B1 we measure brighter magnitudes and larger r_e for more extended galaxies, where SExtractor does not detect all of the light in the galaxy. Secondly, we measure and fix the background sky while Hoyos et al. (2011) keep the sky as a free parameter. Allowing the sky background to freely vary in our fits fails to account for most of the scatter between our results and those of Hoyos et al. (2011). Rather, the disagreement appears to mainly be the result of differences in image masking.

B2 Multicomponent fits

For the Stage 2 Sérsic + Sérsic fits, we model the 'inner' and 'outer' components (C1 and C2) with Sérsic profiles that can represent physically different components (see Section 3.2).

Sensible initial guess parameters for Stage 2 are determined from a combination of the data image, Stage 1 model, and Stage 1 residuals. Guesses for the inner Sérsic component (C1) are usually based on the Stage 1 model. The centroid of the Sérsic components (and nuclear point source if present) are fixed to the best-fitting centroid from the single Sérsic model. During the fits, we allow all other parameters (luminosity, r_e, n, axis ratio, and position angle) to vary for the inner and outer components without a priori fixing the nature of these components.

With one exception, the χ^2 in Stage 2 is always lower compared with χ^2 in Stage 1 due to the extra Sérsic component. While the rare increase in χ^2 from Stage 1 to Stage 2 is an indication that the latter model is not reliable, the almost universal decrease in χ^2 is not necessarily a sign that the Stage 2 fit is meaningful because, in

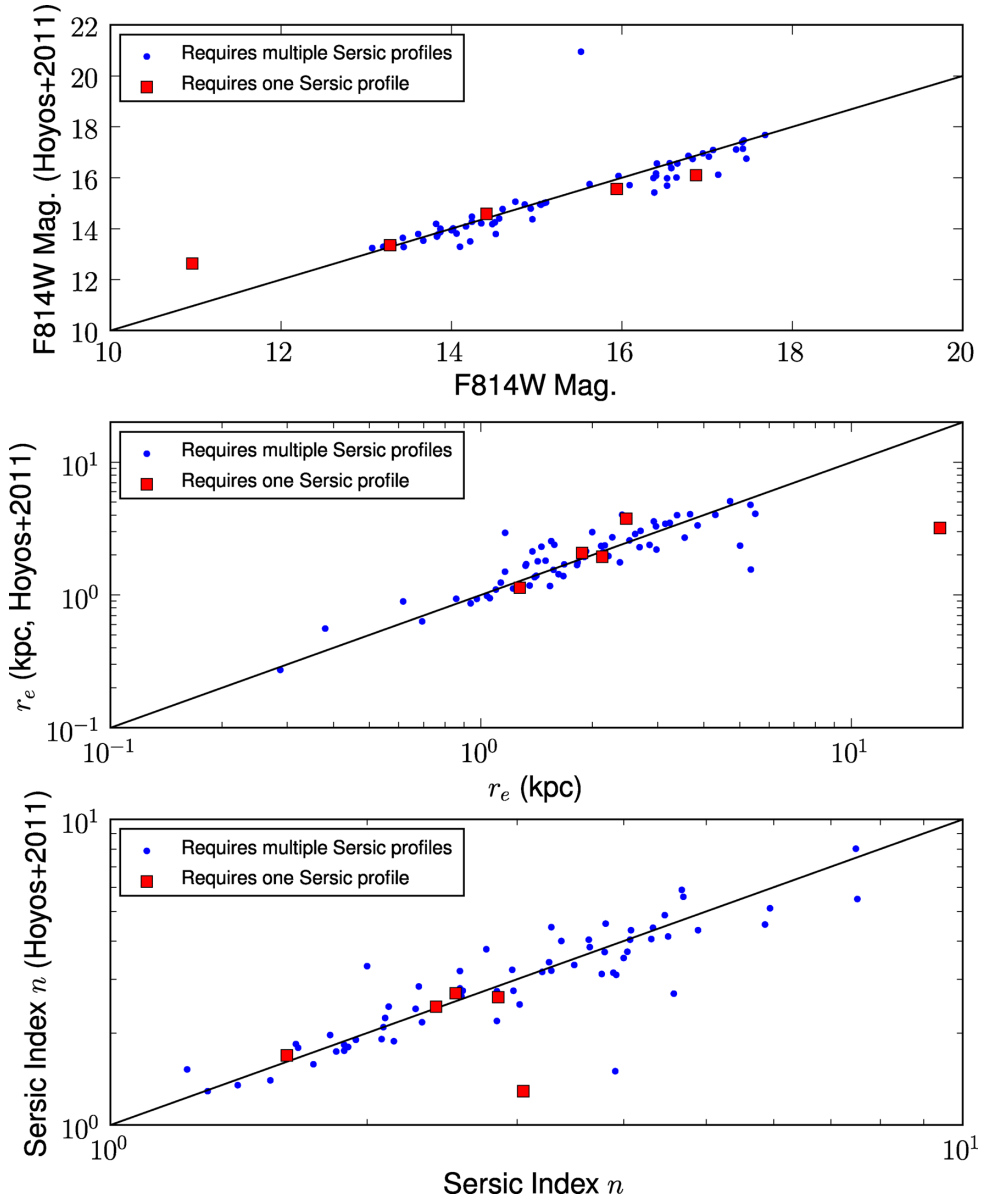

Figure B1. Compares our results for the single Sérsic fits (with no points source) with those obtained by Hoyos et al. (2011) using GALFIT on the same data. The sources in our sample requiring one Sérsic component are labelled separately from sources requiring two or three Sérsic profiles. Our derived magnitudes, r_e, and n for the sources requiring one Sérsic profile agree well with the parameters from Hoyos et al. (2011), with the one exception being cD galaxy NGC 4874 (COMAi125935.698p275733.36) with $n \sim 3$. Note that cD galaxy NGC 4889 requires only one Sérsic profile but it is not included here as it is not in the Hoyos et al. (2011) sample. See Appendix B1 for additional details.

principle, such a decrease in χ^2 could be driven by the extra free model parameters. We consider a Stage 2 multicomponent model to be superior to the Stage 1 fit if (i) χ^2 drops, (ii) the Stage 2 model parameters are well behaved (i.e. not unphysically large or small), and (iii) the Stage 2 residuals are deemed by visual inspection to show a reduction in coherent structure relative to the Stage 1 residuals.

Fig. B2 provides examples where a single Sérsic model fails to model the entire galaxy well and leaves behind coherent structure in the residuals. Such coherent structure is indicative of additional components such as compact central structures, rings, annuli, and extended components, and bars/ovals. We illustrate in Figs B3 and B4 how some of these examples are best fitted by models with multiple Sérsic components.

If a galaxy does not require a Stage 2 model, or if the Stage 2 model fails to meet the above criteria, then the galaxy is described by a single Sérsic profile + point source, if present. Six galaxies are best represented by Stage 1. Two (COMAi13017.683p275718.93 and COMAi13018.093p275723.59) cannot be fitted with multiple Sérsic models because they are interacting. In the third case, (COMAi125931.103p275718.12), the χ^2 increases from Stage 1 to Stage 2. The final three cases (NGC 4874, NGC 4889, and COMAi125909.468p28227.35) show evidence of a core (see Appendix C).

Galaxies for which the Stage 2 model is deemed an improvement are interpreted as follows. Since the outer component C2 could represent a disc, we must specify criteria for identifying an outer disc. The outer component C2 is a disc if it satisfies at least one

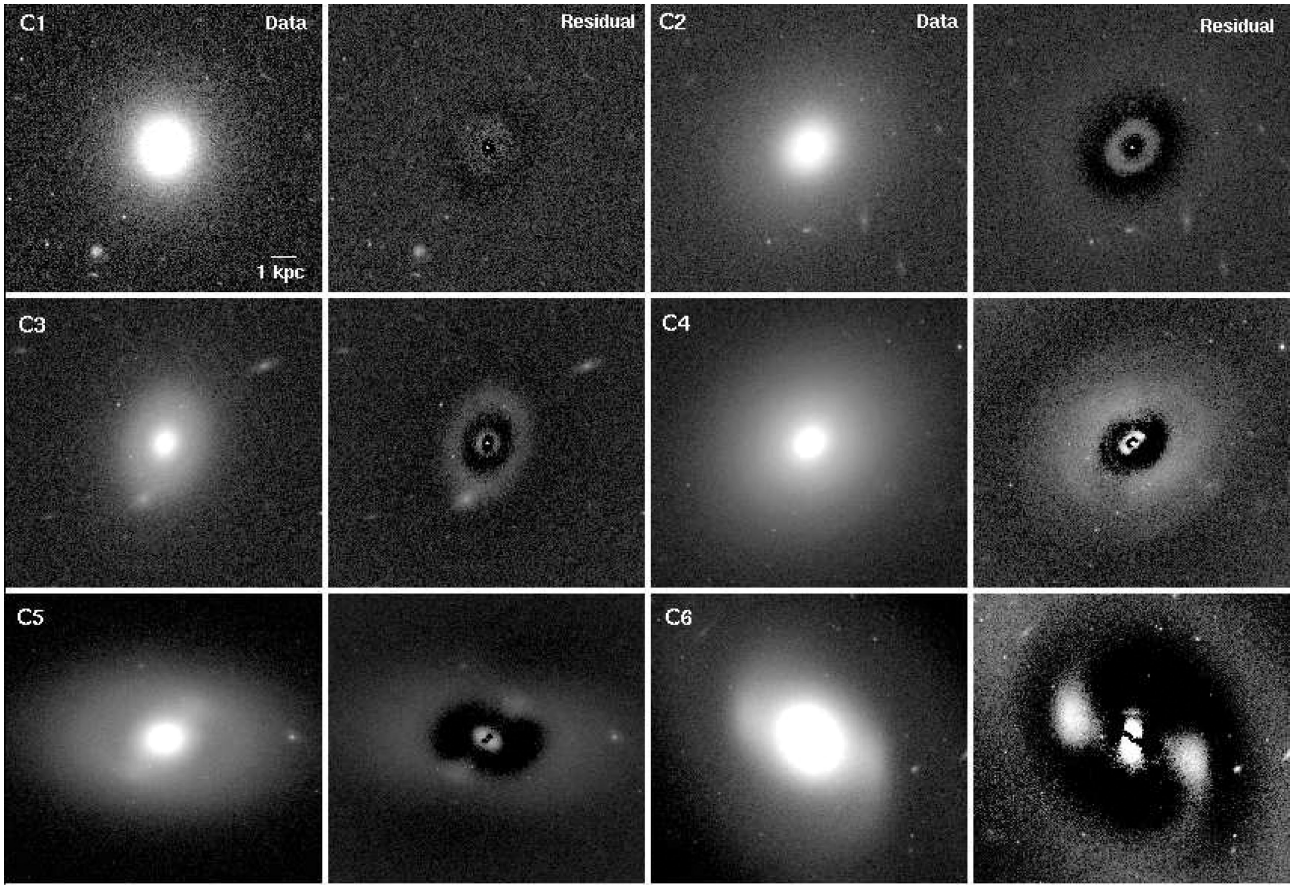

Figure B2. Shows examples C1 to C6 where a single Sérsic model (plus point source if needed) does not provide a good fit to coherent galaxy structure that is best modelled with one or more additional Sérsic profiles. Such residual structure includes central compact structures (C2, C3, C4, C5, C6), rings (C3, C4), annuli and extended components (C1, C4), and bars/ovals (C5, C6). These systems are better fitted by models with multiple Sérsic components (see Figs B3 and B4). Columns 1 and 3 show the input *I*-band images. Columns 2 and 4 show the residuals after subtracting the best single Sérsic fit. Note C1=COMAi125931.893p275140.76, C2=COMAi125935.286p275149.13, C3=COMAi13021.673p275354.81, C4=COMAi13014.746p28228.69, C5=COMAi13027.966p275721.56, and C6=COMAi125930.824p275303.05.

of the following. (i) The galaxy is highly inclined such that C2 has a low axis ratio $b/a \leq 0.25$ that is below the axis ratios found for ellipticals. (ii) The galaxy is moderately inclined and C2 shows disc signatures (e.g. bars, rings, or spiral arms) in the data images and/or Stage 2 residuals. (iii) For moderately inclined galaxies without disc features that do not satisfy (i) or (ii), we require Sérsic n be less than the threshold value $n_{\rm disc\_max}$.

Theoretical considerations show that pure discs have $n = 1$, suggesting the threshold should be $n \sim 1$. However, real galaxy discs are not fitted perfectly by Sérsic profiles. We determine the value empirically from the maximum disc Sérsic index in galaxies satisfying (i) and (ii). Highly inclined discs show a range in Sérsic index of 0.48–0.86. Moderately inclined galaxies identified as having spiral arms but no bar have outer discs with Sérsic index 0.63–1.20. Note that some of the highly inclined galaxies could be barred, and this may account for the small difference in average Sérsic index between the highly inclined and moderately inclined barred galaxies.

In order to accurately model the outer disc of moderately inclined barred galaxies, a triple Sérsic profile (see below) is required. After taking this extra step, the outer disc Sérsic index among moderately inclined barred galaxies is 0.25–1.66. The maximum Sérsic index among outer discs in galaxies satisfying requirement (i) and (ii) is 1.66, and we therefore set $n_{\rm disc\_max}$ to this value. Thus, outer discs span the range 0.25–1.66 in Sérsic index and have a median n of 0.84. Fig. B5 shows the galaxy (COMAi125950.105p275529.44) on which we base our measurement of $n_{\rm disc\_max}$. Appendix D discusses the uncertainties in the adopted value of $n_{\rm disc\_max}$.

Galaxies that satisfy any of the requirements (i), (ii), or (iii) are deemed to have an outer disc. Galaxies without an outer disc are considered photometric ellipticals.

We test all galaxies having an outer disc for the presence of a large-scale bar/oval in Stage 3 by fitting a triple Sérsic profile + point source, if present. Bars/ovals are modelled with an elongated, low Sérsic index ($n \sim 0.5$) profile (Peng et al. 2002; Weinzirl et al. 2009). In the text, we do not distinguish between bars and ovals, and we use 'bar' to describe both.

The initial guesses for the three-component models come from the best Stage 2 model combined with visual inspection. The Sérsic index for the bar is initially guessed to be 0.5, and the shape and position angle of the bar are visually estimated using the data image or the residuals of the Stage 2 fit. When selecting between the Stage 2 and Stage 3 fits, we applied the same constraints described above for the behaviour of χ^2. An additional complication is that in galaxies with unbarred outer discs, GALFIT may fit a 'bar' to any existing spiral arms, rings, or clumpy disc structure. Stage 3 fits in these cases could be discarded by noting the resulting discrepancies in appearance between the galaxy images and the Stage 3 model

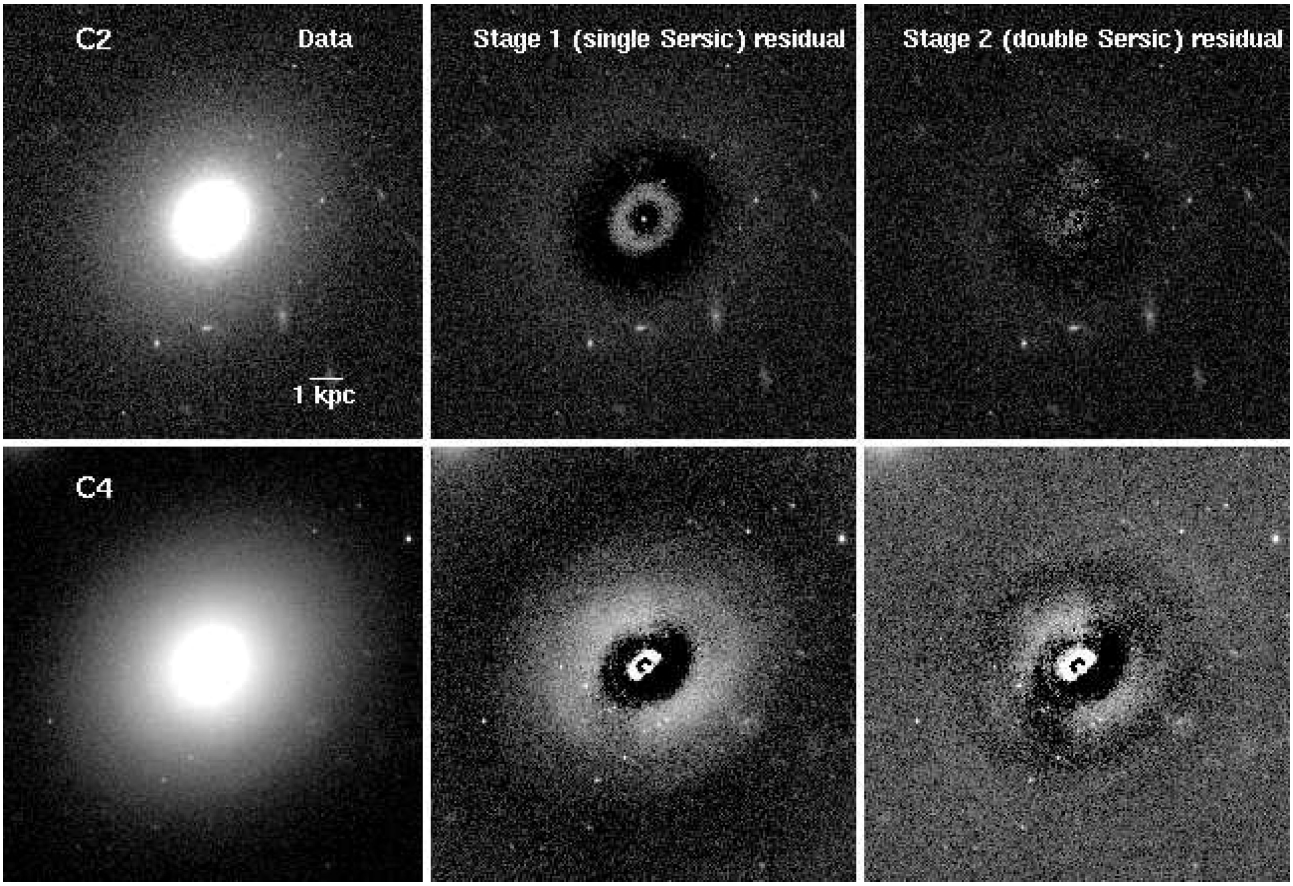

Figure B3. Shows how some of the galaxies (C2=COMAi125935.286p275149.13 and C4=COMAi13014.746p28228.69) poorly fitted by a single Sérsic model (plus point source if needed) in Stage 1 can be better fitted by two Sérsic models (plus point source if needed) in Stage 2. Each row shows the data, residual after Stage 1, and the residual after Stage 2. Galaxy C2 is best fitted as having an inner disc ($n = 0.31$) and an outer elliptical structure ($n = 2.08$). Galaxy C4 is best fitted with an inner bulge $n = 3.68$ and an outer disc ($n = 0.47$).

images. Fig. B4 shows examples of two disc galaxies where adding the third Sérsic component removes the bar signature from the residuals.

B3 Nuclear point sources

Nuclear point sources are found in galaxies of all Hubble types. The frequency of nuclear point sources is very sample dependent and is particularly sensitive to range of galaxy luminosity. *HST* studies of early-type galaxies (e.g. Ravindranath et al. 2001; Côté et al. 2006) have measured nucleation rates of 50 per cent or more. Ravindranath et al. (2001) find that about half of early-type (E, S0, S0/a) galaxies have nuclear point sources. Côté et al. (2006) show that the frequency of nucleation in ACS images of the Virgo cluster is at least 66 per cent in galaxies with $M_B \leq -15$. Graham & Guzmán (2003) discuss 13/15 examples of dwarf ellipticals in the Coma cluster showing evidence for nucleation. Balcells, Graham & Peletier (2007a) measure a frequency of 58 per cent for S0 to Sbc galaxies. Böker et al. (2002) measure the frequency of point sources to be 75 per cent in spirals with Hubble types Scd to Sm.

Although nuclear point sources account for a small percentage (<1 per cent) of a galaxy's light, it is important to include them during multicomponent structural decomposition. Neglecting nuclear point sources can have a significant effect on derived parameters of bulges (Balcells et al. 2003; Weinzirl et al. 2009). We assess the presence of nuclear point sources with visual inspection. If a compact light source is visible by eye in the residuals of the single Sérsic fit, the galaxy is flagged as having a potential point source. With this procedure, 49/69 galaxies in sample S2 have a potential nuclear point source.

Galaxies having a potential nuclear point source are fitted with an extra nuclear point source component in the best-fitting single or multicomponent model. GALFIT models the point source with the user-input PSF. More than half (38/69, 55.1 ± 6.0 per cent) of objects in sample S2 have a nuclear point source in the final, best-fitting structural decomposition. Fig. B6 shows examples of residual galaxy images with point sources.

Fig. B7 shows that the derived point source luminosities correlate with total galaxy magnitude such that more luminous point sources are found in brighter galaxies. Similar results have been found in earlier work (e.g. Graham & Guzmán 2003; Balcells et al. 2007a).

B4 cD galaxies

cD galaxies are defined by having extra light on cluster-sized (∼1 Mpc) scales with respect to the outward extrapolation of the Sérsic profile fit to the inner (∼100 kpc) portion of the galaxy. Such galaxies are luminous and are found in regions of high galaxy number density (Binney & Merrifield 1998). Of the three cD galaxies in Coma, two (NGC 4874 and NGC 4889) lie in the projected central

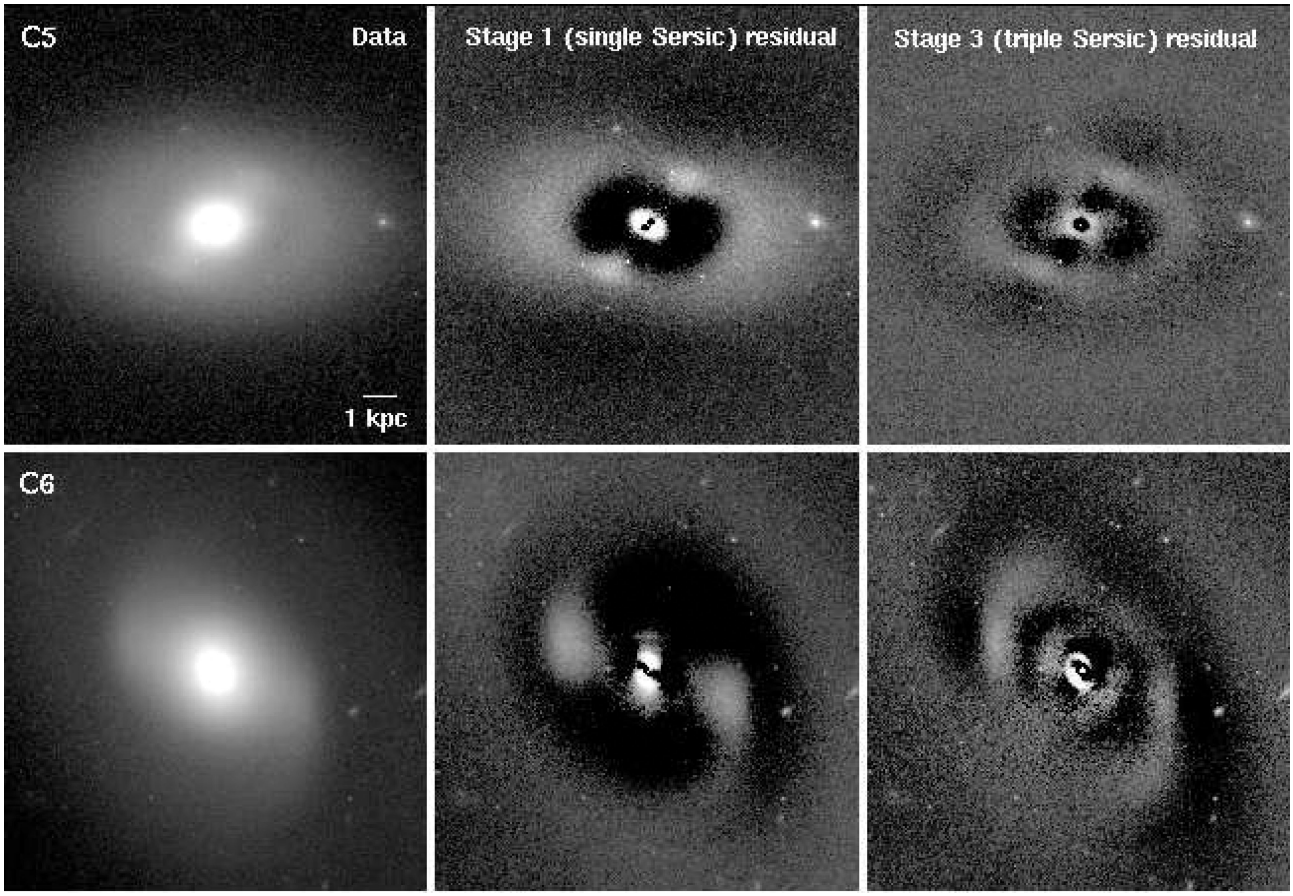

Figure B4. Shows two examples of barred galaxies (C5=COMAi13027.966p275721.56 and C6=COMAi125930.824p275303.05) poorly fitted by a Stage 1 single Sérsic model that are better fitted by a Stage 3 triple Sérsic (plus point source if needed) model. Column 1 shows the data images while columns 2 and 3 show the residuals after the Stage 1 and Stage 3 model, respectively.

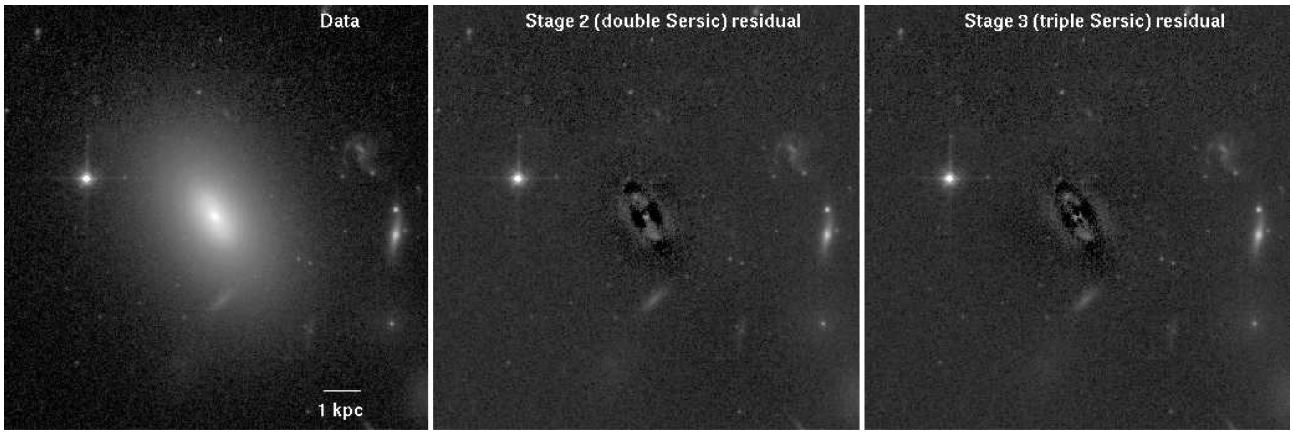

Figure B5. Shows the decomposition of moderately inclined, barred galaxy COMAi125950.105p275529.44, in which we measure the highest outer disc Sérsic index $n = 1.66$. Thus, this galaxy sets the empirically determined upper limit on disc Sérsic index, $n_{\rm disc\_max} = 1.66$. Column 1 shows the data images while columns 2 and 3 show the residuals for the Stage 2 and Stage 3 model, respectively. The bar signature is clearly present in the residuals.

0.5 Mpc and are therefore in our sample. The third cD (NGC 4839) lies in the outer southwest region of Coma and is not part of this study.

Definitive proof that NGC 4874 and NGC 4889 are cDs is the detection of intracluster light in Coma (Kormendy & Bahcall 1974; Melnick et al. 1977; Thuan & Kormendy 1977; Bernstein et al. 1995; Adami et al. 2005; Arnaboldi 2011).

The single Sérsic indices reported in Appendix B and Table 3 for the these cD galaxies are $n \sim 3{-}4.4$ because the decompositions also include the central core. The central core is a clear deviation from the inward extrapolation of the Sérsic profile that characterizes the outer galaxy structure. For this reason, masking the core regions (i.e. the central $\sim$2 arcsec) is more physically motivated and would yield higher single Sérsic indices $n \gtrsim 8$. This is demonstrated in

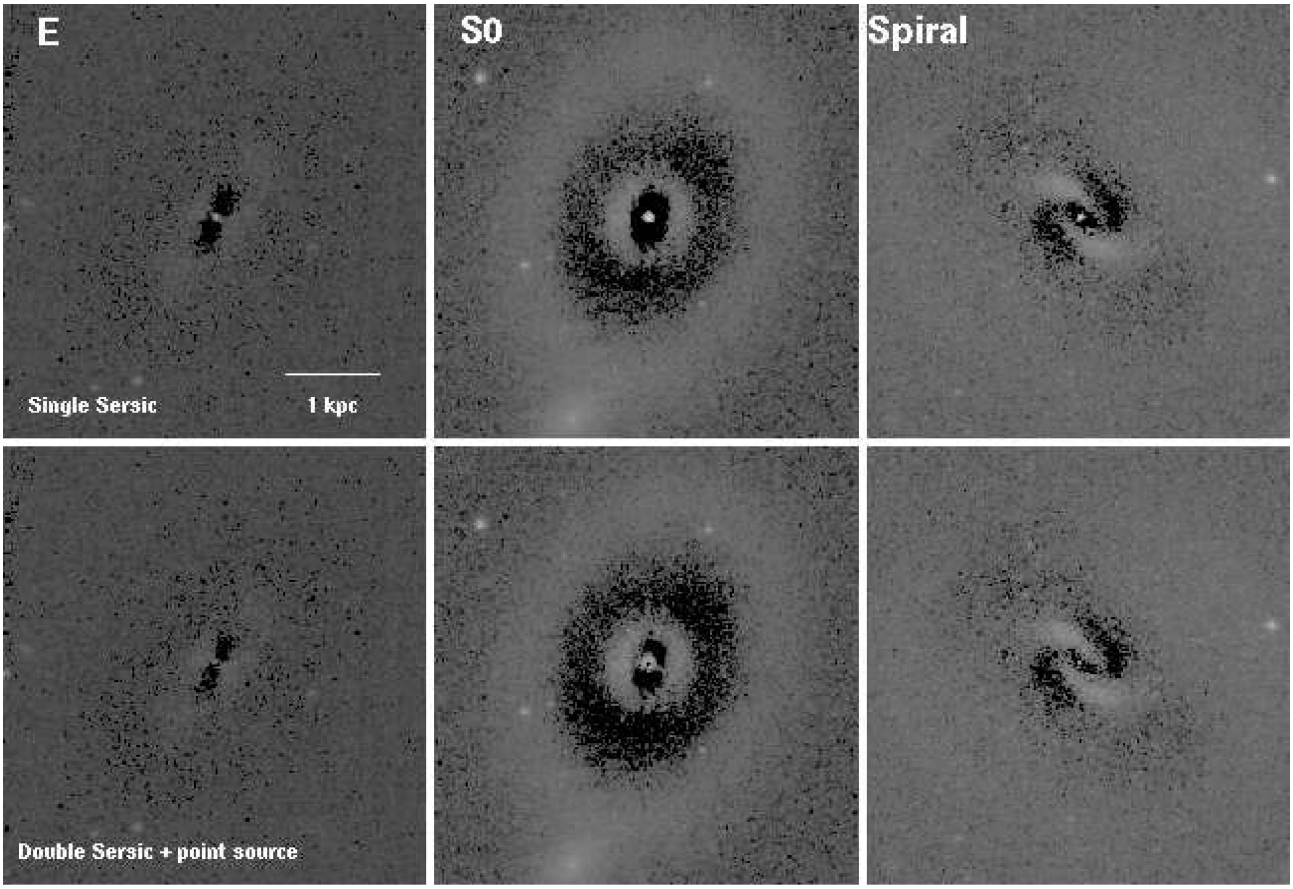

Figure B6. Compares residuals after fitting a single Sérsic model (top row) versus the best-fitting double Sérsic + nuclear point source model (bottom row) for an elliptical (COMAi13030.954p28630.22), S0 (COMAi13021.673p275354.81), and spiral (COMAi13041.193p28242.34). The nuclear point source is visible in the residuals in the top row.

Appendix C and Table 2. We note that both approaches (masking or not masking the core during the 2D decomposition) lead us to the same conclusion that all of the cD light is associated with structures of $n \gg n_{\rm disc\_max}$ (Appendix C). Note in Table 5 we list the cD galaxies and the structure parameters from the 2D decomposition where the core is masked.

The high $n \gg n_{\rm disc\_max}$ values in the cD galaxies are due to the extended wings in the Sérsic profile resulting from the extended low surface brightness envelope of the cD. This extended envelope is likely made up of intracluster light and the cumulative debris from galaxies, consistent with the view that cD galaxies arise from repeated bouts of galactic cannibalism and tidal stripping of satellite galaxies in a cluster (Ostriker & Tremaine 1975; Aragon-Salamanca, Baugh & Kauffmann 1998; De Lucia & Blaizot 2007).

B5 Cosmic variance

The Coma ACS data only cover 19.7 per cent of the projected central 0.5 Mpc radius of Coma. The relative fractional numbers of E+S0:spiral, or specifically the ratio of E/S0s, we derive from this data may not be representative of the full region in the projected central 0.5 Mpc radius of Coma due to the incomplete sampling and cosmic variance. In order to assess the effect of incomplete sampling and cosmic variance on our results, we perform the following test.

First, we define the region covered by ACS in the projected central 0.5 Mpc radius of Coma as $R1$, and the full area in the projected central 0.5 Mpc radius of Coma as $R2$. We use the Hubble MT from the GOLD Mine data base[7] (Gavazzi et al. 2003) to compute the fraction of E+S0:spiral galaxies in region $R1$ and $R2$ with $M_\star \geq 4.4 \times 10^9$ M$_\odot$, the mass limit of the Coma GOLD Mine sample. The MT reported by GOLD Mine are sourced from the literature. If we take the visual MT from GOLD Mine at face value then we draw the following conclusions.

(i) The effect cosmic variance causes the ratio of E/S0 within the GOLD Mine MT to vary by a factor of 1.11 between region $R1$ and $R2$ for $M_\star \geq 4.4 \times 10^9$ M$_\odot$.

(ii) The partial ACS coverage of the projected central 0.5 Mpc and associated cosmic variance thus causes our study based on region $R1$ to

(a) overestimate the ratio of S0/E in the ACS sample for $M_\star \geq 4.4 \times 10^9$ M$_\odot$ by a factor of 1.4 and

(b) overestimate the fraction $f_{\rm cold}$ of dynamically cold stellar mass (43 per cent) by a factor of 1.27 (Section 5.6) for $M_\star \geq 10^9$ M$_\odot$. We note that the overestimation of $f_{\rm cold}$ is not by the same factor as in (a) because S0s have a significant fraction of their mass in dynamically hot bulges.

(iii) Currently, our conclusion in Section 5.6, based on region $R1$ is that the hierarchical models are overpredicting the empirical

[7] http://goldmine.mib.infn.it/

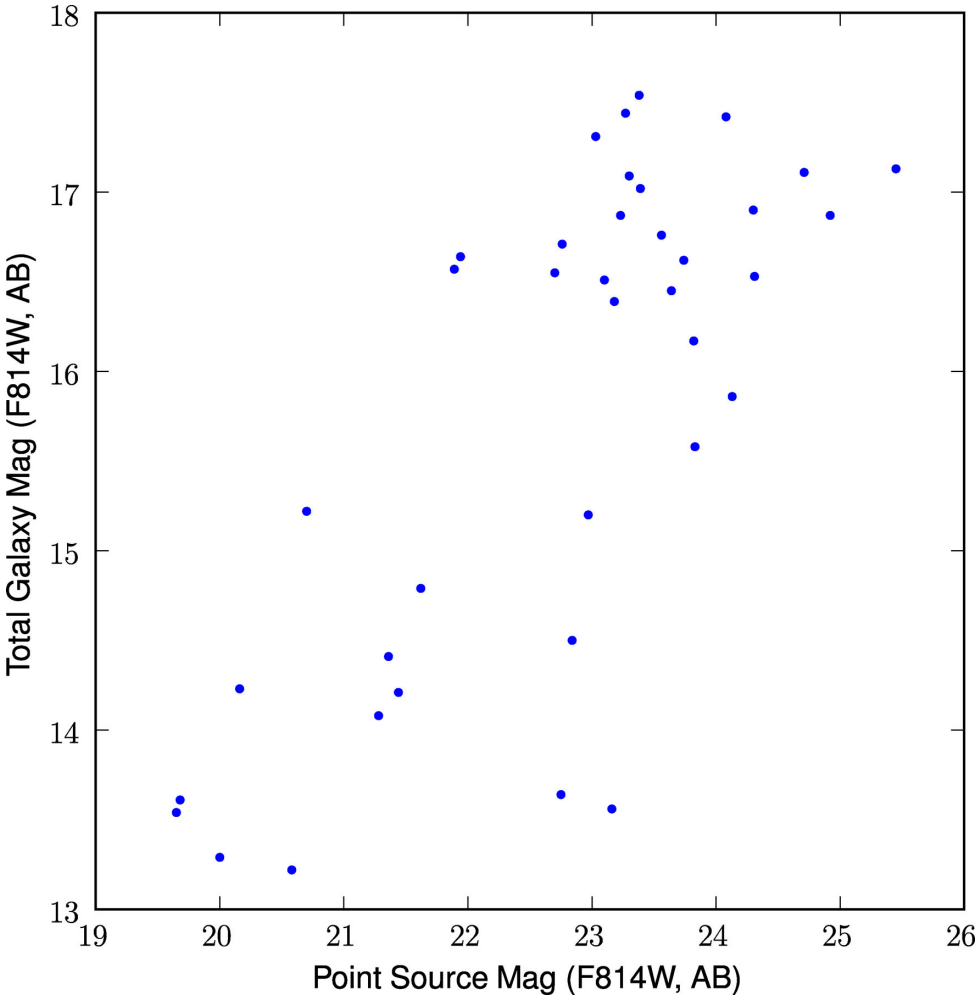

Figure B7. Shows the relation between total galaxy luminosity and point source luminosity for objects having a nuclear point source in the final, best structural decomposition.

fraction $f_{\rm cold}$. It is clear from (ii) (b), that correcting for partial ACS coverage and cosmic variance would only strengthen this conclusion further.

B6 Galaxy colour gradients

In Section 4.2 we suggest that galaxy colour gradients should not bias our conclusions concerning the distribution of dynamically hot and cold stellar mass. Here, we explicitly test this idea.

For a subset of 10 galaxies spanning types G3 to G5 and matching the morphology distribution of the mass-selected sample (E+S0:spiral = 2+7:1) in Table 6, we re-evaluated the fractional mass in hot and cold components based on combining structural decompositions of both the *F*814*W* and *F*475*W* images. The new *F*475*W*-band decompositions were performed identically to the existing *F*814*W* decompositions, except that the position angle and axis ratio of the galaxy structures were fixed to their values from the *F*814*W*-band decompositions. Stellar masses of the structural components were calculated according to Into & Portinari (2013) after converting the $F475W - F814W$ colour and the *F*814*W* luminosity into a $B - I$ colour and *I*-band luminosity, respectively, using the procedure in Section 2.2.

In the new *F*475*W* decompositions for this subset of galaxies, the half-light radii and Sérsic n are similar to the corresponding values in the *F*814*W* band. The average offset is 5.4 per cent with a standard deviation of 5.6 per cent. Furthermore, the fractional hot stellar mass inferred from a constant global *F*814*W* M/L ratio is 53.4 per cent. After calculating the stellar mass of each galaxy component from the $B - I$ colour, the fractional hot stellar mass is found to be 50.5 per cent. Thus, M/L gradients within a galaxy do not appear to have a significant effect on the fractional masses measured in cold versus hot components.

APPENDIX C: IDENTIFYING CORE ELLIPTICALS

While elliptical galaxies are remarkably well fitted by Sérsic profiles over large dynamic ranges, giant elliptical galaxies contain cores, or 'missing light' at small radii that constitute a downward deviation from the inward extrapolation of the outer Sérsic profile (Graham et al. 2003; Trujillo et al. 2004; Kormendy et al. 2009). Such cores are hypothesized to form from scouring induced by binary black holes during dry, dissipationless mergers.

Because cores, which have traditionally been identified with 1D radial light profiles, are not an obvious feature of the galaxy's 2D light distribution, global Sérsic fits will encompass any existing core. This is potentially problematic for at least two reasons. Including the core in the Sérsic fit will lower the global Sérsic

index. This is of concern in this paper where the Sérsic index plays a key role in interpreting galaxy structure (Section 3.1). Secondly, fitting the core region may produce features in the residuals that prompt addition of extra nuclear components that have no physical justification.

We systematically search for cores in all sample galaxies. For this task, we use 1D light profiles generated from ellipse fitting of deconvolved images. The ACS images were deconvolved using a simulated PSF (Appendix A for details) and 40 iterations of Lucy–Richardson deconvolution with the IRAF task LUCY (Lucy 1974; Richardson 1972). Our approach uses the criteria for identifying core galaxies from Trujillo et al. (2004) by fitting Sérsic and core-Sérsic profiles (Graham et al. 2003) to the 1D light profiles.

For simplicity, we use the version of the core-Sérsic profile that assumes an infinitely sharp transition between the outer Sérsic and inner power-law regions, namely

$$I(r) = I_b[(r_b/r)^{\gamma}u(r_b - r) + \mathrm{e}^{b(r_b/r_e)^{1/n}}\mathrm{e}^{-b(r/r_e)^{1/n}}u(r - r_b)]. \quad \text{(C1)}$$

Here, r_b denotes the division between the outer Sérsic and inner power-law profiles, I_b is the intensity at this radius, γ is the inner power-law slope, and $u(x - a)$ is the Heaviside step function. Parameters n and r_e refer to the shape and half-light radius of the outer Sérsic profile. Additionally, b is a constant that depends on several free parameters (r_b, γ, r_e, and n).

We require a core galaxy to meet the following criteria: (1) the core-Sérsic model provides a better fit than the Sérsic profile; (2) the cores are well resolved so that the break radius r_b is greater than the second innermost data point in the profile; (3) the inner power-law slope γ is less than the logarithmic slope of the Sérsic profile $(1/n)$ in the core region.

Three sample galaxies meet the above criteria for having a core. Two of these are the central cD galaxies NGC 4874 and NGC 4889. Table 2 summarizes the r_b and γ measured from the core-Sérsic fit.

We further explore the best way to handle these cored galaxies in the 2D luminosity decompositions. Two natural approaches are to fit the whole galaxy, including the core, or to mask the galaxy over $r \leq r_b$. Masking is more physically motivated because the central core is a clear deviation from the inward extrapolation of the Sérsic profile that characterizes the outer galaxy structure. We try both approaches and summarize the results in Table 2. Applying a mask versus no mask has a nominal effect on COMAi125909.468p28227.35, but there is a significant increase in the r_e and n of the cD galaxies when their larger core regions are masked.

Performing the 2D fit with the core masked is more physically motivated, and we consider these models to represent the best fits for the cD galaxies. It is worth noting, however, that our result from Appendix B4 that 100 per cent of the mass in the cDs is associated with structures of $n \gg n_{\mathrm{disc\_max}}$ remains unchanged irrespective of which approach (mask or no mask) we take.

APPENDIX D: SYSTEMATICS OF $n_{\mathrm{disc\_max}}$

Our effort in this paper to make a census (Section 4.2) of dynamically cold versus dynamically hot stellar mass depends fundamentally on the upper limit, $n_{\mathrm{disc\_max}}$ (Section 3.1), measured for the Sérsic index of a disc. In our approach, all structures with Sérsic index $n \leq n_{\mathrm{disc\_max}}$ are considered disc dominated, while all other structures with higher Sérsic index are considered classical components built in mergers.

The value of $n \leq n_{\mathrm{disc\_max}}$ is set by the moderately inclined barred galaxy (COMAi125950.105p275529.44) having the highest outer disc Sérsic index. The accuracy of $n_{\mathrm{disc\_max}}$ depends on how representative the sample is as well as the robustness of the multicomponent structural decompositions. Fig. B5 shows for this galaxy the data image and residuals of the multicomponent decompositions. While this galaxy was identified as an ambiguous E/S0 galaxy in fig. 2 of Marinova et al. (2012), the barred nature of this galaxy seems clear based on the image residuals produced by our improved method (Sections 3.2 and 3.3) of structural decomposition.

The value of $n_{\mathrm{disc\_max}}$ is subject to sky subtraction errors because it is measured from the outermost Sérsic profile of disc galaxies, and this is likely the dominant systematic effect on $n_{\mathrm{disc\_max}}$. As described in Appendix A, we measure the background sky value with a robust method and hold the sky fixed at this value during the fit. To test the importance of the sky subtraction, we refitted COMAi125950.105p275529.44 while adjusting the mean sky background by $\pm 1\sigma$. This produces a range in outer disc n of $n \sim 1.57-1.77$, which spans $\sim$0.1 above and below the adopted $n_{\mathrm{disc\_max}}$ value of 1.66. Based on the narrow error bars for $n_{\mathrm{disc\_max}}$, we do not expect the uncertainty to have a significant impact on our conclusions.

For completeness, we explore for an alternate value of $n_{\mathrm{disc\_max}}$ the relative stellar mass fractions that would be interpreted as belonging to cold versus hot stellar components. The value $n_{\mathrm{disc\_max}} = 2$ is in line with estimates of the Sérsic index of small-scale discs (e.g. Fisher & Drory 2008; Weinzirl et al. 2009) yet is still above the anticipated range in $n_{\mathrm{disc\_max}}$ due to sky subtraction errors in this study. With this higher $n_{\mathrm{disc\_max}}$, we would find that $\sim$51 per cent stellar mass is in disc-dominated components while $\sim$49 per cent is still in classical bulges/ellipticals assembled in major and minor mergers. These values are somewhat different from the corresponding values (43 per cent in disc-dominated structures versus 57 per cent in non-discs) derived in Section 4.2 excluding the two cD galaxies. Choosing a higher $n_{\mathrm{disc\_max}}$ would increase the importance of disc-building processes relative to processes that build classical bulges/ellipticals.

This paper has been typeset from a TEX/LATEX file prepared by the author.